Doctoral Thesis

Scalar and fermionic extensions of the Standard Model

Author: Audrey Degée

Administrative supervisor:
J.R. Cudell
Scientific supervisors:
D. Aristizabal
I. Ivanov

Other members of the jury:
T. Hambye
E. Nardi
President:
P. Magain

A thesis submitted in fulfillment of the requirements for the degree of Ph.D. in Physics

in the

Université de Liège
Interactions Fondamentales en Physique et Astrophysique
Faculté des Sciences

October 2013

Acknowledgements

The contribution of many different people, in their different ways, have made this thesis possible and contributed to the success of this study. I would like to thank all those people.

I could not have succeeded without the guidance and endless source of ideas of my two scientific supervisors: Diego Aristizabal S. and Igor P. Ivanov. Therefore, I am strongly indebted to them without whose knowledge and assistance this study would not have been possible. I would like to express my appreciation to my administrative supervisor, Jean-René Cudell for providing necessary infrastructure and resources to accomplish my research work and for his lesson in physics as well as for all interesting chats. All of them gave me the opportunity to interact and work with them and provided me their personal support throughout my Ph.D. thesis and made many useful comments and suggestions to improve this work. Under their guidance I successfully overcame many difficulties and learned a lot. I cannot forget the hard times of Diego reviewing my thesis, giving his valuable suggestions and making corrections. His generosity, unflinching courage and conviction will always inspire me. Besides of my supervisor, I also acknowledge my thesis examiners for taking their time to read this thesis.

Moreover, most of the results described in this thesis would not have been obtained without them and a close collaboration with Venus Keus and Jernej F. Kamenik. Because of Diego, I had the privilege to collaborate with Jernej F. Kamenik to whom I thank very much and I am very grateful to Venus Keus for her important contributions in this work and for its collaboration and moral support. Further, I am grateful to all members of the IFPA group, including the numerous visitors, for providing a stimulating and fun filled environment. I would also like to convey thanks to the Fonds de la Recherche Scientifique (FNRS) for providing the financial means for this project.

I am also especially indebted to Tiziana and Marjorie who offered her continuous encouragement throughout the course of my study and of this thesis. Their continual guidance and support was indispensable to sustain me to complete this thesis. They were always beside me during the happy and hard moments to push me and motivate me and were always there when I really needed. Thank for their understanding and precious friendship. I gratefully acknowledge Tiziana and Fabio who corrected my thesis carefully, their painstaking effort in reading the drafts are greatly appreciated.

I thank Maxime for his understanding, love, care, patience and constant support during the course of this project, and for all the fun we have had in the years. His encouragement was in the end what made this dissertation possible. I also would like to extend my appreciation to Dounia for her constant moral support and care and for creating a pleasant atmosphere for me at the University. I thank Arnaud for his useful support in some computational issues and for his moral support and precious friendship. I am grateful to my parents for their love, support throughout my life and encouragement in my many moments of crisis. They have provided a carefree environment for me, so that I can concentrate on my study. My thanks also go to my brother and my grandmother who make a comfortable environment for me to live in. Finally, I would like to thank some of my good friends who have played a part over the years in making who I am. I cannot list all the names here, but you are always on my mind.

CONTENTS

Introduction **2**

I Scalar extensions of the Standard Model **3**

1 Multi-Higgs-doublet models **7**
1.1 The SM Higgs sector . . . 7
1.1.1 A minimal scalar sector . . . 7
1.1.2 The Higgs boson at colliders . . . 9
1.2 The 2HDM . . . 12
1.2.1 Beyond the SM Higgs sector . . . 12
1.2.2 An invitation to models with extra Higgs doublets . . . 14
1.2.3 The challenging case of the most general 2HDM . . . 15
1.2.4 Approaches to the general 2HDM . . . 18
1.2.5 The orbit space of the 2HDM . . . 18
1.3 Few comments on the 3HDM . . . 22
1.3.1 The 3HDM . . . 22
1.3.2 The orbit space of the 3HDM . . . 22

2 Higgs masses of the general 2HDM **25**
2.1 Introduction . . . 25
2.2 Mass matrix and mass spectrum . . . 27
2.2.1 Mass related basis-invariants and non-invariants in a toy model . . . 27
2.2.2 Masses in the Minkowski-space formalism . . . 28
2.3 Mass matrix of the most general 2HDM . . . 30
2.3.1 Electroweak-symmetric vacuum . . . 31
2.3.2 Charge-breaking vacuum . . . 32
2.3.3 Neutral vacuum . . . 35
2.3.4 The extra symmetry of the neutral modes . . . 36

3 Highly symmetric 3HDM **37**
3.1 Introduction . . . 37
3.2 Geometric minimization of symmetric potentials . . . 37
3.2.1 Geometric minimization: the main idea . . . 38
3.3 A_4- and S_4-symmetric 3HDM . . . 39
3.3.1 The potentials . . . 39
3.3.2 The toy model case . . . 40
3.3.3 The orbit space in the S_4 case . . . 42
3.3.4 Minimization of the S_4-symmetric potential . . . 44
3.3.5 Unexpected symmetry of the orbit space . . . 44
3.3.6 The orbit space in the A_4 case . . . 46
3.3.7 Minimization of the A_4-symmetric potential . . . 47
3.4 Discussion . . . 47
3.4.1 Origin of geometric CP-violation . . . 47
3.4.2 Coexistence of different minima . . . 48
3.4.3 How general is the proposed method? . . . 48

II Fermionic extensions of the Standard Model **51**

4 Neutrino Physics **55**
4.1 Neutrino flavor oscillations . . . 55
4.2 Neutrino flavor oscillations: experimental evidence . . . 56
4.3 Summary of experimental data . . . 60
4.3.1 Present status of neutrino oscillation data . . . 60
4.3.2 Present status of absolute neutrino masses . . . 61
4.3.3 Present status of charged lepton flavor violation . . . 64
4.4 Neutrino masses: theoretical perspective . . . 65
4.5 The baryon asymmetry of the Universe . . . 69
4.5.1 Boltzmann equations . . . 70

5 MLFV realizations of minimal seesaw **75**
5.1 Introduction . . . 75
5.2 The setups . . . 76
5.3 Lepton-flavor-violating processes . . . 80
5.3.1 $l_\alpha \to l_\beta \gamma$ processes . . . 81
5.3.2 $l_\alpha \to l_\beta l_\beta l_\beta$ processes . . . 82
5.3.3 $\mu - e$ conversion in nuclei . . . 83
5.4 Primordial lepton asymmetries . . . 85

Conclusion **89**

A Algebra of matrices Σ^μ and Π^μ **91**

B The S_4- and A_4-symmetric 3HDM potentials **93**
B.1 The orbit space of the S_4-symmetric potential 93
B.2 Higgs spectra of the S_4-symmetric potential 96
B.3 Higgs spectra of the A_4-symmetric potential 97

C Standard seesaw Lagrangian **101**
C.1 Dirac and Majorana neutrinos 101
C.2 RH neutrinos 102
C.3 Thermodynamic of the early Universe 105

D Formulas and Feynman diagrams for LFV processes **107**

Bibliography **115**

INTRODUCTION

In the Standard Model (SM), ElectroWeak Symmetry Breaking (EWSB) is provided by the Brout-Englert-Higgs (BEH) mechanism [1–4], which predicts the existence of a scalar degree of freedom, the SM Higgs boson. Testing whether the BEH mechanism is responsible for EWSB or whether in contrast a much more intrincated (maybe richer) mechanism is at work is a priority in the Large Hadron Collider (LHC) program. Recently the ATLAS and CMS collaborations have announced the discovery of a new state which resembles to a large extent the features (production and decay properties) of the SM Higgs [5, 6]. Pinning down its nature has become of major importance, and the LHC has already started providing the first clues. Although a comprehensive understanding of the picture lying beneath will probably require not only time but even technical efforts beyond LHC [7].

Regardless of whether the discovered scalar is or not the SM Higgs, theoretical-based as well as experimental data beyond collider physics support the idea that new physical degrees of freedom at certain unknown energy scale should be present [1]. Accordingly, in relation with recent LHC results it can be said that if deviations from the SM picture are found [2] this might hint to the physics responsible for those theoretical and/or experimental issues, otherwise the exact mechanism for EWSB would be definitively established but nevertheless the quest for the physics responsible for those phenomena the SM cannot account for will continue to be pursued both theoretically and experimentally in the high-energy as well as in the high intensity frontiers.

Motivated by these observations, in this thesis several aspects of beyond SM physics schemes have been treated. In particular, two categories of models have been considered: (*i*) models with extra Higgs ElectroWeak (EW) doublets (multi-Higgs-doublet models) [9, 10], (*ii*) models with new fermion EW singlets (type-I seesaw models) [11–15]. In the first category, two problems associated with the most general two-Higgs-Doublet Model (2HDM) and with the three-Higgs-Doublet Model (3HDM) have been tackled. In the former case the scalar mass spectrum has been derived in a basis-invariant fashion

1. These data involve neutrino oscillation and astrophysics experiments. The former providing an unquestionable proof that neutrinos are massive while the later establishing a precise determination of the cosmic baryon asymmetry and supporting the existence of dark matter.

2. As of 2013, ATLAS is observing an excess in the $\gamma\gamma$ channel while CMS is not [8]. However, given current data, knowing whether this corresponds to a "genuine" deviation is not possible and further statistics is needed.

whereas in the later, after introducing a general procedure for the minimization of highly symmetric potentials, the minimization of an S_4 and of an A_4 3HDM has been analyzed. In the second category, the possibility of envisaging seesaw-like models yielding sizeable lepton-flavor-violating decay rates has been investigated. With the models at hand, the corresponding charged lepton-flavor-violating phenomenology has been studied focusing on rare muon decays, for which forthcoming lepton-flavor-violating experiments will be able to prove large parts of their parameter space. The results of these investigations have been published in [16–18], and constitute the main part of this thesis (Chapter 2, 3 and 4).

In order to make the manuscript much more handable and readable, the thesis has been divided in two parts: *Scalar extensions of the SM* and *Fermionic extensions of the SM*. Each part contains its own short introduction, where the subjects treated are motivated and an explanation of its structure is given. An introductory Chapter covering standard material and aiming to provide the tools used in the main chapters (2, 3 and 5) has been also added in each part (1 and 4). It is worth stressing that these opening Chapters are not intended to give comprehensive reviews of any of the subjects they deal with, their aim is only to put into context the main part of the thesis. Thorough reviews as well as textbooks on those subjects exist and the reader is referred to them for exhaustive details [9, 19–27]. Finally, lengthy calculations associated with Chapters 2, 3 and 5 have been included in Appendices A, B, C and D.

Part I

Scalar extensions of the Standard Model

INTRODUCTION

Since the discovery of β decay, many efforts have been made in order to understand the nature of weak interactions. The first model capable of successfully describing experimental data at low energies was the effective β decay theory proposed by Fermi in 1934 [28]. This formulation, however, being based on an effective operator, was only suitable for describing low-energy data, at high energies unitarity was violated. In modern jargon, it is a non-renormalizable theory. It was not only until 1967 that Weinberg [29], Salam [30] and Glashow [31] proposed a successful model for EW interactions, which, after adding strong interactions, well described by Quantum ChromoDynamic (QCD), constitutes what is now known as the SM of particle physics. It accurately describes many experimental results that probe elementary particles and their interactions up to an energy scale of a few hundred GeV. Indeed, very precise experiments at CERN Large Electron Positron Collider (LEP), at SLAC Linear Collider (SLC) and at the Fermilab Tevatron collider, which were quite sensitive to quantum corrections that were carried out through a great theoretical effort, demonstrated with an impressive accuracy the validity of this model. All the parameters of the SM except the Higgs mass have been experimentally determined with a huge precision and through these parameters, any physical EW observables can be predicted and confronted with experimental data. An open question which started being addressed first by LEP [32] and the Tevatron [33], and is currently investigated by the LHC [34] is, undoubtedly, the mechanism for spontaneous EWSB. In the SM, the mechanism responsible for EWSB is driven by a complex scalar EW doublet (ϕ) acquiring a non-vanishing Vacuum Expectation Value (VEV). The gauge group of the SM, $SU(3)_c \otimes SU(2)_L \otimes U(1)_Y$, is therefore broken according to

$$SU(3)_c \otimes SU(2)_L \otimes U(1)_Y \rightarrow SU(3)_c \otimes U(1)_Q, \tag{1}$$

via the BEH mechanism [1–4]. The renormalizable and gauge invariant interactions of ϕ allow for a scalar potential. As a consequence EW gauge bosons ($W^{\pm}$ and Z) as well as fermions acquire a mass in a gauge-invariant way. Furthermore, the theory exhibits a new physical scalar degree of freedom, the Higgs boson (H). Testing the properties of the Higgs boson is crucial and the search for this particle has become one of the main goals of particle accelerators for last two decades. The discovery of the correct mechanism for EWSB has been as well a major priority. Recently, the ATLAS [5] and CMS [6] collaborations have announced the discovery of a heavy boson that could complete the

SM picture. Despite some deviations from the SM expectations, in particular in the $\gamma\gamma$ channel, the newly discovered scalar exhibits properties quite close to those of the SM scalar. Pinning down in a definitive way its properties will require further efforts and maybe even a high precision machine such as the International Linear Collider (ILC) [35].

If the newly discovered scalar does not feature SM properties this might hint towards the physics responsible for the theoretical and experimental information the SM cannot account for[3]. Examples of that new physics could be multi-Higgs-doublet models [9], supersymmetry [36, 37] and composite Higgs models [38], among others.

The first part of this thesis is organized in three Chapters. Chapter 1 is a review chapter, covering standard materiel related with the SM and models involving extra EW doublets. Chapter 2 addresses the issue of determining the scalar mass spectrum of the 2HDM in a basis-invariant fashion while Chapter 3 deals with a novel approach for the minimization of highly symmetric scalar potentials applied to specific versions of the 3HDM.

3. Theoretically here means the instability of the Higgs mass under quantum corrections, which once heavy degrees of freedom are added to the SM (e.g. heavy RH neutrinos accounting for neutrino masses), implies the hierarchy problem.

CHAPTER 1

MULTI-HIGGS-DOUBLET MODELS

This chapter aims at providing a motivation for multi-Higgs doublet models as well as the technical framework for Chapters 2 and 3. It is not intended to give a comprehensive review of neither theoretical nor phenomenological aspects of the SM and/or extended scalar sectors, for which the reader is referred to e.g. [9, 20, 21]. The Chapter is organized as follows: first of all the SM scalar sector and the Higgs SM collider phenomenology is accounted for in Section 1.2. Section 1.2 provides a phenomenological-based motivation for extended scalar sectors, focusing on models with extra EW doublets. The theoretical-based challenges of those scenarios, in particular of the 2HDM are emphasized, and the techniques used to address those problems are discussed. Finally, in Section 1.3, the 3HDM is introduced and the corresponding techniques which allow its analysis are briefly summarized.

1.1 The SM Higgs sector

1.1.1 A minimal scalar sector

Before discussing technicalities of extended scalar sectors some details about the SM Higgs are worth reviewing. Rather than providing full details, this brief review aims at giving a general picture of the SM Higgs boson, and the current status of Higgs searches at the LHC. Comprehensive phenomenological reviews including beyond SM Higgs sectors exist, see e.g. [20, 21]. As already pointed out, in the SM, the EW gauge bosons as well as the fermions acquire their mass via the BEH mechanism. Masses for these fields are introduced in a gauge-invariant way by endowing the SM Lagrangian with a $Y = 1$ hypercharge $SU(2)$ complex doublet:

$$\phi(x) = \frac{1}{\sqrt{2}} \begin{pmatrix} \phi^+(x) \\ \phi^0(x) \end{pmatrix} . \tag{1.1}$$

The SM interactions in which the SM scalar participates are given by the following Lagrangian:

$$\mathcal{L}_\phi = (D^\mu \phi)^\dagger (D_\mu \phi) - V(\phi^\dagger \phi) , \tag{1.2}$$

where the covariant derivative, which guarantees the $SU(2)_L \otimes U(1)_Y$ gauge invariance of the theory, reads

$$D_\mu = \delta_\mu + ig\frac{\tau^i}{2} \cdot W^i_\mu + i\frac{g'}{2} Y B_\mu \,, \tag{1.3}$$

with $\tau^i/2$, the Pauli matrices, and Y the $SU(2)_L$ and $U(1)_Y$ generators and g, g' the corresponding gauge couplings. The pure scalar couplings are determined by the scalar potential $V(\phi^\dagger\phi)$, which because of renormalizability and gauge invariance only involves quadratic and quartic couplings,

$$V(\phi^\dagger\phi) = \mu^2\phi^\dagger\phi + \lambda(\phi^\dagger\phi)^2 \,. \tag{1.4}$$

In addition, gauge invariance of the fermion bilinear couplings demands at the Yukawa coupling level

$$-\mathcal{L}_Y = \overline{u}_R Y_u Q_L \tilde{\phi}^\dagger + \overline{d}_R Y_d Q_L \phi^\dagger + \overline{l}_R Y_e \ell_L \phi^\dagger \,, \tag{1.5}$$

where u_R, d_R are the up-type and down-type quark EW singlets, l_R are the lepton $SU(2)$ singlets and Q_L and ℓ_L are the quark and lepton $SU(2)$ doublets. The different quark-quark-scalar couplings are encoded in $Y_{u,d,e}$ which are 3×3 matrices in flavor space.

EWSB is triggered by the non-vanishing scalar VEV, which from the scalar potential minimization condition [1] can be written as

$$v = \sqrt{\frac{-\mu^2}{2\lambda}} \,. \tag{1.6}$$

This symmetry breaking pattern must guarantee $U(1)_Q$ invariance, implying three out of the four $SU(2)_L \otimes U(1)_Y$ generators are broken after EWSB. Accordingly, three Goldstone bosons (GB's) appear and become the longitudinal degrees of freedom of the massive EW gauge bosons. A useful parametrization of the scalar doublet where the GB's and the remaining physical degree of freedom, the Higgs, are made explicit reads

$$\phi(x) = e^{i\tau^i \frac{\chi_i(x)}{2v}} \begin{pmatrix} 0 \\ \frac{v+H(x)}{\sqrt{2}} \end{pmatrix} \,, \tag{1.7}$$

which then in turn, by rotating away the GB's degrees of freedom, can be made real (in technical jargon, by choosing the unitary gauge [2]):

$$\phi(x) \longrightarrow^{SU(2)} \phi(x) = \begin{pmatrix} 0 \\ \frac{v+H(x)}{\sqrt{2}} \end{pmatrix} \,. \tag{1.8}$$

With $\phi(x)$ parametrized as in (1.8) it is now straightforward to determine the EW gauge boson and fermion masses in terms of the SM scalar EW doublet VEV and the Higgs

1. A bounded from below scalar potential requires $\lambda > 0$, which then implies a non-vanishing VEV. develops provided $\mu^2 < 0$.

2. It is worth bearing in mind that while this gauge has the advantage of making the particle (physical degrees of freedom) content of the theory explicit, the massive gauge boson propagators suffer from a problematic ultra-violet divergence when it comes to the calculation of massive gauge boson mediated scattering amplitudes. Though being much more involved, this however does not mean proving the renormalizability of the theory is not possible in such a gauge

boson mass itself. More importantly—for the following discussion—the different Higgs couplings which determine the Higgs collider phenomenology can also be derived. When combined with (1.6), the Lagrangians in (1.2) and in (1.5) yield

$$M_W = \frac{gv}{2}, \quad M_Z = \frac{gv}{2\cos\theta_W}, \quad m_f = \frac{v}{\sqrt{2}}Y_f\,, \tag{1.9}$$

(with f = quarks or charged leptons) while using (1.4) it reads

$$M_H = \sqrt{-2\mu^2}\,. \tag{1.10}$$

Some words of caution are in order regarding results in (1.9) and (1.10). The scalar doublet VEV is measured in μ decay to be $v = (\sqrt{2}G_{\rm F})^{-\frac{1}{2}} \simeq 246$ GeV with $G_{\rm F}$ the Fermi constant while the weak mixing angle θ_W is measured via different reactions e.g. elastic neutrino-lepton scattering: $\overline{\nu}_\mu + e \to \overline{\nu}_\mu + e$. Its value at the Z mass according to the PDG [39] is given by $\sin^2\theta_W = 0.231$. Thus, the relations in (1.9) for the W and Z mass combined with these experimental information allow the determination of M_Z and M_W. For the fermion masses, it has been assumed that the fermion fields in the Lagrangian in (1.5) have been rotated to the mass eigenstate basis. In contrast to the weak gauge couplings the Yukawa couplings are experimentally unknown. Their measurement requires Higgs production and precise determination of fermion channels. Indeed, measuring Yukawa couplings strengths turns out to be a powerful strategy to determine whether the associated scalar is or not the SM one.

As for the SM Higgs collider phenomenology the couplings HVV (with $V = W, Z, \gamma$) and $H\overline{f}f$ can be read off directly from the Lagrangians in (1.2) and (1.5) once (1.6) is taken into account:

$$g_{HVV} = 2i\frac{M_V^2}{v}, \quad g_{Hf\bar{f}} = -i\frac{m_f}{v}\,. \tag{1.11}$$

1.1.2 The Higgs boson at colliders

Studying Higgs properties at colliders (as for any particle) requires first production and then subsequent analysis of its decay modes. Higgs production depends on the specific machine. In e^+e^- colliders three production mechanisms are at work: Bjorken ($e^+e^- \to Z^*H$, represented in diagram (b) of Figure 1.1) and weak vector boson fusions ($e^+e^- \to e^+e^-H$ if $V = Z$ or $e^+e^- \to \overline{\nu}\nu H$ if $V = W$, represented in diagram (a) of Figure 1.1). In particular at LEP, due to the center-of-mass energy, the Bjorken mechanism dominated. In hadronic machines, in particular at the LHC, the above mechanisms, controlled by $\alpha_{\rm EW} = g^2/4\pi$ are overwhelmed by mechanisms driven by $\alpha_S = g_s^2/4\pi$, namely gluon fusion (diagram (c) in Figure 1.1). Additional mechanisms are weak boson fusion, Higgs-strahlung (diagram (e) in Figure 1.1) and $\overline{t}t$ emission (diagram (f) in Figure 1.1). Once produced, depending on kinematical thresholds, different modes will dominate. Ignoring for the time being any collider data the following kinematical regions can be identified:

I. Heavy kinematical region ($M_H > 2m_t$): Events with the vector boson channels open, the $\overline{t}t$ mode being controlled by $y_t \sim 1$ will dominate Higgs decays.

II. Intermediate kinematical region ($2M_Z < M_H < 2m_t$): In this kinematical window the $\overline{t}t$ mode is kinematically forbidden while the vector boson channels are open, thus

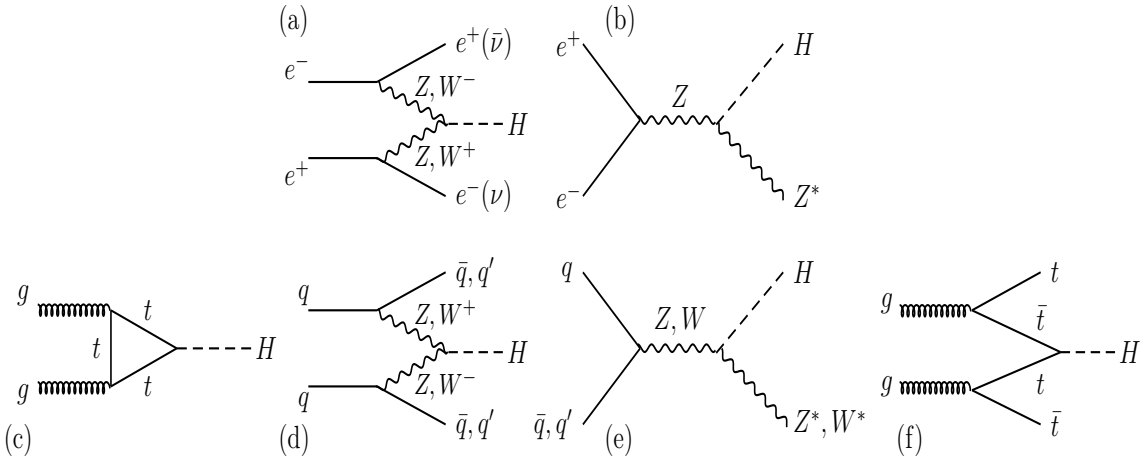

Figure 1.1: *Feynamn diagrams for H production at e^+e^- ((a) and (b)) and proton-proton ((c)-(f)) colliders.*

dominating. Between the WW and ZZ modes the WW branching fraction turns out to be a factor 2 larger due to the ZZ mode involving unidentifiable particles. In principle three-body decay modes involving the top quark are possible ($H \to tt^* \to tWb$), but are sub-dominant due to phase-space suppression factors.

III. Low kinematical region ($M_H < 2M_V$): Higgs boson decays are driven by the $b\bar{b}$ mode, as the leptonic $\tau\overline{\tau}$ turns out to have a branching ratio more than an order of magnitude smaller due to the combined effect of the color factor and the relative Yukawa couplings size ($y_b^2/y_\tau^2 \sim 16$). EW-gauge-boson three-body decays are also possible ($H \to WW^* \to W\ell\nu(cs)$, $H \to ZZ^* \to Z\ell\bar{\ell}(q\bar{q}, \nu\nu)$). In hadronic machines, these modes despite their suppression can be even more relevant than the $b\bar{b}$ channel (this has been actually the case at the LHC).

To complete the picture intrinsically quantum decay modes have to be accounted for. The Higgs being charge and color neutral does not couple at the tree level with neither photons nor gluons, the two-body decay modes $H \to \gamma\gamma$ and $H \to gg$ therefore proceed via fermion and vector-boson loops, of which top loops give the dominant contribution (there are subtle details when calculating the corresponding partial decay widths, see e.g. [20, 21]). The couplings in (1.11) can be recasted in terms of the Fermi constant:

$$g_{HVV} = 2iM_V^2\sqrt{\sqrt{2}G_{\rm F}}, \quad g_{Hf\bar{f}} = -im_f\sqrt{\sqrt{2}G_{\rm F}}\,, \tag{1.12}$$

thus implying than when calculating the partial decay widths of the aforementioned processes the only free parameter left is the Higgs boson mass. Figure 1.2 shows the relative importance of the different Higgs boson decay branching ratios for the intermediate and low energy kinematical regions (regions II and III) as a function of the Higgs mass. The width of the corresponding bands is associated with parametric uncertainties, which originate from uncertainties in input parameters, and theoretical uncertainties, stemming usually from missing higher orders [40]. Up to know nothing has been said about pure scalar couplings: H^3 and H^4. The corresponding strengths can be extracted from the scalar potential in (1.4) after taking into account, once again, (1.6). The couplings read

$$g_{HHH} = -3i\frac{M_H^2}{v}, \quad g_{HHHH} = -3i\frac{M_H^2}{v^2}\,. \tag{1.13}$$

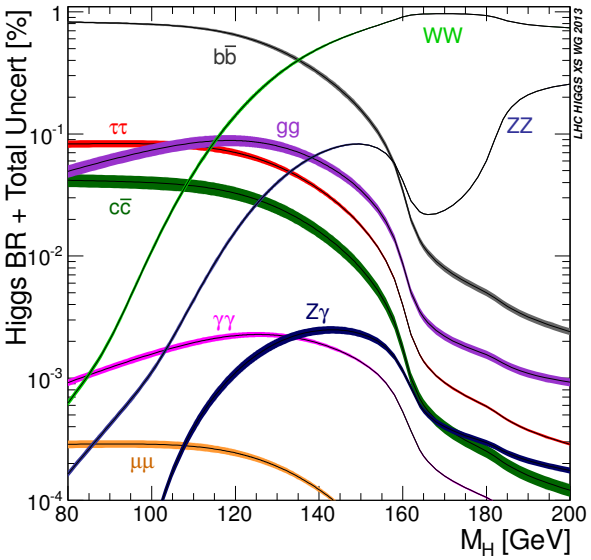

Figure 1.2: *Decay branching ratios for the SM Higgs as a function of its mass width of the corresponding curves follow from parametric and theoretical uncertainties [40] (see the text for further details).*

These Higgs boson scattering processes ($HH \to H$ and $HH \to HH$) are crucial for the reconstruction of the scalar potential parameters and for unravelling the mechanism of EWSB. However, an experimental program based on Higgs scattering processes is far beyond the LHC possibilities and might require a Higgs factory [3] which could be based on e.g. a linear $125 \otimes 125$ GeV e^+e^- collider or a circular 125 GeV e^+e^- machine. Suggestions have already been put forward by Blondel and Zimmermann [41], and indeed much more technical analyses have been recently carried out in Ref. [42].

In addition to theoretically based arguments such as unitarity, positivity, perturbativity and minimum constraints, which constrained the Higgs boson mass to be below 1 TeV [43, 44], before the LHC era the Higgs boson mass was already constrained by LEP and Tevatron data: EW precision data favored a Higgs mass of the order of 90 GeV with an upper limit of 152 GeV at the 95% Confidence Level (CL) [45], LEP excluded values below ~ 114 GeV at 95% CL [46] while Tevatron closed the mass window $162 - 166$ GeV at the 95% CL [47]. Given its design and capability LHC [5, 6] has gone far beyond LEP and Tevatron making a major discovery, a new scalar particle which seems to resemble quite closely the SM Higgs boson properties.

As of 2012, ATLAS (CMS) searching for the SM Higgs boson in the $\gamma\gamma, ZZ^*, WW^*, \tau\bar{\tau}$ and $b\bar{b}$ channels, and using data samples corresponding to integrated luminosities of approximately 4.8 fb^{-1} (5.1 fb^{-1}) at a center-of-mass energy of 7 TeV and 5.8 fb^{-1} (5.3 fb^{-1}) at $\sqrt{s} = 8$ TeV, reported an excess of events above background with a local significance of $5.9\,\sigma$ ($5\,\sigma$). The excess being more pronounced in the channels with highest mass resolution: ZZ^* and $\gamma\gamma$. The fit to the signals giving a mass of 126 ± 0.4 (stat.) ± 0.4 (syst.) GeV [5] (125 ± 0.4 (stat.) ± 0.5 (syst.) GeV [6]). Figure 1.3 show the

3. Strictly speaking the LHC is a Higgs factory, however due to its dirty experimental conditions the range of Higgs modes that can be measured accurately is limited.

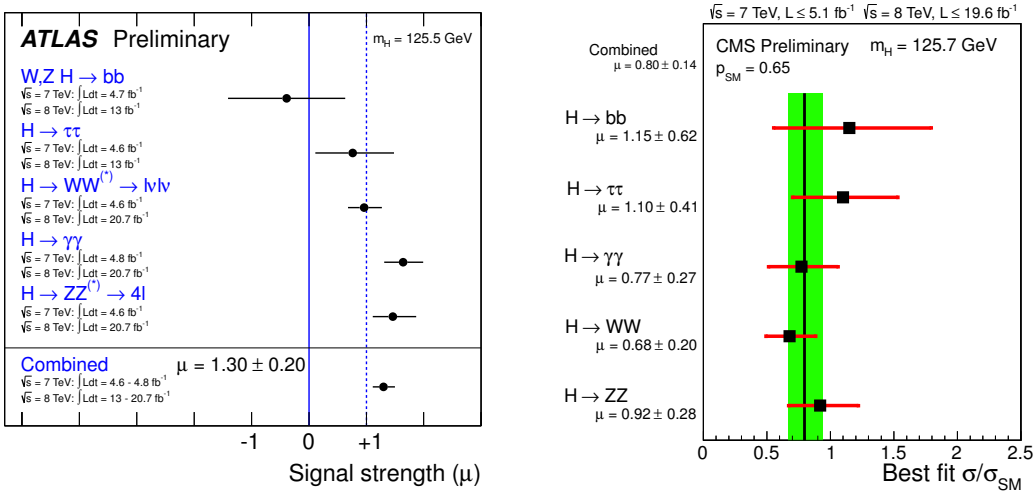

Figure 1.3: *The signal strength for the individual channel and their combination at ATLAS (left) and at CMS (right) [48]. The values of combined signal strength, $\mu = \sigma/\sigma_{SM}$, are given for $M_H = 125.5$ GeV for ATLAS ($\mu = 1.3 \pm 0.13(stat.) \pm 0.14(syst.)$ [49]) and for $M_H = 125.7$ GeV for CMS ($\mu = 0.8 \pm 0.14$ [50]).*

results for the individual channels and their combination for ATLAS (left-hand side plot) and CMS (right-hand side plot). In both cases $\mu = \sigma/\sigma_{SM} = 1$ corresponds to the SM hypothesis. In conclusion, according to these data, the discovered scalar is compatible with the hypothesis of being the SM Higgs particle. However, it is also a fact that further data are needed in order to pin down whether this scalar is actually the one expected from the SM or whether it is in contrast a gate towards beyond SM physics.

Finally, as of 2013 results for both CMS and ATLAS based on samples with an integrated luminosity of ~ 25 fb^{-1} and $\sqrt{s} = 8$ TeV exist. These results, however, are still spread in proceedings and/or slides (presentations), mainly of the Moriond2013 and EPS-HEP2013 conferences. An official paper from neither ATLAS nor CMS exist yet, accordingly, apart from stressing that the picture of a SM-like Higgs remains, no further discussion on the experimental status of Higgs searches will be done.

1.2 The 2HDM

1.2.1 Beyond the SM Higgs sector

Even if the scalar particle discovered at the LHC turns out to be the SM Higss boson, there are deep reasons to expect manifestations of physics beyond the SM. These reasons can be grouped into two somehow non-overlapping sets: theoretical and experimental. Theoretically, the main motivation for beyond SM physics is certainly the hierarchy problem [51], which for more than three decades has been the subject of intense research. Experimentally, three main observations: neutrino oscillations [52], the cosmic baryon asymmetry [53] and astrophysical data supporting the existence of dark matter [54], implying the following questions: what is the origin of neutrino masses, the origin of matter and the origin of dark matter? Whether these facts necessarily involve beyond SM physics

and/or whether this new physics should show up is arguable, as of course expected from any scientific argument. The position adopted here is however that these facts, in particular those grouped in the experimental set, are a solid evidence in favor of beyond SM physics.

The scalar sector of the SM is minimal, this means that the associated Higgs representation [4] is the simplest possibility allowing for non-vanishing mass terms for EW bosons and fermions after spontaneous EWSB. However, no fundamental reason exists to claim that the scalar sector is minimal i.e. that it contains only one Higgs doublet. Thus, since the SM Higgs sector has not been experimentally tested yet, larger or additional representations are still a well motivated possibility. For example, extended Higgs sectors with extra $SU(2)$ singlet, doublet and triplet fields can be added to the minimal Higgs sector. Adding more scalar fields is a simple theoretical commitment while the range of new dynamical possibilities it generates is very wide. Moreover, many new physics models often predict extended Higgs sectors at the low-energy effective theory level [55].

Examples of beyond SM physics involving extended Higgs sector are numerous, e.g. supersymmetry [36, 37] and grand unified theories [56]. New physics models which can explain tiny neutrino masses (see table 4.1 in the next Chapter) also often predict an extension of the Higgs sector. For example, the type-II seesaw model [14, 57–59], where a $Y = 1$ Higgs triplet field is added to the SM, can generate tiny neutrino masses at the tree level. Radiative seesaw models [60,61], that can also account for tiny neutrino masses typically require additional scalar bosons running in the loops. Some models beyond SM which contain an extended Higgs sector could also explain the origin of dark matter. Indeed, very simple realizations relying on 2HDMs with an unbroken discrete symmetry in the Higgs sector provide dark matter candidates.

There are two important experimental observables through which Higgs sectors (scalar sectors) beyond the SM can be constrained:

I. The so-called ρ parameter defined as [62]

$$\rho = \frac{M_W^2}{M_Z^2 \cos\theta_W}\,, \tag{1.14}$$

which at tree-level, within the SM, satisfies $\rho = 1$ as can be seen from the tree-level relations in (1.9). Adding loop corrections modify this result but only slightly, the ρ parameter remains of order 1 even at the quantum level in perfect agreement with data. It turns out that by adding Higgs (scalar) multiplets with suitably chosen weak isospin (e.g. triplets, sextets, octets) and hypercharge, the ratio M_Z/M_W can be basically anything, in clear disagreement with data. Exceptions to this statement are models involving $SU(2)_L$ singlets and/or extra Higgs doublets, for which in the latter case the ρ parameter reads [19]

$$\rho = \frac{\sum_i \left(T_i(T_i+1) - (T_i^3)^2\right) v_i^2}{2\sum_i (T_i^3)^2 v_i^2}\,, \tag{1.15}$$

where T_i, T_i^3 and v_i correspond respectively to the weak isospin, the third component weak isospin and the VEVs of the doublet ϕ_i. Clearly, $\rho = 1$ regardeless of the number of doublets.

4. The smallest representation containing the three would-be Goldstone fields associated with the three massive gauge bosons and the Higgs scalar is a single $SU(2)_L$ doublet.

II. Rare-process-related observables: Once going beyond the SM scalar sector, the new Yukawa interactions induced by the new scalar degrees of freedom generally (indeed almost unavoidably) induce rare flavor violating transitions, which according to flavor violating experimental data are severely constrained (e.g. $K_L \to \mu e, K_L \to \pi^0 l\bar{l}, K^+ \to \pi^+ l^+ l^-, \mu \to e\gamma, \mu \to 3e$). In the SM quark sector these rare processes are absent at the tree-level (GIM-mechanism [63]), arising only at the loop-level so providing an explanation for their smallness. On the other hand, with neutrinos being massless in the SM, rare processes in the lepton sector are always absent (they can be rotated away). Experimental flavor violating data thus provides a powerful tool to constraint the parameters of extended scalar sectors.

All in all, these experimental constraints, more importantly the ρ parameter constraint, arguably favor extended scalar sectors involving extra doublets (singlets as well, but nothing else will be added about this possibility). Indeed multi-Higgs-doublet models [9, 64–71] can be regarded as a quite conservative possibility which involves an amazingly rich phenomenology ranging from low-energy rare decays up to high-energy collider physics, that is to say covering both the high intensity as well as the high-energy frontiers.

1.2.2 An invitation to models with extra Higgs doublets

There is a vast literature on models involving scalar sectors with extra EW doublets, in particular in 2HDMs (for a review see [9]). However, models involving more than two scalar EW doublets have also been subject of intensive work. The motivations for such an extensive amount of research is diverse, and cover several particle physics scenarios as well as astroparticle physics and cosmology.

Arguably, nowadays, the main motivation comes from LHC physics. In the light of ATLAS and CMS findings, the question of whether the scalar sector associated with the discovered scalar is or not minimal (pure SM) has gained strength. However, given the SM-like behavior of this scalar, the possible scenarios are tightly constrained, and finding frameworks where one, out of several, degree of freedom exhibits SM-like properties has turned out to be a non-simple task. Indeed, current data have already been used to put stringent constraints in models involving scalar sectors largely departing from the SM (see e.g. [72]). The 2HDM provides an ideal playground where a much more intrincated scalar sector is at work, but one of the three neutral scalars readily have SM-like behavior [5].

In the most general 2HDM the new Yukawa reactions induce rare processes with dangerously large decay rates. Several approaches to avoid such a phenomenological inconsistency exist, among which the following can be distinguished: (i) assume the new Yukawa couplings obey certain structures e.g. $Y^f_{\alpha\beta} \propto \sqrt{m_{f_\alpha} m_{f_\beta}}$, where $f = l, u, d$ and α, β are generation indices [74]; (ii) decouple the new degrees of freedom e.g. assuming $\mathcal{O}(m_S) \sim 10^2$ TeV or so, with m_S a generic scalar mass; (iii) introduce a suitable symmetry which guarantees that the parameters inducing rare processes either vanish or are suppressed. Among these categories, from the phenomenological point of view, probably category (iii) turns out to be the most appealing, if related with a simple symmetry choice.

5. In the conventional notation h^0 and H^0 denote the two CP-even states whereas A^0 the CP-odd state. Given LHC results, the possibility that the signals are due to A^0 decays is already ruled out [73].

Surprisingly, a $\mathbb{Z}_2$ symmetry suffices to yield a relatively large variety of 2HDM realizations each one with its own and somehow distinctive phenomenology. Assuming one doublet is $\mathbb{Z}_2$-even while the other is $\mathbb{Z}_2$-odd, five models can be defined by taking the SM left-handed fermion fields to be $\mathbb{Z}_2$-even and assigning different $\mathbb{Z}_2$ parities to the right-handed fermions. In doing so, the so-called type-I [75, 76], type-II [76, 77], leptophilic (or type-X), type-Y [78–82] and inert [78, 83] 2HDMs arise. Recently these models have been the subject of extensive collider studies (see e.g. [84–87]), mainly motivated by the diphoton signal excess reported by CMS and ATLAS collaborations, which though not yet statistically significant has generated a great deal of attention.

Multi-Higgs doublet models also provide scenarios where the origin of neutrino masses, the cosmic baryon asymmetry and dark matter can be addressed, sometimes even providing a common explanation for all of them. In the simplest approaches, typically, the resulting pictures have the ingredients that guarantee the Sakharov conditions are quantitatively satisfied [53] (for more details see Chapter 4), allowing for an explanation of the cosmic baryon asymmetry via EW baryogenesis [88, 89] [6]. Under certain simple assumptions viable dark matter frameworks can also be defined, the most remarkable example being the inert 2HDM, which has been the subject of intensive investigation in the last years. Finally, a large number of models for Majorana neutrino masses involving extended Higgs sectors exist, in particular in scenarios where the Majorana neutrino mass matrix arises via radiative corrections, in this case the most well studied scenario corresponds to the radiative seesaw where the inert doublet model is enriched with fermion EW singlets (right-handed neutrinos) [90].

1.2.3 The challenging case of the most general 2HDM

Having discussed in some details the phenomenological motivations for models involving extra doublets, it is now clear that it would be interesting going beyond particular cases and tackling the most general problem (model). This can be guided by three main goals: (*i*) identification of the phenomenological consequences parameter dependence; (*ii*) identification of possible symmetries and their corresponding dynamics, that is to say whether they are always broken or whether—instead—remain exact under certain conditions; (*iii*) identification of those properties which holding at the tree-level are not valid once quantum effects are taken into account.

The main challenge when pursuing such a task is the large number of free parameters involved, with several choices yielding (defining) particular realizations. Despite involving a large number of parameters, an appealing strategy when tackling the general problem, which allows a rather significant simplification, consist on constructing a set of basis-invariant quantities. Writing observables in terms of these basis-invariant quantities reduces somehow the arbitrariness of the corresponding phenomenology. Methods for treating the 2HDM via basis-invariants are well known and different approaches and studies exist [91–93]. These methods, when extended to include non-unitary transformations [94–96] provide—probably—the most powerful approach to the general problem, since the most relevant qualitative features are determined by geometric properties of the orbit space (see Section 1.2.5). Indeed these geometric techniques allowed a full treatment

6. These conditions despite being satisfied at the qualitative level in the SM, fail at the quantitative level, see the discussion in Chapter 4.

of the problem (at only the scalar potential level) and lead to a deeper understanding of the 2HDM [94–97].

The 2HDM involves two identical EW doublets with hypercharges $Y = \pm 1$ (here for definitiveness $Y = +1$ will be taken):

$$\phi_i = \begin{pmatrix} \phi_i^+ \\ \phi_i^0 \end{pmatrix} , \tag{1.16}$$

with $i = 1, 2$. The doublets being complex involve eight degrees of freedom from which three will become the longitudinal components of the EW gauge bosons, thus implying the physical spectrum involves five scalar degrees of freedom: three electrically neutral and one charged and its conjugate. In general, unless enforced by a symmetry, both doublets acquire a v.e.v's $\langle \phi_i \rangle = v_i$, so $v = \sqrt{v_1^2 + v_2^2}$. The eight degrees of freedom become evident when adopting the parametrization in (1.7), namely

$$\phi_i = \begin{pmatrix} w_i^+ \\ \frac{v_i + h_i + i\eta_i}{\sqrt{2}} \end{pmatrix} . \tag{1.17}$$

The Lagrangian accounting for the doublet interactions reads:

$$\mathcal{L} = \mathcal{L}_{\text{Yuk}} + \mathcal{L}_\phi \, , \tag{1.18}$$

where the EW gauge boson and pure scalar coulings are encoded in

$$\mathcal{L}_\phi = \sum_{i=1,2} (D_\mu \phi_i)^\dagger (D_\mu \phi_i) - V_H(\phi_1, \phi_2) \, . \tag{1.19}$$

The most general gauge invariant and renormalizable potential $V(\phi_1, \phi_2)$ of the 2HDM is defined in the 8-dimensional space of Higgs field and is a Hermitian combination of the EW-invariant combinations $(\phi_i^\dagger \phi_j)$, $i, j = 1, 2$. In models of EW interactions with spontaneously broken gauge invariance, renormalizability limits to four the degree of the Higgs potential, terms of order greater than four have to be excluded because they are not renormalizable, therefore, the maximum power of the combination $(\phi_i^\dagger \phi_j)$ is two. The most general two-Higgs-doublet potential is conventionally then parametrized in a generic basis as:

$$V = V_2 + V_4 \, , \tag{1.20}$$

where

$$\begin{aligned} V_2 &= -\frac{1}{2}\left[m_{11}^2 (\phi_1^\dagger \phi_1) + m_{22}^2 (\phi_2^\dagger \phi_2) + m_{12}^2 (\phi_1^\dagger \phi_2) + m_{12}^{2\,*} (\phi_2^\dagger \phi_1) \right] ; \\ V_4 &= \frac{\lambda_1}{2} (\phi_1^\dagger \phi_1)^2 + \frac{\lambda_2}{2} (\phi_2^\dagger \phi_2)^2 + \lambda_3 (\phi_1^\dagger \phi_1)(\phi_2^\dagger \phi_2) + \lambda_4 (\phi_1^\dagger \phi_2)(\phi_2^\dagger \phi_1) \\ &+ \frac{1}{2}\left[\lambda_5 (\phi_1^\dagger \phi_2)^2 + \lambda_5^* (\phi_2^\dagger \phi_1)^2 \right] + \left\{ \left[\lambda_6 (\phi_1^\dagger \phi_1) + \lambda_7 (\phi_2^\dagger \phi_2) \right] (\phi_1^\dagger \phi_2) + \text{H.c.} \right\} . \end{aligned} \tag{1.21}$$

This general potential with all quadratic and quartic terms contains 14 real free parameters (in contrast to only two real parameters in the SM case): the real parameters (by hermiticity of the potential) $m_{11}^2, m_{22}^2, \lambda_1, \lambda_2, \lambda_3, \lambda_4$ and the complex parameters $m_{12}^2, \lambda_5, \lambda_6, \lambda_7$.

This potential accounts for EWSB and therefore for massive SM EW gauge bosons and fermions. The problem of the large number of parameters involved, highlighted previously, at this point becomes evident. In contrast to the SM, where the choice $\lambda > 0$ and $\mu^2 < 0$ assures EWSB, in this case the appropriate parameter choice is far from trivial, the large freedom implied by the 14 new parameters allows for CP-violating, CP-conserving, electric charge and color breaking minima. Choosing the correct parameter combination is therefore of fundamental importance, but following the standard algebraic approach yields no further insights: minimization of the potential leads to high order algebraic equations for which a solution in the general case does not exist. In order to see this is actually the case, the following notation is adopted:

$$\Phi_a = \begin{pmatrix} \phi_1 \\ \phi_2 \end{pmatrix} . \tag{1.22}$$

Note that here both ϕ_1 and ϕ_2 are EW doublets themselves, so that although $a = 1, 2$, Φ_a effectively incorporates four complex fields. Thus, in the definition of Φ_a there is a hidden EW index. In terms of (1.22) the general Higgs potential in (1.20) can be written in the following form:

$$V = Y_{ab}(\Phi_a^\dagger \Phi_b) + \frac{1}{2} Z_{abcd}(\Phi_a^\dagger \Phi_b)(\Phi_c^\dagger \Phi_d) \,, \tag{1.23}$$

where Y_{ab} and Z_{abcd}, constructed from the Higgs potential parameters, represent mass terms and quartic couplings respectively and the indices run from 1 to 2. The basic objects used here $(\Phi_a^\dagger \Phi_b)$ are EW scalar products of doublets Φ_a and Φ_b so that $(\Phi_a^\dagger \Phi_b)$ is a 2-by-2 matrix and has no EW indices. The number of free parameters that the tensor Z_{abcd} involves in tensors is restricted by the constraint (symmetry)

$$Z_{abcd} = Z_{cdab} \,. \tag{1.24}$$

Hermiticity of V also implies

$$Y_{ab} = (Y_{ba})^* , \quad Z_{abcd} = (Z_{badc})^* . \tag{1.25}$$

All in all, these relations reduce the number of parameters to 14 as it has to be (4 from Y_{ab} and 10 from Z_{abcd} .

In order to guarantee that the vacuum respects the electromagnetic gauge symmetry, only neutral components of the doublets acquire non-zero VEVs [91]:

$$\langle \Phi_1^0 \rangle = \frac{v}{\sqrt{2}} \hat{v}_1 , \quad \langle \Phi_2^0 \rangle = \frac{v}{\sqrt{2}} \hat{v}_2 \,, \tag{1.26}$$

where $\hat{v_a} = (\hat{v}_1, \hat{v}_2)$ is a vector of unit norm in the space of doublets. With the aid of (1.20) and taking the derivative of (1.23) with respect to Φ_b, the covariant form for the scalar potential extremum conditions reads

$$\hat{v_a}(Y_{ab} + \frac{1}{2} v^2 Z_{abcd} \hat{v_c}^* \hat{v_b}) = 0 \,. \tag{1.27}$$

These coupled equations, unfortunately, cannot be solved explicitly which shows that in the general 2HDM nothing can be done at the algebraic level, as it is done in the SM (or

in constrained versions of the 2HDM). Of course a numerical approach could be followed, but with 14 parameters to consider the task is far from trivial. There are indeed some papers where this approach is used to study the symmetries of the vacuum [98] or the masses of the Higgs bosons [99], but the results are far from conclusive.

A method shielding light on this problem is therefore of crucial importance, and in fact such an observation has lead to the development of the techniques discussed in the next Section.

1.2.4 Approaches to the general 2HDM

The basis independent treatment of the 2HDM [91–93, 100–102] is based on the tensorial decomposition in (1.23), where Y_{ab} and Z_{abcd} are considered as tensors rather than just a collection of parameters. Algebraic independent basis-invariants are constructed as full contractions of the available tensors. These basis-invariants then providing informations about some of the properties the model exhibits (see e.g. [91] for a comprehensive review). The technique, though powerful, does not yield hand-able results, thus not allowing for an intuitive interpretation of the output expressions which generally—at the end—have to be manipulated computationally.

The orbit space technique, based on the reparametrization freedom of the theory [94, 95], is a more appealing and—probably—more powerful description, as it allows a much more intuitive understanding of the 2HDM properties. The realization that the reparametrization group rather than being $SU(2)$, as commonly accepted, is $GL(2,C)$ allows the construction of the Minkowski space structure of the 2HDM orbit space, from which a deeper understanding of the 2HDM is gained. In what follows these techniques will be discussed. Rather than providing a comprehensive treatment, the main aspects and features, in particular those needed/used in Chapter 2 will be presented. For throughout details the reader is referred to [94, 95].

1.2.5 The orbit space of the 2HDM

The scalar potential, defined in the 8-dimensional space of scalar fields, depends on the bilinear EW invariants $(\phi_i^\dagger \phi_j)$. A point in the space of Higgs fields can be mapped into one other via an $SU(2) \otimes U(1)$ transformation. The set of all points connected through such a transformation define an orbit, and have the feature of being undistinguishable. The set of all possible orbits, in turn, defines the orbit space.

With orbits classified according to $SU(2) \otimes U(1)$ transformations, the natural choice for the reparametrization group will be $SU(2)$, and indeed this was the case until the analysis from [94, 95] where—as already pointed out—it was shown that the most general reparametrization group corresponds to $SL(2,C) \subset GL(2,C)$. This reparametrization group reveals the Minkowski space structure of the orbit space, due to its homomorphism with the proper (restricted) Lorentz group. This can be readily done by decomposing the bilinears $(\Phi_a^\dagger \Phi_b)$ (see Eq. (1.22)) in the $SU(2)$ subset adjoint representation: $2 \otimes 2 = 3 \oplus 1$, which then implies the bilinears can be decomposed into a $SU(2)$ singlet and triplet [94]:

$$r_0 = (\Phi^\dagger \Phi) = (\phi_1^\dagger \phi_1) + (\phi_2^\dagger \phi_2) \tag{1.28}$$

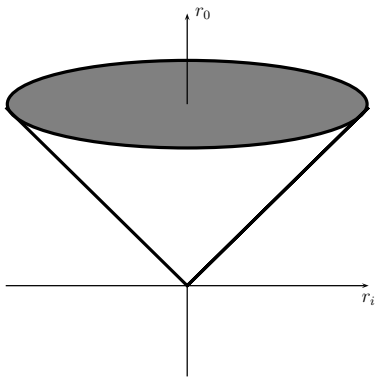

Figure 1.4: *The orbit space of 2HDM, lying along or within the Minkowski future light-cone as required by* $r^\mu r_\mu > 0$.

and

$$r_i = (\Phi^\dagger \sigma_i \Phi) = \begin{pmatrix} (\phi_2^\dagger \phi_1) + (\phi_1^\dagger \phi_2) \\ -i((\phi_1^\dagger \phi_2) - (\phi_2^\dagger \phi_1)) \\ (\phi_1^\dagger \phi_1) - (\phi_2^\dagger \phi_2) \end{pmatrix} = \begin{pmatrix} 2\mathbb{R}\mathrm{e}(\phi_1^\dagger \phi_2) \\ 2\mathbb{I}\mathrm{m}(\phi_1^\dagger \phi_2) \\ |\phi_1|^2 - |\phi_2|^2 \end{pmatrix} . \tag{1.29}$$

The scalar r_0 and vector r_i can then be identified with an irreductible representation of $SO(1,3)$, namely

$$r^\mu = (r_0, r_i) , \tag{1.30}$$

thus providing the Minkowski space structure of the 2HDM orbit space, where of course covariant and contravariant vectors (tensors) are related through the Minkowski space metric: $g_{\mu\nu} = \mathrm{diag}(1,-1,-1,-1)$. Although having a Minkowski space, as required by the positiveness of $r^2 = r^\mu r_\nu \geq 0$. From which it becomes clear that the field configurations are in or within the Minkowski future-light-cone (LC^+) as illustrated in Figure 1.4. In terms of the $SO(1,3)$ irreductible representations the scalar potential in (1.21) can be recasted in a compact way [94, 96]:

$$V = -B_\mu r^\mu + \frac{1}{2}\Lambda_{\mu\nu} r^\mu r^\nu , \tag{1.31}$$

with the parameter tensors given by [96]

$$B_\mu = \mathrm{Tr}[\sigma_\mu Y] \quad \text{and} \quad \Lambda_{\mu\nu} = 4(\sigma_\mu)_{ab} Z_{abcd} (\sigma_\nu)^*_{cd} , \tag{1.32}$$

where the tensors Y and Z come from (1.23), for which explicit expressions for their components can be calculated by direct comparison of (1.23) and (1.21), and $\sigma_\mu = (\mathbb{I}_{2\times 2}, \sigma^i)$. Explicitly they read

$$B^\mu = \frac{1}{4}(m_{11}^2 + m_{22}^2, -2\mathbb{R}\mathrm{e}\, m_{12}^2, 2\mathbb{I}\mathrm{m}\, m_{12}^2, -m_{11}^2 + m_{22}^2) , \tag{1.33}$$

$$\Lambda_{\mu\nu} = \frac{1}{2}\begin{pmatrix} \frac{\lambda_1+\lambda_2}{2} + \lambda_3 & -\mathbb{R}\mathrm{e}(\lambda_6+\lambda_7) & \mathbb{I}\mathrm{m}(\lambda_6+\lambda_7) & -\frac{\lambda_1-\lambda_2}{2} \\ -\mathbb{R}\mathrm{e}(\lambda_6+\lambda_7) & \lambda_4 + \mathbb{R}\mathrm{e}\lambda_5 & -\mathbb{I}\mathrm{m}\lambda_5 & \mathbb{R}\mathrm{e}(\lambda_6-\lambda_7) \\ \mathbb{I}\mathrm{m}(\lambda_6+\lambda_7) & -\mathbb{I}\mathrm{m}\lambda_5 & \lambda_4 - \mathbb{R}\mathrm{e}\lambda_5 & -\mathbb{I}\mathrm{m}(\lambda_6-\lambda_7) \\ -\frac{\lambda_1-\lambda_2}{2} & \mathbb{R}\mathrm{e}(\lambda_6-\lambda_7) & -\mathbb{I}\mathrm{m}(\lambda_6-\lambda_7) & \frac{\lambda_1+\lambda_2}{2} - \lambda_3 \end{pmatrix} . \tag{1.34}$$

Positivity conditions

The tensor $\Lambda_{\mu\nu}$ has an important property, which originates from the positivity condition. The potential in (1.20) is stable if its quartic part V_4 increases in all directions in the entire ϕ_i-space. In other words, the positivity condition leads to inequalities between the coefficients λ_i in (1.21) (in the SM this is trivially satisfied by taking $\lambda > 0$). Such conditions were found explicitly only for simple potentials, for example for potentials with $\lambda_6 = \lambda_7 = 0$ [64]. For the most general case, nobody has found these explicit inequalities, because the most general case is algebraically very complicated. In the formalism described above, these conditions have to be imposed on $\Lambda_{\mu\nu}$: for potentials stable in a strong sense [7], in the orbit space, V_4 is positive definite if $\Lambda_{\mu\nu}$ is positive definite on and inside the LC^+, that is, $\Lambda_{\mu\nu} r_\mu r_\nu > 0$ on and inside the LC^+. As was proved in [103], this is equivalent to the statement that $\Lambda_{\mu\nu}$ is diagonalizable by an $SO(1,3)$ transformation and that after diagonalization it takes the form

$$\Lambda_{\mu\nu} = \mathrm{diag}(\Lambda_0, -\Lambda_1, -\Lambda_2, -\Lambda_3) \quad \text{with} \quad \Lambda_0 > 0, \quad \Lambda_0 > \Lambda_i\,, \; i = 1,2,3\,, \tag{1.35}$$

where the inequalities among the eigenvalues result from the positivity constraint on the potential. The minus signs in front of the "space-like" eigenvalues arise from the pseudo-Euclidean Minkowski metric of the orbit space. It is obvious that if $\Lambda_{\mu\nu}$ satisfies this condition, the positive definiteness is assured. On the other side, it has been proved in [103] that this condition follows from the positive definiteness of $\Lambda_{\mu\nu}$. Finding the eigenvalues explicitly in terms of λ_i requires solving the fourth order characteristic equation, which constitutes one of the computational difficulties of the algebraic approach. However, fortunately these explicit expressions are never used and only the eigenvalues of $\Lambda_{\mu\nu}$ are needed.

Vacua in the 2HDM

Using the technique introduced in the previous discussion, the vacuum structure of the scalar potential can be much more easily analyzed. The minimization of the scalar potential can be rewritten (translated) in the orbit space and the ground state can be studied without finding explicitly its location [94, 95].

The extrema of the potential define the fields ϕ_i VEVs $\langle\phi_i\rangle$:

$$\left(\frac{\partial V}{\partial \phi_i}\right)_{\phi_i=\langle\phi_i\rangle} = 0\,, \quad \left(\frac{\partial V}{\partial \phi_i^\dagger}\right)_{\phi_i=\langle\phi_i\rangle} = 0\,. \tag{1.36}$$

Different kinds of vacuum states with various physical properties are possible (EW symmetry conserving solution $\langle\phi_i\rangle = 0$ or several EWSB solutions) depending on the interrelation among parameters [65]. Indeed, using the CP-phase freedom of the Lagrangian

7. Here the terminology of [91, 92]. is used: the potential is stable in a strong sense, if its quartic part increases along all rays starting from the origin in the Higgs field space. The potential is called stable in a weak sense, if the quartic part has flat directions, but the quadratic potential increases along them. For the Minkowski-space analysis of potentials stable in a weak sense, see [103], where a similar condensed-matter problem was considered.

and in choosing appropriately the third isospin axis, the most general EWSB VEV can be written in the form:

$$\langle\phi_1\rangle = \frac{1}{\sqrt{2}}\begin{pmatrix} 0 \\ v_1 \end{pmatrix}, \quad \langle\phi_2\rangle = \frac{1}{\sqrt{2}}\begin{pmatrix} u \\ v_2 e^{i\xi} \end{pmatrix}, \tag{1.37}$$

where v_1 and v_2 are real. With the quantum numbers of the scalar EW doublets the Gell-Mann-Nishijima formula, $Q = Y/2 + I_3$, clearly shows $u \neq 0$ ($u = 0$) corresponds to a charge breaking (conserving) vacuum. Accordingly, the potential in (1.31) exhibits three different kinds of minima: (*i*) EW conserving; (*ii*) EW breaking and charge conserving; (*iii*) EW and charge breaking. The four-vector VEVs configurations yielding such minima are correspondingly $\langle r^\mu\rangle = 0$ (the apex of the LC^+), $\langle r^\mu\rangle \neq 0$ but $\langle r^\mu\rangle\langle r_\mu\rangle = 0$ (the surface of the LC^+), $\langle r^\mu\rangle \neq 0$ and $\langle r^\mu\rangle\langle r_\mu\rangle > 0$ (the interior of the LC^+).

Given that the most interesting, and actually needed, situations are those leading to EWSB, in what follows the conditions ensuring these extrema are discussed (details can be found in [94]). As stressed charge-breaking as well as charge-conserving extrema are possible. In the former case, their position (denoted by $\langle r_\nu\rangle_{\rm ch}$) is determined by the minimization condition

$$\Lambda^{\mu\nu}\langle r_\nu\rangle_{\rm ch} = B^\mu\,, \tag{1.38}$$

which arises by enforcing the partial derivative of the potential in (1.21) to vanish. A solution to (1.38) exists provided $\Lambda^{\mu\nu}$ is not singular, namely

$$\langle r_\nu\rangle_{\rm ch} = b_\nu \equiv (\Lambda^{-1})_{\nu\mu}B^\mu\,. \tag{1.39}$$

Shifting the minimum to zero, the potential in (1.21) can be recasted as follows:

$$V = \frac{1}{2}\Lambda_{\mu\nu}(r^\mu - b^\mu)(r^\nu - b^\nu) + C\,, \tag{1.40}$$

with C a constant. The condition for the existence of a minimum (bounded from below potential) then implies

$$\Lambda_{\mu\nu}(r^\mu - b^\mu)(r^\nu - b^\nu) > 0 \quad \forall \quad (r^\mu - b^\mu)\,, \tag{1.41}$$

meaning that the charge-breaking stationary point is a minimum if and only if $\Lambda_{\mu\nu}$ is definite positive in the entire Minkowski space, which according to the previous discussion (positivity conditions) requires $\Lambda_i > 0$ for $i = 1, 2, 3$. As for the charge-conserving extremum the minimization condition involves a Lagrange multiplier (in order to guarantee the solutions lie along the light-cone surface). Consequently, the positions of all neutral extrema $\langle r^\mu\rangle$ are the solutions of the following simultaneous equations:

$$\Lambda^{\mu\nu}\langle r_\nu\rangle - \xi^\mu = B^\mu\,, \quad \xi^\mu \equiv \xi\langle r^\mu\rangle\,. \tag{1.42}$$

where ξ is the Lagrange multiplier. This system can have up to six solutions [91,92,94,104], among which there are at most two minima, while the other are saddle points [95].

Kinetic terms

Up to now nothing has been said about reparametrization invariance and the kinetic terms. In order to start with the discussion, first of all, the transformation properties of the kinetic term have to be derived (the discussion is carried out for the total derivative, the covariant derivative can be included in a straightforward way). Arranging the kinetic term according to $(\partial_\mu\Phi)^\dagger(\partial^\mu\Phi)$ it turns out to be clear that its transformation properties allow, as in the r_σ case, a $3\oplus 1$ decomposition (see Section 1.2.5) which then implies that the kinetic term can be recasted as [94]

$$\rho^\mu = (\partial_\mu\Phi)^\dagger\sigma^\beta(\partial^\mu\Phi)\,, \tag{1.43}$$

while β labels orbit space coordinates and μ refers to "guenine" space-time coordinates. Reparametrization invariance can be assured provided orbit space indices of a given expression are fully contracted, thus implying the reparametrization invariant kinetic term should be written as

$$K_\rho\rho^\rho, \tag{1.44}$$

with K_ρ the kinetic term clearly has a non-canonical form, enforcing a canonical form requires $K_\rho = (1,0,0,0)$, which then fixes a preferred frame.

1.3 Few comments on the 3HDM

1.3.1 The 3HDM

Until now the discussion has been limited to the 2HDM, mainly because the orbit space formalism can be readily described in a rather intuitive way avoiding most of its technicalities. Indeed, after this intuitive understanding is gained some features of the formalism can be readily extrapolated to more intricated cases involving more than two Higgs doublets, even to the general case of the N-Higgs-Doublet Model (NHDM) [105–107]. This Section does not aim to discuss such an ambitious framework, and though results from the NHDM will be somehow used in Chapter 3, instead some aspects of another specific multi-Higgs-doublet model will be covered, namely the 3HDM. At this point, it should be clear that a treatment of the 3HDM based on the conventional algebraic approach, where minimization conditions are worked out by brute force, will not render any useful conclusion. So, as in the 2HDM case, the orbit space method is expected to provide an appealing insight into the features of the scalar potential. From now on and based on the results from the previous Sections the orbit space of the 3HDM will be introduced, mainly aiming to settle the playground for Chapter 3.

1.3.2 The orbit space of the 3HDM

The 3HDM involves three EW doublets with identical EW quantum numbers, and, as in the 2HDM case, hypercharge is chosen as $Y = 1$:

$$\phi_i = \begin{pmatrix} w_i^+ \\ \frac{v_i+h_i+i\eta_i}{\sqrt{2}} \end{pmatrix}, \quad i = 1,2,3\,. \tag{1.45}$$

The total number of degrees of freedom is twelve of which, as usual, after EWSB three are absorbed by the EW gauge bosons thus leaving nine physical degrees of freedom in the spectrum: five electrically neutral and two electrically charged and their corresponding charge conjugated.

As in the 2HDM case, any simultaneous $SU(2)_L \otimes U(1)_Y$ transformations inside all doublets without changing the Lagrangian can be performed. In applying all possible such transformations to a point in the Higgs field space, the 12-dimensional space of Higgs fields is naturally "sliced" into non-intersecting orbits. The resulting set of orbits is the 8-dimensional orbit space. Indeed, using the phase freedom of the Lagrangian and choosing appropriately the third isospin axes, the most general EWSB VEVs can be written in the form:

$$\phi_1 = \begin{pmatrix} 0 \\ v_1 \end{pmatrix}, \quad \phi_2 = \begin{pmatrix} u_2 \\ v_2 e^{i\xi_2} \end{pmatrix}, \quad \phi_3 = \begin{pmatrix} u_3 e^{i\eta_3} \\ v_3 e^{i\xi_3} \end{pmatrix}. \tag{1.46}$$

Therefore, a point in the orbit space is defined by 8 real parameters. A point with $u_2 \neq 0$ or $u_3 \neq 0$ corresponds to the charge-breaking vacuum, whereas a point with $u_2 = 0$ and $u_3 = 0$ is a neutral vacuum and therefore the dimensionality of the neutral orbit space is equal to 5.

As in the most general 2HDM, the general renormalizable Higgs potential of 3HDM is constructed from the gauge-invariant bilinear combinations $(\phi_i^\dagger \phi_j)$ [108], which describe the gauge orbits in the Higgs space. The orbit space can be represented as a certain algebraic manifold in the space of these bilinears which is more complicated than the Minkowski space structure of the 2HDM orbit space. As in Section 1.2.5, it is convenient to decompose the bilinears according, in this case, to the $SU(3)$ product decomposition $\bar{3} \otimes 3 = 8 \oplus 1$, provided the scalar potential bilinears are constructed for the hyperspinor

$$\Phi_a = \begin{pmatrix} \phi_1 \\ \phi_2 \\ \phi_3 \end{pmatrix}, \quad a = 1, 2, 3\,. \tag{1.47}$$

With this decomposition it is now clear that [105–107]

$$\begin{aligned} r_0 &= \frac{1}{\sqrt{3}}(\Phi^\dagger \Phi) = \frac{1}{\sqrt{3}} \sum_i \phi_i^\dagger \phi_i\,, \\ r_i &= (\Phi^\dagger \lambda_a \Phi) = \sum_{i,j} \phi_i^\dagger (\lambda_a)_{ij} \phi_j\,, \quad a = 1, \ldots, 8\,. \end{aligned} \tag{1.48}$$

Explicitly the nine components read

$$\begin{aligned} &r_0 = \frac{(\phi_1^\dagger \phi_1) + (\phi_2^\dagger \phi_2) + (\phi_3^\dagger \phi_3)}{\sqrt{3}}\,, \; r_3 = \frac{(\phi_1^\dagger \phi_1) - (\phi_2^\dagger \phi_2)}{2}\,, \; r_8 = \frac{(\phi_1^\dagger \phi_1) + (\phi_2^\dagger \phi_2) - 2(\phi_3^\dagger \phi_3)}{2\sqrt{3}} \\ &r_1 = \mathrm{Re}(\phi_1^\dagger \phi_2)\,, \quad r_4 = \mathrm{Re}(\phi_3^\dagger \phi_1)\,, \quad r_6 = \mathrm{Re}(\phi_2^\dagger \phi_3)\,, \\ &r_2 = \mathrm{Im}(\phi_1^\dagger \phi_2)\,, \quad r_5 = \mathrm{Im}(\phi_3^\dagger \phi_1)\,, \quad r_7 = \mathrm{Im}(\phi_2^\dagger \phi_3)\,, \end{aligned} \tag{1.49}$$

where λ_a are the $SU(3)$ generators.

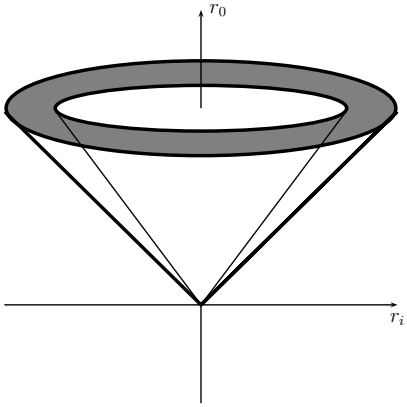

Figure 1.5: *The orbit space of* 3*HDM defined by two forward cones as determined by the* $SU(3)$ $\bar{3} \otimes 3$ *decomposition.*

With the results in (1.48) at hand, in particular the numerical factor entering in r_0, the shape of the 3HDM orbit space turns out to be determined by the following boundaries

$$r_0 \geq 0\,, \quad \frac{1}{4} r_0^2 \leq \vec{r}^2 \leq r_0^2\,, \tag{1.50}$$

which yield the geometrical representation illustrated in Figure 1.5. In addition, neutral vacua always lie on the surface of the outer cone $\vec{r}^2 = r_0^2$, while charge-breaking vacua lie strictly inside, $\vec{r}^2 < r_0^2$.

In the orbit space formalism, the Higgs scalar potential takes the form of a general quadratic form of r_0 and r_i:

$$\begin{aligned} V &= -M_0 r_0 - M_i r_i + \frac{1}{2}\Lambda_{00} r_0^2 + \Lambda_{0i} r_0 r_i + \frac{1}{2}\Lambda_{ij} r_i r_j\,. \\ &= -M_\mu r^\mu + \Lambda_{\mu\nu} r^\mu r^\nu \end{aligned} \tag{1.51}$$

The minimization of the potential can then be cast into a geometric condition of contact of two algebraic surfaces constructed in $\mathbb{R}^9$: the orbit space and the equipotential surfaces defined by $V = const$, see details in [106].

Summary

In this Chapter several subjects related with scalar sectors have been treated. For completeness, and also because the LHC results, the main aspects of the SM scalar sector as well as the corresponding SM Higgs phenomenology have been discussed. Motivations for extended scalar sectors have been presented, in particular motivations arising from phenomenological aspects for which the SM does not provide a successful description. Focusing on the 2HDM, the challenges of the scalar potential minimization and thus of the intrinsic problems when dealing with 2HDM phenomenology, have been emphasized. With this in mind, the orbit space method has been reviewed, highlighting its advantages and at the same time fixing the playground for the forthcoming discussion in Chapters 2 and 3.

CHAPTER 2

HIGGS MASSES OF THE GENERAL 2HDM

2.1 Introduction

In Chapter 1 the reparametrization symmetry inducing the Minkowski-space structure of the 2HDM orbit space was reviewed. Following this Minkowski-space approach, the geometric properties of the most general two-Higgs-doublet potential in the orbit space in Eq. (1.31) and its minima were investigated (see Section 1.2.5). This formalism is a powerful tool in the analysis of the existence and number of extrema of the scalar potential and their classification. The geometric constructions appear naturally in the orbit space and allow to prove various theorems concerning the number, the coexistence and the nature of the extrema, and also to find conditions for which the symmetry is broken and establish the phase diagram of the scalar sector of the 2HDM [94, 95]. The next step towards a comprehensive study of the general 2HDM consist in understanding its dynamics. This includes the mass spectrum of the physical Higgs bosons, the pattern of their interactions, as well as their couplings to the gauge bosons and fermions.

The dynamics of a quantum system can be expressed via the correlation functions. The scalar Lagrangian of the most general 2HDM, including a generic kinetic term, can be written in terms of the two complex EW doublets ϕ_1 and ϕ_2:

$$\mathcal{L} = K - V_2 - V_4 = (\partial_\alpha \phi_i)^\dagger K_{ij} (\partial^\alpha \phi_j) - \phi_i^+ B_{ij} \phi_j + \frac{1}{2} Z_{ijkl} (\phi_i^\dagger \phi_j)(\phi_k^\dagger \phi_l)\,. \tag{2.1}$$

Here all indices run from 1 to 2. After spontaneous EWSB these doublets acquire non-trivial VEVs, so that the physical scalar bosons φ_i can be introduced according to

$$\phi_i = \langle \phi_i \rangle + \varphi_i\,. \tag{2.2}$$

If the VEVs are known, this Lagrangian can be rewritten using the physical scalar fields:

$$\mathcal{L}(\phi_i, \partial_\alpha \phi_i) \to \mathcal{L}(\langle \phi_i \rangle + \varphi_i, \partial_\alpha \varphi_i)\,. \tag{2.3}$$

Then, using this Lagrangian, in principle various n-point correlation functions of physical scalar bosons can be calculated:

$$V_n(i_1, i_2, ..., i_n) = \langle 0 | T \varphi_{i_1}(x_{i_1}) ... \varphi_{i_n}(x_{i_n}) | 0 \rangle\,. \tag{2.4}$$

This notation is rather schematic because the n indices $i_1, ..., i_n$ do not only give the number of doublets, but also specify the fields. Besides, similar correlation functions with conjugate fields can be considered. The most important among them is the two-point correlation function V_2, that is, the propagator. Three-point and four-point correlation function V_3 and V_4 are given, at the tree level, by the couplings of the potential, while even higher order correlation functions are given by some specific convolutions of these. With V_2, V_3, V_4, Feynman rules of the model can be formulated and, in principle, any scattering process in the scalar sector can be calculated. These correlation functions, V_n, however, have the same important problem as the Lagrangian itself: their general form is redundant. Indeed, each V_n contains elements which depend on the basis for representing the Higgs fields, so they do not reflect the physical content of the model, but just depend on the way it is described. These elements, which are not basis-invariant, are unphysical. On the other hand, there are several basis-invariant combinations in each V_n, which are truly important for the physical content of the most general 2HDM. It is these invariant quantities that are aimed to be found. Unfortunately, it is very difficult to compute them working in the space of the scalar fields. A straightforward approach fails for the most general 2HDM, which calls upon more involved techniques for the analysis of its properties.

The mass spectrum of the general 2HDM was studied in a number of papers. If a restricted Higgs potential is chosen, for example, an explicitly CP-symmetric one, the entire calculation is drastically simplified. The minimum of the potential can be found explicitly and the masses and the interactions of the Higgs bosons calculated. For example, in [96,109,110] the mass matrix was explicitly calculated in a specific basis. An interesting study of the general 2HDM was presented in [99], where certain bounds and relations between the masses and the parameters of the potential were observed, however that work relied only on numerical analysis. Finally, a very detailed account of the dynamics of the general 2HDM was presented in [93] and in [9]. Among other results, explicit expressions of the mass matrix were derived in a $U(2)$-invariant way in terms of various full contractions of tensors Y_{ab} and Z_{abcd} introduced in (1.23) as well as vacuum expectation values. As has been seen in Chapter 1, this task is simplified if a shift from the space of Higgs fields to the orbit space is done. In this formalism, all basis-invariant quantities can be represented via full contractions of K_μ, $\Lambda_{\mu\nu}$ and B_μ (see Eq. (1.33), (1.34) and (1.43)) and invariant tensors $g_{\mu\nu}$ and $\epsilon_{\mu\nu\rho\sigma}$. Therefore, a natural task is to find these basis-invariant quantities. However, this is a very intricated and complex program which is not to be addressed here. Instead, in this chapter efforts focus on V_2, that is to say on the masses of the physical scalars degrees of freedom of the most general 2HDM.

The rest of this Chapter (based on [16]) is organized as follows: mass matrix related subjects are treated. First, the basis dependence (independence) of the mass matrix (mass spectrum) is discussed in a simple toy model and secondly the methods of the Minkowski space formalism for the mass spectrum is introduced. In Section 2.3, the mass-matrix for each possible 2HDM vacua is derived (see Section 1.2.5), and powers of the mass matrix traces are calculated in a reparametrization-covariant way.

2.2 Mass matrix and mass spectrum

2.2.1 Mass related basis-invariants and non-invariants in a toy model

In order to illustrate the essence of the task, a very simple model is considered: a free scalar theory with two complex scalars. An important fact is that the mass matrix itself is a basis-dependent quantity. Consider the Lagrangian for two complex scalar fields, ϕ_1 and ϕ_2, in matrix form:

$$\mathcal{L}_\phi = K - V = \sum_{i=1,2} \left[(\partial_\mu \phi_i)^\dagger (\partial^\mu \phi_i) - m_i^2 \phi_i^\dagger \phi_i \right] . \tag{2.5}$$

In this case there is no interaction between the fields ϕ_1 and ϕ_2, so that m_1^2 and m_2^2 represent the physical squared masses of these particles. As seen in Section **??** of Chapter 1, transformations from the reparametrization group $GL(2, C)$ of the Higgs fields modify the Higgs kinetic term. The full Higgs Lagrangian can therefore includes kinetic terms which can be off-diagonal in the general case. Therefore, a Lagrangian in the following general form is considered:

$$\mathcal{L} = (\partial_\alpha \phi_i)^\dagger K_{ij} (\partial^\alpha \phi_j) - \phi_i^\dagger B_{ij} \phi_j \, , \tag{2.6}$$

where the potential $V = \phi_i^\dagger B_{ij} \phi_j$ has an extremum at $\langle \phi_i \rangle = 0$. Now the mass matrix in two specific bases is derived and it is shown that they are different. First, the Lagrange equations from Lagrangian (2.6) is calculated:

$$\partial_\alpha \frac{\partial \mathcal{L}}{\partial (\partial_\alpha \phi_i)^\dagger} - \frac{\partial \mathcal{L}}{\partial \phi_i^\dagger} = 0 \, . \tag{2.7}$$

the following equations of motion are obtained:

$$K_{ij} \Box \phi_j + B_{ij} \phi_j = 0 \, . \tag{2.8}$$

If this equation is multipied by K^{-1}, it reads

$$\Box \phi_j + (K^{-1} B)_{ij} \phi_j = 0 \, . \tag{2.9}$$

Therefore, a set of Klein-Gordon equations for fields ϕ_i is obtained. Their mass matrix, in this basis, is

$$M_{ij} = (K^{-1} B)_{ij} \, . \tag{2.10}$$

Now the mass matrix is calculated in another way, by performing a transformation of the fields which makes the kinetic term of the Lagrangian (2.6) diagonal. So, a transformation on the fields is performed:

$$\phi_i \longrightarrow \tilde{\phi}_i = T_{ii'} \phi_{i'} \, , \quad \phi_i^\dagger \longrightarrow \tilde{\phi}_i^\dagger = \phi_{i'}^\dagger T_{i'i}^\dagger \, , \tag{2.11}$$

where T is some invertible 2-by-2 matrix, i.e. $T \in GL(2, C)$. The Lagrangian becomes:

$$\mathcal{L} = (\partial_\alpha \phi_{i'})^\dagger T_{i'i}^\dagger K_{ij} T_{jj'} (\partial^\alpha \phi_{j'}) - \phi_{i'}^\dagger T_{i'i}^\dagger B_{ij} T_{jj'} \phi_{j'} \, . \tag{2.12}$$

T is choosen so that the kinetic term becomes diagonal, that is, $T^\dagger K T = I$ and therefore $TT^\dagger = K^{-1}$. Therefore, in this new basis, the mass matrix becomes:

$$M'_{ij} = (T^\dagger B T)_{ij} \,. \tag{2.13}$$

Since matrices T and B do not necessarily commute

$$M_{ij} \neq M'_{ij} \,, \tag{2.14}$$

which confirms that the mass matrix is a basis dependent quantity. As a consequence, V_2 is also a basis-dependent quantity.

Nevertheless, it can be easily proved that the masses of the physical scalar bosons, m_1 and m_2, being the eigenvalues of the mass matrices, are the same for these two bases. Indeed, these masses can be calculated from the traces of powers of the mass matrix:

$$\mathrm{Tr}(T^\dagger B T) = \mathrm{Tr}(TT^\dagger B) = \mathrm{Tr}(K^{-1}B) \,. \tag{2.15}$$

Here the relation $TT^\dagger = K^{-1}$ and the cyclic property of the trace are used. So,

$$m_1^2 + m_2^2 = \mathrm{Tr}(M) = \mathrm{Tr}(M') \,. \tag{2.16}$$

The trace of the square of the mass matrix is also calculated:

$$\mathrm{Tr}(T^\dagger B T T^\dagger B T) = \mathrm{Tr}(TT^\dagger B T T^\dagger B) = \mathrm{Tr}(K^{-1}BK^{-1}B) \,, \tag{2.17}$$

so that

$$m_1^4 + m_2^4 = \mathrm{Tr}(M^2) = \mathrm{Tr}(M'^2) \,. \tag{2.18}$$

The same equality is also valid for any power of the mass matrices. It is noted that what is basis independent is the eigenvalues of the mass matrix. The determinant of the mass matrix can also be calculated via the traces,

$$\begin{aligned} 2\mathrm{Det}(M) &= [\mathrm{Tr}(M)]^2 - \mathrm{Tr}(M^2) = [\mathrm{Tr}(K^{-1}B)]^2 - \mathrm{Tr}(K^{-1}BK^{-1}B) \\ &= [\mathrm{Tr}(M')]^2 - \mathrm{Tr}(M'^2) \,. \end{aligned} \tag{2.19}$$

Therefore,

$$\mathrm{Det}(M) = \mathrm{Det}(M') = m_1^2 m_2^2 \,. \tag{2.20}$$

2.2.2 Masses in the Minkowski-space formalism

Anticipating work with 2HDM, the way the masses in this simple problem can be calculated in the four-vector formalism is illustrated. The Lagrangian (2.6) can be written, in the orbit space in a compact form as

$$\mathcal{L} = K - V = K_\mu \rho^\mu - B_\mu r^\mu \,, \tag{2.21}$$

where $\rho^\mu = (\partial_\alpha \Phi)^\dagger \sigma^\mu (\partial^\alpha \Phi)$. The minimum of the potential is at $\langle r^\mu \rangle = 0$, since $r^\mu = (\Phi^\dagger \sigma^\mu \Phi)$. The theory is thus reformulated using quantities defined in the orbit space. In particular, the following correspondence follows:

$$\begin{array}{ccccc} \text{degrees of freedom} & & (\phi_i, \phi_j) & \longrightarrow & r_\mu \\ \text{reparametrization group} & & SL(2,C) & \longrightarrow & SO(3,1) \\ \text{parameters} & & K_{ij}, B_{ij} & \longrightarrow & K_\mu, B_\mu \end{array} \tag{2.22}$$

What is the analogous table for the masses?

$$\begin{array}{rcccc} m_1^2+m_2^2 & : & \mathrm{Tr}(K_{ij}^{-1}B_{jm}) & \longrightarrow & ? \\ m_1^4+m_2^4 & : & \mathrm{Tr}(K_{ij}^{-1}B_{jk}K_{kl}^{-1}B_{lm}) & \longrightarrow & ? \end{array} \tag{2.23}$$

The matrix K_{ij} and B_{ij} are 2-by-2 Hermitian matrices, so they can be expressed in the covariant notation, using $\sigma_\mu = (\sigma_0, \sigma_a)$ with $\sigma_0 \equiv I$ and σ_a the Pauli matrices with $a = 1, 2, 3$, as

$$K_{ij} = K_\mu \sigma^\mu = K_0\sigma_0 - K_a\sigma_a \,, \tag{2.24}$$

$$B_{ij} = B_\mu \sigma^\mu = B_0\sigma_0 - B_a\sigma_a \tag{2.25}$$

where $K_\mu = (K_0, K_a)$ and $B_\mu = (B_0, B_a)$. This inverse of K_{ij} exists and can be written, using $\bar{\sigma_\mu} = (I, -\sigma_a)$, as

$$(K^{-1})_{ij} = \frac{(K^\mu \bar{\sigma}_\mu)_{ij}}{K^2} \,, \tag{2.26}$$

where $K^2 = K_\mu K^\mu = 1$. The traces of the mass matrix can now be calculated in the four-vector formalism.

$$\mathrm{Tr}(M) = \mathrm{Tr}(K^{-1}B) = \mathrm{Tr}\left(\frac{K^\mu\bar{\sigma}_\mu}{K^2}B^\nu\sigma_\nu\right) = \frac{K^\mu B^\nu}{K^2} Tr(\bar{\sigma}_\mu\sigma_\nu) \,. \tag{2.27}$$

Using $\mathrm{Tr}(\bar{\sigma}_\mu\sigma_\nu) = 2g_{\mu\nu}$ and $K^2 = 1$, it follows that:

$$\mathrm{Tr}(M) = m_1^2 + m_2^2 = 2K^\mu B_\mu = 2(KB) \,. \tag{2.28}$$

In order to calculate masses, $\mathrm{Tr}(M^2)$ needs to be derived.

$$\begin{aligned} \mathrm{Tr}(M^2) &= \mathrm{Tr}(K^{-1}BK^{-1}B) = \mathrm{Tr}(K^\mu\bar{\sigma}_\mu B^\nu\sigma_\nu K^\tau\bar{\sigma}_\tau B^\delta\sigma_\delta) \\ &= K^\mu B^\nu K^\tau B^\delta Tr(\bar{\sigma}_\mu\sigma_\nu\bar{\sigma}_\tau\sigma_\delta) \,. \end{aligned} \tag{2.29}$$

Using the following relation

$$\mathrm{Tr}(\bar{\sigma}^\mu\sigma^\nu\bar{\sigma}^\tau\sigma^\delta) = 2(g^{\mu\nu}g^{\tau\delta} - g^{\mu\tau}g^{\nu\delta} + g^{\mu\delta}g^{\nu\tau} - i\epsilon^{\mu\nu\tau\delta}) \,, \tag{2.30}$$

it eventually follows that

$$\mathrm{Tr}(M^2) = m_1^4 + m_2^4 = 2(KB)(KB) - K^2B^2 \,, \tag{2.31}$$

where $(KB) \equiv K_\mu B^\mu$. Now, the determinant can be calculated

$$\mathrm{Det}(M) = m_1^2m_2^2 = \frac{1}{2}\left[[\mathrm{Tr}(M)]^2 - \mathrm{Tr}(M^2)\right] = B^2 \,. \tag{2.32}$$

Now, as the trace and the determinant of the mass matrix are known, the masses themselves, m_1^2 and m_2^2, can be derived. To this end, the following system of equations need to be solved

$$m_1^2m_2^2 = B^2, \quad m_1^2 + m_2^2 = 2(KB) \,. \tag{2.33}$$

It follows that

$$m_1^2,\ m_2^2 = (KB) \pm \sqrt{(KB)^2 - B^2} \,. \tag{2.34}$$

The quantity $(KB)^2 - B^2$ is always positive because K_μ lies inside the LC^+. Indeed, this quantity is Lorentz-invariant which can calculated it in a particular frame in which $K_\mu = (1,0,0,0)$. In this frame, this quantity becomes $B_1^2 + B_2^2 + B_3^2 \equiv |\vec{B}|^2$, which is of course positive. Therefore, in this frame the masses take a simple form:

$$m_1^2,\ m_2^2 = B_0 \pm |\vec{B}|\,. \tag{2.35}$$

Now conditions in terms of B^μ for which this is the minimum of the potential are derived. An extremum is a minimum if all the eigenvalues of the mass matrix, the squares of the particles masses, are positive. Therefore, it is a minimum if Det M > 0 and Tr$M > 0$. Looking at (2.35), both m_i^2 are positive if $B_0 > 0$ and $B_0 > |\vec{B}|$. It means that B^μ lies inside the LC^+. This is a basis-invariant statement. The phase transition happens when one of the eigenvalues becomes zero, that is Det$(M) = 0$. So, the phase transition takes place if

$$B_0^2 = B_1^2 + B_2^2 + B_3^2\,. \tag{2.36}$$

Therefore, the phase transition takes place on the surface of the forward light-cone.

2.3 Mass matrix of the most general 2HDM

The aim of this Section is to make a step towards fulfilling the study of the dynamics of the most general 2HDM in an reparametrization-covariant way. As illustrated previously, although the masses are physical observables and are reparametrization-invariant, the mass-matrix is basis-dependent. For intermediate calculations a switch back from the bilinears to the Higgs fields themselves is made, then the mass-matrix is derived in a specific basis, and finally, after some manipulations on the mass-matrix, the results are expressed in the Minkowski-space formalism.

The complex fields are denoted as $\phi_{i,\alpha}$, where $i = 1, 2$ indicates the doublet, while the index $\alpha = \uparrow, \downarrow$ indicates the upper and lower components in a given doublet. Then the 8-component real vector of scalar fields φ_a, $a = 1, ..., 8$, is introduced with the following components:

$$\varphi_a = (\mathbb{R}\mathrm{e}\phi_{1,\uparrow},\ \mathbb{I}\mathrm{m}\phi_{1,\uparrow},\ \mathbb{R}\mathrm{e}\phi_{2,\uparrow},\ \mathbb{I}\mathrm{m}\phi_{2,\uparrow},\ \mathbb{R}\mathrm{e}\phi_{1,\downarrow},\ \mathbb{I}\mathrm{m}\phi_{1,\downarrow},\ \mathbb{R}\mathrm{e}\phi_{2,\downarrow},\ \mathbb{I}\mathrm{m}\phi_{2,\downarrow})\ . \tag{2.37}$$

The four-vector r^μ can be rewritten in terms of φ_a as

$$r^\mu = \varphi_a \Sigma^\mu_{ab} \varphi_b\,. \tag{2.38}$$

Here, Σ^μ are four real symmetric 8-by-8 matrices; Σ^0 is just the unit matrix, while explicit form of Σ^i can be immediately reconstructed from the definitions in Appendix A. Since the upper and lower components of the doublets are not mixed by the Higgs potential, matrices Σ^μ have a block-diagonal form, composed of identical 4-by-4 matrices. Below, these 4-by-4 matrices will be used denoting them by the same letter Σ^μ. Which set of matrices is being used, 4-by-4 or 8-by-8, should be clear from the context. In contrast to σ^μ, the matrices Σ^μ do not form a closed algebra, but they belong to a larger algebra (Σ^μ, Π^μ), described in Appendix A. They also share with σ^μ an important property:

$$\left\{\Sigma^i, \Sigma^j\right\} = 2\delta^{ij} \cdot \mathbb{I}_8\,, \tag{2.39}$$

where brackets denote the anticommutator. It follows then that if a regular real symmetric 8-by-8 matrix A is written as $a_\mu \Sigma^\mu$, then its inverse is

$$A^{-1} = \frac{a_\mu \bar{\Sigma}^\mu}{a_\mu a^\mu}\,, \quad \bar{\Sigma}^\mu \equiv (\Sigma^0,\, -\Sigma^i)\,. \tag{2.40}$$

Below products of matrices Σ's and $\bar{\Sigma}$'s will be encountered. When simplifying these products, the following results prove useful:

$$\begin{aligned} &\frac{1}{2}(\Sigma^\mu \bar{\Sigma}^\nu + \bar{\Sigma}^\nu \Sigma^\mu) = g^{\mu\nu} \cdot \mathbb{I}_8\,, \\ &\frac{1}{2}\left(\Sigma^\mu \bar{\Sigma}^\rho \Sigma^\nu + \Sigma^\nu \bar{\Sigma}^\rho \Sigma^\mu\right) = g^{\mu\rho}\Sigma^\nu + g^{\nu\rho}\Sigma^\mu - g^{\mu\nu}\Sigma^\rho\,. \end{aligned} \tag{2.41}$$

With this notation, the formalism illustrated above can be used and a compact expression for the mass matrix in a specific basis can be given. The expansion of the scalar Lagrangian near an extremum is written as

$$\mathcal{L} \approx (K_\rho \Sigma^\rho_{ab})(\partial_\alpha \varphi_a)(\partial^\alpha \varphi_b) - H_{ab}(\varphi_a - \langle\varphi_a\rangle)(\varphi_b - \langle\varphi_b\rangle)\,, \quad H_{ab} \equiv \frac{1}{2}\frac{\partial^2 V}{\partial\varphi_a\,\partial\varphi_b}\,, \tag{2.42}$$

where the Hessian H_{ab} is calculated at the extremum. The 8-by-8 mass matrix can then be expressed as

$$\mathcal{M}_{ac} = (K_\rho \Sigma^\rho)^{-1}_{ab} H_{bc} = K_\rho \bar{\Sigma}^\rho_{ab} H_{bc}\,. \tag{2.43}$$

In the rest of this Section this mass matrix is calculated and its eigenvalues are analyzed for the three possible types of vacua mentioned in Section 1.2.5: electroweak-symmetric, charge-breaking and neutral.

2.3.1 Electroweak-symmetric vacuum

The masses of the Higgs bosons in the EW-symmetric vacuum are determined only by the quadratic term of the potential and can be easily calculated in a straightforward way. The eight masses are grouped into two quartets with values (1.21) are

$$m^2_{1,2} = \frac{1}{4}\left((-m^2_{11}) + (-m^2_{22}) \pm \sqrt{(m^2_{11} - m^2_{22})^2 + 4|m_{12}|^2}\right)\,. \tag{2.44}$$

These masses squared are positive, if $m^2_{11} < 0$, $m^2_{22} < 0$ and $m^2_{11} m^2_{22} > |m_{12}|^2$. However, it useful to work out this simple case in the reparametrization-covariant formalism just to illustrate how it works. The Hessian H_{ab} comes only from the $B_\mu r^\mu$ term of the potential in (1.31) and is equal to $-B_\mu \Sigma^\mu_{ab}$. The mass matrix is then

$$\mathcal{M}_{ab} = K_\rho(-B_\mu)(\bar{\Sigma}^\rho \Sigma^\mu)_{ab}\,. \tag{2.45}$$

Matrices Σ's have a block-diagonal form, and therefore so does the mass matrix (2.45). It is built of two identical 4-by-4 blocks $(\mathcal{M}_4)_{ab}$, with $a, b = 1, 2, 3, 4$, whose form is still given by the same expression but now with 4-by-4 matrices Σ^μ. In order to find its eigenvalues, mimicking what has been done in the previous section, the trace of its successive powers is calculated:

$$\mathrm{Tr}[\mathcal{M}_4] \;=\; K_\rho(-B_\mu)\mathrm{Tr}[\bar{\Sigma}^\rho \Sigma^\mu] = -4(KB)\,,$$

$$\begin{aligned}\mathrm{Tr}[(\mathcal{M}_4)^2] &= K_\rho(-B_\mu)K_{\rho'}(-B_{\mu'})\mathrm{Tr}[\bar{\Sigma}^\rho\Sigma^\mu\bar{\Sigma}^{\rho'}\Sigma^{\mu'}] \\ &= 2(KB)K_\rho B_\mu\mathrm{Tr}[\bar{\Sigma}^\rho\Sigma^\mu] - K_\rho K_{\rho'}B^2\mathrm{Tr}[\bar{\Sigma}^\rho\Sigma^{\rho'}] = 8(KB)^2 - 4K^2B^2\,, \\ \mathrm{Tr}[(\mathcal{M}_4)^n] &= -2(KB)\mathrm{Tr}[(\mathcal{M}_4)^{n-1}] - K^2B^2\mathrm{Tr}[(\mathcal{M}_4)^{n-2}]\,. \end{aligned} \tag{2.46}$$

These relations among the traces prove the mass matrix has only two independent eigenvalues. A simple analysis shows that there are two pairs of different eigenvalues, which are equal to

$$m^2_{1,2} = -(KB) \pm \sqrt{(KB)^2 - B^2}\,, \tag{2.47}$$

where the relation $K^2 = 1$ is used. This expression is reparametrization-invariant and can be calculated in any frame. In particular, in the original frame, where $K^\mu = (1,0,0,0)$, it reads

$$m^2_{1,2} = -B_0 \pm |\vec{B}|\,. \tag{2.48}$$

Using the definition of B^μ in (1.33), Eq. (2.44) can be immediately recovered and these masses can be calculated in terms of $m^2_{11}, m^2_{22}, m^2_{12}$. Indeed, from the expression for B^μ it follows that

$$|\vec{B}| = \frac{1}{4}(4|m^2_{12}|^2 + m^4_{11} + m^4_{22} - 2m^2_{11}m^2_{22})^{\frac{1}{2}}\,, \quad B_0 = \frac{1}{4}(m^2_{11} + m^2_{22})\,.$$

Therefore the masses become:

$$m^2_1,\ m^2_2 = -\frac{1}{4}(m^2_{11} + m^2_{22}) \pm \frac{1}{4}(4|m^2_{12}|^2 + m^4_{11} + m^4_{22} - 2m^2_{11}m^2_{22})^{\frac{1}{2}}. \tag{2.49}$$

The conditions in terms of B^μ when this is the minimum of the potential are: $\mathrm{Det}B > 0$ and $\mathrm{Tr}B > 0$. Looking at (2.48), both m^2_i are positive if $B_0 < 0$ and $|B_0| > |\vec{B}|$. Therefore, in order for the EW-symmetric extremum to be minimum, the four-vector B^μ must lie inside the backward-light-cone, LC^-.

2.3.2 Charge-breaking vacuum

Firstly, in what follows the mass matrix of the general 2HDM in the case of a charge-breaking vacuum is now derived. Using Eq.(1.39), the mass matrix can be calculated. According to (2.7), the second-derivative of the potential is first calculated:

$$\frac{\partial V}{\partial\varphi_a} = \frac{\partial r^\mu}{\partial\varphi_a}\frac{\partial V}{\partial r^\mu} = \frac{\partial r^\mu}{\partial\varphi_a}\cdot\xi_\mu\,. \tag{2.50}$$

where $\xi_\mu \equiv (-B_\mu + \Lambda_{\mu\nu}r^\nu)$. Therefore,

$$\left(\frac{\partial^2 V}{\partial\varphi_a\partial\varphi_b}\right)_{\mathrm{ch}} = \left(\frac{\partial^2 V}{\partial\varphi_a\partial\varphi_b}\right)_{\xi_\mu=0} = \frac{\partial r^\mu}{\partial\varphi_a}\frac{\partial r^\nu}{\partial\varphi_b}\Lambda_{\mu\nu}\,. \tag{2.51}$$

Therefore the Hessian has the following form:

$$H_{bc} = 2\Lambda_{\mu\nu}\Sigma^\mu_{bb'}\Sigma^\nu_{cc'}\varphi_{b'}\varphi_{c'}\,. \tag{2.52}$$

Then, the second derivative of the kinetic term, which gives the same result as before, is computed:

$$\frac{\partial^2 L}{\partial(\partial_\alpha\varphi_a)\partial(\partial_\alpha\varphi_b)} = K_\mu\Sigma^\mu_{ab} = K_{ab}\,. \tag{2.53}$$

All fields here must be understood as VEVs $\langle\varphi_a\rangle$, but to keep the notation simple, the brackets will be suppressed. Thus, the mass matrix can be written as

$$\mathcal{M}_8 = 2K_\rho\Lambda_{\mu\nu}\bar{\Sigma}^\rho\Sigma^\mu(\varphi\otimes\varphi)\Sigma^\nu\,. \tag{2.54}$$

By construction, this is a 8-by-8 matrix. However, it must have four flat directions corresponding to the Goldstone modes. Now to get rid of these four flat directions it can be shown that there exists a 4-by-4 matrix $\mathcal{M}_4$ such that trace of any power of $\mathcal{M}_8$ is equal to the trace of the same power of $\mathcal{M}_4$. The trace of $\mathcal{M}_8$ is considered. Using Eq. (1.39) and the properties of Σ's it reads

$$\begin{aligned}\mathrm{Tr}\left[\mathcal{M}_8\right] &= 2K_\rho\Lambda_{\mu\nu}\,\varphi\Sigma^\nu\bar{\Sigma}^\rho\Sigma^\mu\varphi = 2K_\rho\Lambda_{\mu\nu}\left(g^{\mu\rho}b^\nu + g^{\nu\rho}b^\mu - g^{\mu\nu}b^\rho\right)\\ &= 2K_\rho b_\mu\left(2\Lambda_{\rho\mu} - \mathrm{Tr}\Lambda\, g_{\rho\mu}\right) \equiv 2\mathrm{Tr}\left[S\cdot\Lambda\right]\,,\end{aligned} \tag{2.55}$$

where the cyclic property of the trace is used and the antisymmetric part of $\Sigma^\nu\bar{\Sigma}^\rho\Sigma^\mu$ is neglected since $\Lambda_{\mu\nu}$ is symmetric. Here, the matrix $S\cdot\Lambda$ is a symbolic form of the tensor $S^\mu{}_\alpha\Lambda_{\alpha\nu}\equiv S^{\mu\alpha}\Lambda_{\alpha\nu}$, where

$$S^{\nu\mu} \equiv K^\nu b^\mu + K^\mu b^\nu - (Kb)g^{\nu\mu}\,. \tag{2.56}$$

The matrix $S\cdot\Lambda$ is defined in the euclidean space, and although it contains the tensors $S^{\mu\alpha}$ and $\Lambda_{\alpha\nu}$, they are contracted according to the usual rules of matrix multiplication. The trace of the square of $\mathcal{M}_8$ is now considered:

$$\mathrm{Tr}\left[(\mathcal{M}_8)^2\right] = 4K_\rho\Lambda_{\mu\nu}K_{\rho'}\Lambda_{\mu'\nu'}\cdot\varphi\Sigma^\nu\bar{\Sigma}^{\rho'}\Sigma^{\mu'}\varphi\cdot\varphi\Sigma^{\nu'}\bar{\Sigma}^\rho\Sigma^\mu\varphi\,. \tag{2.57}$$

This expression does not factorize because $\Lambda_{\mu\nu}$ and $\Lambda_{\mu'\nu'}$ couple the first and the second threads of Σ's. For example, if one of these threads is considered

$$\varphi_a(\Sigma^\nu\bar{\Sigma}^{\rho'}\Sigma^{\mu'})_{ab}\varphi_b\,. \tag{2.58}$$

This is a quadratic form in φ_a; therefore, only the ab-symmetric part of the product of Σ's survives. This effectively leads to the $\nu\leftrightarrow\mu'$ symmetrization, and (2.41) can again be applied to obtain

$$K_{\rho'}\varphi_a\left(\Sigma^\nu\bar{\Sigma}^{\rho'}\Sigma^{\mu'}\right)_{ab}\varphi_b = S^{\nu\mu'}\,. \tag{2.59}$$

The trace of the square of the mass matrix is then

$$\mathrm{Tr}\left[(\mathcal{M}_8)^2\right] = 4\Lambda_{\mu\nu}S^{\nu\mu'}\Lambda_{\mu'\nu'}S^{\nu'\mu} = \mathrm{Tr}\left[(2S\cdot\Lambda)^2\right]\,. \tag{2.60}$$

This calculation is easily generalizes to any power of the mass matrix:

$$\mathrm{Tr}\left[(\mathcal{M}_8)^n\right] = \mathrm{Tr}\left[(2S\cdot\Lambda)^n\right]\,. \tag{2.61}$$

The fact that the trace of any power of $\mathcal{M}_8$ is equal to the trace of the same power of the 4-by-4 matrix $2S\cdot\Lambda$, means that there are four zero-modes in $\mathcal{M}_8$ and that all the four non-zero eigenvalues of $\mathcal{M}_8$ coincide with the eigenvalues of $2S\cdot\Lambda$. Thus, the four eigenvalues of the matrix $2S\cdot\Lambda$ gives the masses squared of the physical Higgs bosons in the charge-breaking vacuum.

There is no simple way to calculate the masses themselves. However, the product of all four masses squared can be easily inferred from the above expression:

$$\prod_i m_i^2 = \det(2S \cdot \Lambda) = 16 \det S \cdot \det\Lambda \,. \tag{2.62}$$

Both tensors here are written in the euclidean space. Determinant of euclidean $\Lambda^\alpha{}_\beta$ is the product of the eigenvalues [1] of Minkowski $\Lambda^{\mu\nu}$: $\det\Lambda = \Lambda_0\Lambda_1\Lambda_2\Lambda_3$. In order to calculate the other determinant, a closer look at $S^{\mu\nu}$ is taken. The way it is defined, Eq. (2.56), allows to immediately find its eigenvalues. Indeed, a reduced version of this tensor, $K^\mu b^\nu + K^\nu b^\mu$, is first considered. In general, K^μ and b^μ are non-parallel four vectors, both lying strictly inside the forward light-cone. Within the subspace spanned by them, two eigenvectors of this reduced tensor can be identified,

$$e^\mu_\pm = \frac{K^\mu}{\sqrt{K^2}} \pm \frac{b^\mu}{\sqrt{b^2}} \,, \quad e^\mu_+ e_{-\,\mu} = 0 \,, \tag{2.63}$$

whose eigenvalues are $(Kb) \pm \sqrt{K^2 b^2}$. Note that e^μ_+ lies inside the forward light-cone, while e^μ_- lies outside it. In addition, there are two eigenvectors in the subspace orthogonal to K^μ and b^μ, with zero eigenvalues. Since adding a term proportional to $g_{\mu\nu}$ does not change the eigenvectors but just shifts all the eigenvalues by a common constant, the following result is obtained: $S^{\mu\nu}$ is diagonalizable by an appropriate $SO(1,3)$ transformation, and after diagonalization it take form:

$$S^{\mu\nu} = \mathrm{diag}(S_0, -S_1, -S_2, -S_3) \,, \quad S_0 = \sqrt{b^2} \,, \; S_1 = -\sqrt{b^2} \,, \; S_2 = S_3 = -(Kb) \,. \tag{2.64}$$

Therefore it reads:

$$\prod_i m_i^2 = 16\Lambda_0(-\Lambda_1)(-\Lambda_2)(-\Lambda_3) \cdot b^2 (Kb)^2 \,. \tag{2.65}$$

As stressed in Chapter 1, a charge-breaking extremum exists, if b^μ lies inside the LC^+, i.e. if $b^2 > 0$ and $(Kb) > 0$. It is also known that the charge-breaking extremum is a minimum if the tensor $\Lambda^{\mu\nu}$ is positive-definite in the entire Minkowski space, i.e. if all its spacelike eigenvalues $\Lambda_{1,2,3}$ are negative [2]. Thus, all factors in (2.65) are positive.

Another observation concerns cases when the potential has an explicit symmetry. Consider, for example, the lowest possible explicit symmetry, a $\mathbb{Z}_2$-symmetry [3], which consists in reflection of, say, with axis r_2.This explicit symmetry means that $K_2 = 0$, $B_2 = 0$, and that $\Lambda_{2\mu} = 0$ for $\mu \neq 2$. It is known that the position of the charge-breaking minimum preserves all the discrete symmetries, so that m_2 is also zero. In this case the mass squared of the excitation that violates this symmetry can be immediately calculated:

$$m_2^2 = 2(-\Lambda_2)(bm) \,. \tag{2.66}$$

1. There is a subtlety here: in a generic basis, the eigenvalues of the Euclidean matrix $\Lambda^\alpha{}_\beta$, which is not even symmetric, are different from the eigenvalues of the Minkowski tensor $\Lambda^{\mu\nu}$, i.e. Λ_0 and Λ_i. However, the product of all the eigenvalues of these two matrices are equal.

2. These conditions can be also inferred from the positive-definiteness of the mass matrix just derived.

3. This symmetry is known in the literature as a generalized CP-symmetry. The "conventional $\mathbb{Z}_2$" corresponds, strictly speaking, to a $(\mathbb{Z}_2)^2$-symmetry of the potential, see details in [95].

2.3.3 Neutral vacuum

In the case of a neutral vaccum, as it has been emphasized in Chapter 1, the four-vector r^μ must lie on the surface of the forward light-cone (again, the brackets $\langle\cdots\rangle$, referring to the VEVs, are implicitly assumed) [94]. Therefore, the minimization procedure involves a Lagrange multiplier ζ, which brings up a new light-cone four-vector, ζ_μ, defined as $\zeta_\mu = \Lambda_{\mu\nu}r^\nu - B_\mu = \zeta\cdot r_\mu$, see Eq. (1.42). This new four-vector gives rise to an additional term in the mass matrix:

$$\mathcal{M}_8 = 2K_\rho\Lambda_{\mu\nu}\bar{\Sigma}^\rho\Sigma^\mu(\varphi\otimes\varphi)\Sigma^\nu + K_\rho\zeta_\mu\bar{\Sigma}^\rho\Sigma^\mu\,. \tag{2.67}$$

This matrix is again an 8-by-8 real symmetric matrix. However, it can easily be splitted into two 4-by-4 matrices corresponding to the charged (the first four components of φ_a) and neutral (the last four components of φ_a) modes, which do not mix. Essentially this expression for the mass matrix of the most general 2HDM, but with a trivial kinetic part, was obtained in other works, [93, 94, 109]. All these papers followed then the standard procedure: a switch to the basis where only the first doublet has non-zero VEV is made (the Higgs basis), and then the entries of the mass matrix can then be written in a simple way via the parameters of the potential in this specific basis as well as v^2. In this subsection, the basis-invariant features of the mass matrix will be written in an $SO(1,3)$-covariant way, without referring to any specific basis. The power of the covariant expression is that the result can be analyzed in any desired basis, e.g. in the $\Lambda_{\mu\nu}$-diagonal basis. In the canonical basis, the results reproduce those of [93, 94].

First the charged excitations are considered. Their masses arise solely from the last term in (2.67):

$$\mathcal{M}_4^{\rm ch} = K_\rho\zeta_\mu\bar{\Sigma}^\rho\Sigma^\mu\,, \tag{2.68}$$

where Σ's are now 4-by-4 matrices. Explicit calculations and the fact that $\zeta^2=0$, read

$$\mathrm{Tr}\mathcal{M}_4^{\rm ch} = 4(K\zeta)\,,\quad \mathrm{Tr}[(\mathcal{M}_4^{\rm ch})^2] = 8(K\zeta)^2\,,\quad \mathrm{Tr}[(\mathcal{M}_4^{\rm ch})^n] = 2[2(K\zeta)]^n\,. \tag{2.69}$$

It means that this matrix has only two non-zero eigenvalues, which are identical and equal to

$$m^2_{H^\pm} = 2(K\zeta)\,. \tag{2.70}$$

This implies, in particular, that in order for the extremum to be minimum, ζ must lie on the surface of the forward, not backward-light-cone.

For the neutral modes the same expression as in (2.67) is obtained, but with 4-by-4 matrices Σ^μ:

$$\mathcal{M}_4^{\rm n} = 2K_\rho\Lambda_{\mu\nu}\bar{\Sigma}^\rho\Sigma^\mu(\varphi\otimes\varphi)\Sigma^\nu + K_\rho\zeta_\mu\bar{\Sigma}^\rho\Sigma^\mu\,. \tag{2.71}$$

The trace of the mass matrix of the neutral Higgs bosons is calculated:

$$\begin{aligned}\mathrm{Tr}\mathcal{M}_4^{\rm n} &= 2K_\rho\Lambda_{\mu\nu}\varphi\Sigma^\nu\bar{\Sigma}^\rho\Sigma^\mu\varphi + 4(K\zeta) = 4\Lambda_{\mu\nu}K^\mu r^\nu - 2\mathrm{Tr}\Lambda\,(Kr) + 4(K\zeta)\\ &= 2(4\Lambda_{\mu\nu} - \mathrm{Tr}\Lambda\, g_{\mu\nu})K^\mu r^\nu - 4(KB)\,.\end{aligned} \tag{2.72}$$

Among the four neutral modes one Goldstone is expected, which makes the determinant of $\mathcal{M}_4^{\rm n}$ zero. To check it explicitly, the matrix $K_\rho\bar{\Sigma}^\rho$ is first factored out and then by a

direct calculation its determinant is checked to be equal to $(K_\mu K^\mu)^2 = 1$. The remaining determinant

$$\det\left[2\Lambda_{\mu\nu}\Sigma^\mu(\varphi\otimes\varphi)\Sigma^\nu + \zeta_\mu\Sigma^\mu\right] \tag{2.73}$$

is equal to zero, which can be best seen in the Higgs basis, where the second row and the second column have only zeros. In the generic basis, the Goldstone mode is $w_i = (\Pi^0)_{ij}\phi_j$, where the matrix Π^0 is the generator of the $SO(2)$ rotations between the real and imaginary parts (see Appendix A).

2.3.4 The extra symmetry of the neutral modes

The appearance of the tensor $4\Lambda_{\mu\nu} - \mathrm{Tr}\Lambda\, g_{\mu\nu}$ in (2.72) is not accidental, but reflects an extra symmetry of the neutral mass matrix. If the neutral vacuum is considered and only neutral excitations are analyzed, which correspond to the surface of the light-cone, only r^μ such that $g_{\mu\nu}r^\mu r^\nu = 0$ is considered. This means that if the tensor $\Lambda_{\mu\nu}$ is shifted in the potential as

$$\Lambda_{\mu\nu} \to \Lambda_{\mu\nu} + C g_{\mu\nu} \tag{2.74}$$

with an arbitrary C, the purely neutral contribution to the potential does not change, and neither does the neutral mass matrix. The tensor $4\Lambda_{\mu\nu} - \mathrm{Tr}\Lambda\, g_{\mu\nu}$ is precisely the combination that is invariant under such a shift. In terms of the original parametrization of the quartic potential (1.21), this symmetry means that the neutral Higgs boson masses do not depend on the value of $\mathrm{Tr}\Lambda = \lambda_3 - \lambda_4$.

This extra symmetry can be used to simplify the neutral Higgs boson mass matrix. First, the neutral mass matrix (2.71) is invariant under the transformation (2.74) thanks to the following relation:

$$2g_{\mu\nu}\Sigma^\mu(\varphi\otimes\varphi)\Sigma^\nu + r_\mu\Sigma^\mu = 0\,. \tag{2.75}$$

Then, since ζ_μ is proportional to r_μ: $\zeta_\mu = \zeta\cdot r_\mu$, where ζ is the Lagrange multiplier of the minimization problem the two terms in (2.71) can be grouped together:

$$\mathcal{M}_4^{\mathfrak{n}} = 2K_\rho\tilde{\Lambda}_{\mu\nu}\bar{\Sigma}^\rho\Sigma^\mu(\varphi\otimes\varphi)\Sigma^\nu \quad \text{where} \quad \tilde{\Lambda}_{\mu\nu} \equiv \Lambda_{\mu\nu} - \zeta g_{\mu\nu}\,. \tag{2.76}$$

It is remarkable that the new tensor $\tilde{\Lambda}_{\mu\nu}$ is itself invariant under (2.74) as this shift is accompanied by $\zeta \to \zeta + C$:

$$\zeta r^\mu \equiv \zeta^\mu = \Lambda^{\mu\nu}r_\nu - B^\mu \to (\Lambda^{\mu\nu} + Cg^{\mu\nu})r_\nu - B^\mu = \zeta^\mu + Cr^\mu = (\zeta + C)r^\mu\,. \tag{2.77}$$

With this expression at hand, the trick from the analysis of the charge-breaking vacuum can again be used and all the neutral boson masses are given by the eigenvalues of the following matrix written in a manifestly covariant form:

$$\tilde{\mathcal{M}}_4^{\mathfrak{n}} = 2\tilde{S}\cdot\tilde{\Lambda}\,, \quad \text{where} \quad \tilde{S}^\mu{}_\nu = K^\mu r_\nu + K_\nu r^\mu - (Kr)\delta^\mu_\nu\,. \tag{2.78}$$

Therefore, the trace of any power of the mass matrix can immediately be written as:

$$\mathrm{Tr}[(\mathcal{M}_4^{\mathfrak{n}})^k] = 2^k\tilde{S}^{\mu_1}{}_{\nu_1}\tilde{\Lambda}^{\nu_1}{}_{\mu_2}\cdots\tilde{S}^{\mu_k}{}_{\nu_k}\tilde{\Lambda}^{\nu_k}{}_{\mu_1}\,, \tag{2.79}$$

and the determinant of $\tilde{S}^\mu{}_\nu$ using (2.64) reads:

$$\det\tilde{S} = -r^2(Kr)^2 = 0\,, \tag{2.80}$$

which proves the existence of a Goldstone mode in a basis-invariant fashion.

CHAPTER 3

HIGHLY SYMMETRIC 3HDM

3.1 Introduction

As already mentioned in Chapter 1, many non-minimal Higgs sectors motivated by either theoretical-based or experimental results have been considered in the literature [111]. Typically, these sectors involve several Higgs fields subject to scalar interactions determined by a scalar potential, which is often invariant under a group of Higgs-family transformations. Once the potential is written, to a large extent, the analysis consists in minimizing it and finding the VEV alignment, then the potential has to be expanded near this point and finally the phenomenologically relevant quantities can be calculated. Models with extra EW doublets were motivated in Chapter 1, where it was shown that the orbit space formalism provides an appealing treatment of the 2HDM. However, despite being powerful, the complexity of the problem is such that a thorough analysis does not exist.

When analyzing scalar potentials beyond the SM, the complexity arises from the large number of parameters involved e.g. the most general 3HDM involves 54 parameters at the scalar potential level. So, of course, regardless of the method employed, deriving definite predictions in the most general cases is hopeless. However, in highly complex scenarios the orbit space formalism proves again to be a powerful approach provided the scalar potential is highly symmetric, which implies a significant reduction of the parameters involved. In this Chapter, it is shown to be the case by sticking to specific versions of the 3HDM where the scalar potential is invariant under either S_4 or A_4 Higgs transformations.

The structure of the Chapter, based on [17], is as follows: in Section 3.2 the main idea is formulated for convenience in the context of multi-Higgs-doublet models. The general construction is then illustrated in Section 3.3, where the S_4- and A_4-symmetric 3HDM is discussed in detail. In Section 3.4 various additional aspects of the method are discussed.

3.2 Geometric minimization of symmetric potentials

Although the method proposed is rather general and can be applied to a broad range of extended Higgs sectors and perhaps beyond, it is exposed in the context of NHDMs.

This method will allow to keep the notation simple and, at the same time, get prepared for the particular applications in 3HDM.

3.2.1 Geometric minimization: the main idea

The crucial feature of passing from fields to bilinears, reviewed in Chapter 1, is that the Higgs potential is simplified; it becomes a quadratic form of these new variables (see Eq. (1.31)). This transition was used in the 2HDM [108], and it has allowed to observe and exploit interesting geometric features of the potential both in 2HDM [94, 95] as detailed in Section 1.2 and in multi-Higgs-doublet models [106] briefly viewed in Section 1.3 in the Chapter 1. Here to go further in this direction, new variables in terms of which the potential becomes a linear function are introduced.

To this end, an NHDM potential with a sufficiently high symmetry so that $M_i = 0$ in (1.51) is considered. For the NHDM the potential has the same structure than (1.51), of course with $r_\mu = (\Phi^\dagger T^\mu \Phi)$ with T_μ the $SU(N)$ generators and Φ a N-component "hyper-spinor", for details see [105]. Absence of this term is a hallmark of so-called "frustrated symmetries" in NHDM which were discussed in [71]. The quartic part of the potential contains k different terms, k usually being rather small for a highly symmetric potential. The potential is generically written as

$$V = -M_0 r_0 + r_0^2 \sum_{i=0}^{k} \Lambda_i x_i \,. \tag{3.1}$$

Here x_i are the quartic terms divided by r_0^2, with $x_0 = 1$ by convention, and Λ_i are coefficients in front of them.

Now the variables x_i, which can always be chosen real, are considered. Calculating them for all possible field configurations (or for all possible values of r's inside the orbit space) fills a certain region in the space $\mathbb{R}^k$. This region, which is denoted by Γ, is the orbit space "squashed" into the x_i space. Note that the map from r's to x_i is not, generally speaking, injective because different r's can correspond to the same point x_i.

Suppose the geometric shape of Γ is known. Then the minimization of the potential proceeds in three simple steps. First, since the potential (3.1) is a linear function of x_i, the "direction of steepest descent" of the potential can be introduced, $\vec{n} = -(\Lambda_1 \,, \ldots \,, \Lambda_k)$. The potential can then be written as

$$V = -M_0 r_0 + r_0^2 \left(\Lambda_0 - \vec{n}\vec{x}\right) \,. \tag{3.2}$$

Then the minimum of the potential is achieved at the points of Γ which protrude farthest in the direction of $\vec{n}$. Once these points x_i are known, their realizations in terms of fields can be found, and, finally, the value of r_0 can be found. Note that the positivity conditions require that $\Lambda_0 - \vec{n}\vec{x} > 0$ everywhere in Γ.

Some phenomenologically relevant properties of the minima follow from this geometric picture, which is illustrated in Fig. 3.1 with a two-dimensional example. If Γ has a smooth and strictly convex local shape, Fig. 3.1a, then the minimum is unique in the x_i space. It is also seen that the minimum point continuously changes if parameters Λ_i are varied. If Γ, instead, has vertices, see Fig. 3.1b, then the minimum point becomes stable within certain regions of Λ_i variation (or alternatively, regions of possible directions of $\vec{n}$). Note

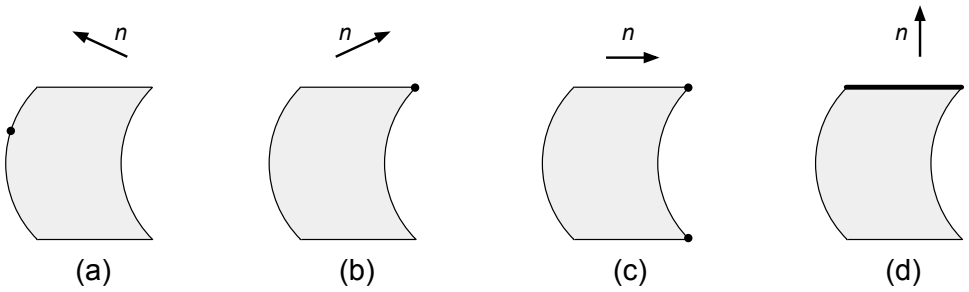

Figure 3.1: *Two-dimensional illustration of the geometric minimization method. Shown are four cases with the same orbit space* Γ *(represented by the shaded region) but with different values of the parameters* Λ_i*, which define the direction of steepest descent* $\vec{n}$*. The four cases show how the local geometry of* Γ *determines the stability and degeneracy of the global minimum; (a): locally convex geometry leads to a single global minimum indicated by the dot, whose position is sensitive to the exact values of* Λ_i*; (b): a minimum at a vertex is stable against variations of* Λ_i*; (c): cusps separated by a concave region allow two distinct minima to coexist and be degenerate; (d): straight segments can lead to a continuum of global minima (shown by a thick line) for the special values of the parameters, implying presence of massless bosons.*

that such a feature is the origin of geometric CP-violation in multi-doublet models, see the discussion in Section. 3.4.1. At the borders of these regions, two concurrent minima become degenerate and coexist, Fig. 3.1c; crossing this border causes a first order phase transition between the two vacuum configurations. Finally, if Γ contains straight segments, Fig. 3.1d, then for the borderline parameters Λ_i a continuum of global minima is obtained, which means that the model contains additional massless scalars.

In this picture, the key object becomes the shape of Γ rather than the parameters of the potential. Once the symmetry group is fixed and Γ is constructed, many properties of the potential (points of minimum, their degeneracy and coexistence, patterns of symmetry breaking, the phase diagram of the model and phase transitions) can be immediately read from its shape.

3.3 A_4- and S_4-symmetric 3HDM

In this Section an illustration of how the general method works with the example of A_4 and S_4-symmetric 3HDM is presented.

3.3.1 The potentials

The A_4-symmetric 3HDM can be represented by the following potential

$$\begin{aligned} V \;=\; & -\frac{M_0}{\sqrt{3}}\left(\phi_1^\dagger\phi_1+\phi_2^\dagger\phi_2+\phi_3^\dagger\phi_3\right)+\frac{\Lambda_0}{3}\left(\phi_1^\dagger\phi_1+\phi_2^\dagger\phi_2+\phi_3^\dagger\phi_3\right)^2 \\ & +\frac{\Lambda_3}{3}\left[(\phi_1^\dagger\phi_1)^2+(\phi_2^\dagger\phi_2)^2+(\phi_3^\dagger\phi_3)^2-(\phi_1^\dagger\phi_1)(\phi_2^\dagger\phi_2)-(\phi_2^\dagger\phi_2)(\phi_3^\dagger\phi_3)-(\phi_3^\dagger\phi_3)(\phi_1^\dagger\phi_1)\right] \\ & +\Lambda_1\left[(\mathbb{R}\mathrm{e}\phi_1^\dagger\phi_2)^2+(\mathbb{R}\mathrm{e}\phi_2^\dagger\phi_3)^2+(\mathbb{R}\mathrm{e}\phi_3^\dagger\phi_1)^2\right] \end{aligned}$$

$$+\Lambda_2\left[(\mathbb{I}\mathrm{m}\phi_1^\dagger\phi_2)^2+(\mathbb{I}\mathrm{m}\phi_2^\dagger\phi_3)^2+(\mathbb{I}\mathrm{m}\phi_3^\dagger\phi_1)^2\right]$$
$$+\Lambda_4\left[(\mathbb{R}\mathrm{e}\phi_1^\dagger\phi_2)(\mathbb{I}\mathrm{m}\phi_1^\dagger\phi_2)+(\mathbb{R}\mathrm{e}\phi_2^\dagger\phi_3)(\mathbb{I}\mathrm{m}\phi_2^\dagger\phi_3)+(\mathbb{R}\mathrm{e}\phi_3^\dagger\phi_1)(\mathbb{I}\mathrm{m}\phi_3^\dagger\phi_1)\right], \tag{3.3}$$

or, in terms of the bilinears defined in (1.49),

$$\begin{aligned} V &= -M_0 r_0+\Lambda_0 r_0^2+\Lambda_1(r_1^2+r_4^2+r_6^2)+\Lambda_2(r_2^2+r_5^2+r_7^2)+\Lambda_3(r_3^2+r_8^2) \\ &\quad +\Lambda_4(r_1r_2+r_4r_5+r_6r_7)\,. \end{aligned} \tag{3.4}$$

Here the parameters M_0 and Λ_i are assumed to take generic values. This potential is symmetric under the full achiral tetrahedral group T_d isomorphic to $A_4\rtimes\mathbb{Z}_2$ of order 24. This group is generated by independent sign flips of individual doublets, by cyclic permutations of the three doublets, as well as by a specific type of generalized-CP transformation (the CP-conjugation combined with exchange of any two doublets).

An alternative way to parametrize the potential was used in [112–114]. The coefficients introduced here are related with the coefficients of the alternative parametrization used in [114] as

$$-\frac{M_0}{\sqrt{3}}=\mu^2\,,\quad \Lambda_0=3\lambda_1+\lambda_3\,,\quad \Lambda_3=-\lambda_3\,,\quad \Lambda_{1,2}=\lambda_4\pm\lambda_5\cos\epsilon\,,\quad \Lambda_4=-2\lambda_5\sin\epsilon\,. \tag{3.5}$$

If $\Lambda_4=0$, the S_4-symmetric 3HDM is obtained. In the alternative parametrization, this is equivalent to setting $\epsilon=0$. The potential becomes now symmetric under the full achiral octahedral group O_h isomorphic to $S_4\times\mathbb{Z}_2$ of order 48, which is generated by sign flips of the individual doublets, by their permutations, and by the CP-conjugation.

The classification of the finite realizable symmetry groups of the scalar sector in 3HDM is now known [115]. The word realizable stresses that when imposing such a symmetry group, a potential that is exactly symmetric under this is obtained and restricting the parameters further will never produce any larger finite symmetry group. It can only lead to continuous symmetry groups, which are necessarily frustrated and must therefore be spontaneously broken and produce massless scalars [71]. This situation is disregarded on phenomenological grounds. It is therefore interesting to check what are the phenomenological consequences of such a high symmetry of the potential.

3.3.2 The toy model case

Before tackling the full problem in both scenarios, it is worth illustrating the method described in the previous Section by using a simplified toy model, as this will give insight about the subtleties expected.

Suppose only real-valued fluctuations in all three doublets are allowed ($r_2=r_5=r_7=0$). Then the potential simplifies to

$$V=-M_0r_0+r_0^2\left(\Lambda_0+\Lambda_1x+\Lambda_3z\right), \tag{3.6}$$

with the vector (x,z) playing the role of x_i where $x=n_1^2+n_4^2+n_6^2$ and $z=n_3^2+n_8^2$. It is clear from (1.50) that $x>0$, $z>0$, and $1/4\leq x+z\leq 1$, which defines a trapezoid shown in Figure 3.2. The four vertices of this trapezoid correspond to the following patterns of

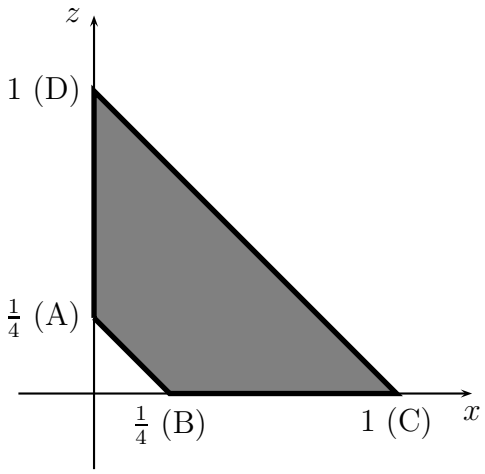

Figure 3.2: *The orbit space of the toy model projected on the* (x, z)*-plane.*

the three doublets (here only the relative magnitude of the VEVs are given):

$$\begin{aligned} D: &\quad \begin{pmatrix} 0 \\ 1 \end{pmatrix}, \begin{pmatrix} 0 \\ 0 \end{pmatrix}, \begin{pmatrix} 0 \\ 0 \end{pmatrix}; \\ C: &\quad \begin{pmatrix} 0 \\ 1 \end{pmatrix}, \begin{pmatrix} 0 \\ 1 \end{pmatrix}, \begin{pmatrix} 0 \\ 1 \end{pmatrix}; \\ A: &\quad \begin{pmatrix} 0 \\ 1 \end{pmatrix}, \begin{pmatrix} 1 \\ 0 \end{pmatrix}, \begin{pmatrix} 0 \\ 0 \end{pmatrix}; \\ B: &\quad \begin{pmatrix} 0 \\ 1 \end{pmatrix}, \begin{pmatrix} \sin\alpha \\ \cos\alpha \end{pmatrix}, \begin{pmatrix} \sin\beta \\ \cos\beta \end{pmatrix}; \end{aligned} \tag{3.7}$$

with $\alpha = -\beta = \frac{\pi}{3}$. The first two points correspond to neutral vacua while the last two are charge-breaking minima. All points inside this trapezoid are realizable by fields (in other words, when the full orbit space is projected on the (x, z)-plane, it covers the entire trapezoid).

The positivity have then to be derived. It is known from Chapter 1 that it is necessary and sufficient to require that the quartic part of the potential is positive inside the orbit space. Since the potential (3.6) is a linear function in x and z defined inside this trapezoid and therefore convex, it is sufficient to write the positivity conditions at the four vertices (3.7); then they will be automatically satisfied at all points inside the trapezoid. Thus, the positivity conditions for this toy model read:

$$\Lambda_0 + \Lambda_1 > 0\,, \quad \Lambda_0 + \Lambda_3 > 0\,, \quad 4\Lambda_0 + \Lambda_1 > 0\,, \quad 4\Lambda_0 + \Lambda_3 > 0\,. \tag{3.8}$$

In general, none of these inequalities can be removed because Λ_0 can be positive or negative. However, it is shown in [106] that in 3HDM the situation with $\Lambda_0 < 0$ always corresponds to the charge-breaking minimum. Therefore, since in this Chapter only neutral minima will be considered, the assumption that $\Lambda_0 > 0$ is made. In this case only the first two conditions in (3.8) are retained.

The global minima can now be found for different values of the parameters using the method explained previously. On the (x, z)-plane, the direction of steepest descent

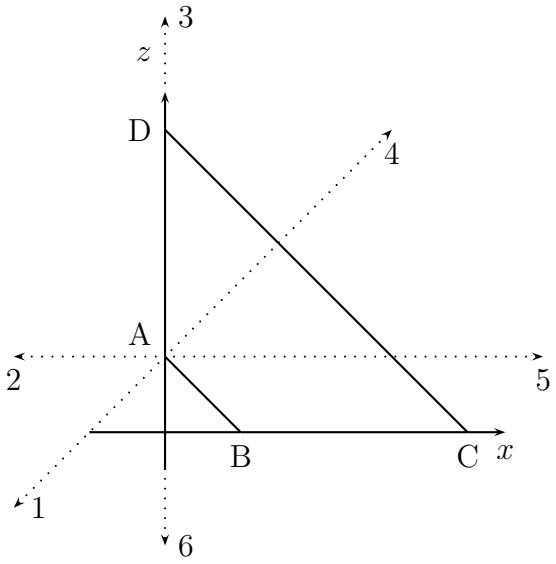

Figure 3.3: *Various possible directions of steepest descent and the corresponding minima.*

is given by vector $(-\Lambda_1, -\Lambda_3)$. By checking all possible directions of steepest descent, situations where vertices or edges of the trapezoid correspond to the global minimum (see Figure 3.3) are established. If the direction of steepest descent is parallel to direction 1, which happens at $\Lambda_1 = \Lambda_3 > 0$, then the entire edge AB corresponds to the global minimum. If the direction of steepest descent is between directions 1 and 2 ($\Lambda_1 > \Lambda_3 > 0$), point A is the minimum. When the direction of steepest descent is along direction 2 ($\Lambda_1 > 0, \Lambda_3 = 0$), all the points on the AD edge are minima. When the direction of steepest descent rotates further from direction 2 to direction 4, point D becomes the minimum. When the direction of steepest descent reaches direction 4 ($\Lambda_1 = \Lambda_3 < 0$), then all the points on the DC edge become minima of the potential. And so on. In this way, the full phase diagram of the model can be reconstructed in the Λ_i parameter space.

3.3.3 The orbit space in the S_4 case

The more restricted model, the S_4-symmetric 3HDM, is first presented. Written in terms of bilinears, the potential takes form

$$\begin{aligned} V &= -M_0 r_0 + \Lambda_0 r_0^2 + \Lambda_1(r_1^2 + r_4^2 + r_6^2) + \Lambda_2(r_2^2 + r_5^2 + r_7^2) + \Lambda_3(r_3^2 + r_8^2) \\ &= -M_0 r_0 + r_0^2(\Lambda_0 + \Lambda_1 x + \Lambda_2 y + \Lambda_3 z)\,, \end{aligned} \tag{3.9}$$

with the vector (x, y, z) playing the role of x_i, the definition of x, z are the same as in the toy model and $y = n_2^2 + n_5^2 + n_7^2$. The positivity conditions for the potential require that

$$\Lambda_0 + \Lambda_1 x + \Lambda_2 y + \Lambda_3 z > 0 \tag{3.10}$$

everywhere in the orbit space. Using the properties of bilinears mentioned in Section 1.3.2, the conclusion is that the three-dimensional orbit space Γ must lie inside the truncated pyramid defined by

$$x, y, z \geq 0\,, \quad \frac{1}{4} \leq x + y + z \leq 1\,, \tag{3.11}$$

meaning that the orbit space sits inside a 3-dimensional pyramid in the (x, y, z)-space but does not fill the entire pyramid. In addition, it turns out that $y \leq 3/4$. Indeed, y can be rewritten as

$$y = \frac{3}{4}\left[1 - \frac{2(\kappa_{12} + \kappa_{23} + \kappa_{31}) + Q_{\alpha\beta}Q^*_{\alpha\beta}}{(\rho_1 + \rho_2 + \rho_3)^2}\right], \tag{3.12}$$

where

$$\rho_a = (\phi_a^\dagger \phi_a) \geq 0\,, \quad \kappa_{ab} = \rho_a\rho_b - |\phi_a^\dagger \phi_b|^2 \geq 0\,, \quad Q_{\alpha\beta} = \sum_a \phi_a^\alpha \phi_a^\beta\,, \tag{3.13}$$

with $a = 1, 2, 3$ numbering the doublets and $\alpha, \beta = +, 0$ denoting the upper and lower components inside doublets. The largest value of y equal to $3/4$ is attained when, first, all $\kappa_{ab} = 0$ which selects the neutral vacuum, and then when the lower components of the doublets sum up as $\sum(\phi_a^0)^2 = 0$.

The exact shape of the orbit space which is found by numerical methods [1] is rather complicated, see Figure 3.4, left handside plot. It has the form of a wedge with the edge at $x + z = 1$, $y = 0$ and the convex backside at small values of $x + z$. However if only the phenomenologically relevant case of neutral vacuum is taken into account, then only one of its faces defined by $x + y + z = 1$ is to be considered. Indeed, as the potential is a linear function of x, y and z thus as already mentioned, the points on the border of the orbit space corresponds to the minima of the potential. If the potential is not a linear function of x, y and z, such as the A_4-symmetric potential detailed below, there could be other minima inside the orbit space and it requires further investigation. Here only the neutral minima are considered. They correspond to the points on the AB line in Figure(3.4)(b). The rest of Γ corresponds to charge-breaking vacua and is disregarded.

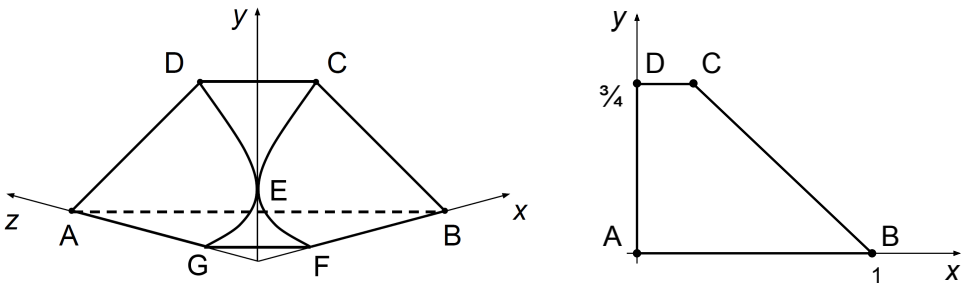

Figure 3.4: *Left: sketch of the orbit space* Γ *of the* S_4*-symmetric 3HDM in the* (x, y, z)*-space. Right: the neutral orbit space in the* (x, y)*-plain. On each plot, the four dots A, B, C, and D mark the positions of the possible neutral global minima.*

This neutral part of the orbit space has the shape of a trapezoid, which can be established analytically using (B.1) and (3.12). It is shown in Fig. 3.4, right, on the (x, y)-plane (with z defined as $z = 1 - x - y$).

The VEV alignments corresponding to the four vertices of the trapezoid are (here

1. One million points with random up and down components of the three doublets were generated. For each point the values of x, y, and z were calculated and then all points were plotted. By looking at the resulting 3D scatter plot from different angles, the shape is reconstructed and the sketch drawn in Figure 3.4.

again only the relative magnitude of the VEVs are given)

$$A:\ (1,0,0)\,,\quad B:\ (1,1,1)\,,\quad C=(e^{i\pi/3},e^{-i\pi/3},\pm1)\,,\quad D=(e^{i\pi/4},e^{-i\pi/4},0)\simeq(1,i,0)\,, \tag{3.14}$$

while the straight segments joining them are

$$\begin{aligned} &AB:\ (v_1,v_2,v_3) \text{ with all } v_i\in\mathbb{R}\,,\quad BC:\ (e^{i\xi_1},e^{i\xi_2},e^{i\xi_3})\,,\\ &AD:\ (v_1,iv_2,0) \text{ with all } v_i\in\mathbb{R}\,,\quad CD:\ (e^{i\xi},e^{-i\xi},r) \text{ with } \cos2\xi=-\frac{r^2}{2}\,. \end{aligned} \tag{3.15}$$

The details of the derivation of these points are given in Appendix B.1. Note that, in each case arbitrary permutations of the doublets are allowed. For example, vertex D corresponds to six degenerate minima $(1,\pm i,0),(1,0,\pm i),(0,1,\pm i)$.

3.3.4 Minimization of the S_4-symmetric potential

Applying the method of Section 3.2.1, the S_4-symmetric 3HDM can have only four types of neutral minima without producing massless scalars, which correspond to the vertices (3.14). Thus, all possible positions of the global minimum are located without the need to calculate any derivatives.

It is also possible to obtain conditions on Λ_i which lead to a minimum at each of these four points just by looking at the orbit space. For example, the VEV alignment of the type $(1,0,0)$ becomes the global minimum, when $\Lambda_3<0$ and $\Lambda_1,\Lambda_2>\Lambda_3$. When these conditions are satisfied, the point A indeed lies farthest along the direction $\vec{n}$. In addition, the positivity condition (3.10) in this case implies that $\Lambda_0+\Lambda_3>0$.

3.3.5 Unexpected symmetry of the orbit space

The S_4-symmetric 3HDM possesses a curious feature which could be noticed but would receive no explanation with the usual calculations.

The field content of the scalar sector, after EWSB, is the following: apart from the usual three "would-be" Goldstone bosons, there are two pairs of charge-conjugate Higges $H_i^\pm$, and five neutral scalars (see Section 1.2.3 for a more detailed counting). The oscillation mode in the direction of VEVs will be denoted as h, while the other neutral Higgses are generically labelled as H_i. In (generalized) CP-conserving cases, these can be additionally classified as (generalized) CP-even and CP-odd states.

The masses of the physical Higgs bosons are now calculated in the two VEV alignments: $(1,1,1)$ and $(1,0,0)$. In both cases $v^2\equiv v_1^2+v_2^2+v_3^2$ is used. The alignment $(1,1,1)$ becomes the global minimum of the potential if

$$\Lambda_1<0,\quad \Lambda_0>|\Lambda_1|>-\Lambda_2,-\Lambda_3\,. \tag{3.16}$$

The minimum point is then parametrized as $(v,v,v)/\sqrt{6}$ with

$$\begin{aligned} v^2&=\frac{\sqrt{3}M_0}{\Lambda_0-|\Lambda_1|}\,, \\ m^2_{H_i^\pm}&=\frac{1}{2}|\Lambda_1|v^2=\frac{\sqrt{3}M_0}{2}\,\frac{|\Lambda_1|}{\Lambda_0-|\Lambda_1|}\quad\text{(double degenerate)}\,, \end{aligned} \tag{3.17}$$

$$
\begin{aligned}
m^2_{H_i} &= \frac{1}{2}(|\Lambda_1| + \Lambda_2)v^2 = \frac{\sqrt{3}M_0}{2}\,\frac{|\Lambda_1| + \Lambda_2}{\Lambda_0 - |\Lambda_1|} \quad \text{(double degenerate)}\,, \\
&\quad \frac{1}{3}(|\Lambda_1| + \Lambda_3)v^2 = \frac{M_0}{\sqrt{3}}\,\frac{|\Lambda_1| + \Lambda_3}{\Lambda_0 - |\Lambda_1|} \quad \text{(double degenerate)}\,, \\
m^2_h &= \frac{2}{3}(\Lambda_0 - |\Lambda_1|)v^2 = \frac{2}{\sqrt{3}}M_0\,.
\end{aligned} \tag{3.18}
$$

The alignment $(1,0,0)$ becomes the global minimum if

$$
\Lambda_3 < 0, \quad \Lambda_0 > |\Lambda_3| > -\Lambda_2, -\Lambda_1\,. \tag{3.19}
$$

Expanding the potential around the point $(v,0,0)/\sqrt{2}$, reads

$$
v^2 = \frac{\sqrt{3}M_0}{\Lambda_0 - |\Lambda_3|}\,, \tag{3.20}
$$

$$
\begin{aligned}
m^2_{H_i^\pm} &= \frac{1}{2}|\Lambda_3|v^2 = \frac{\sqrt{3}M_0}{2}\,\frac{|\Lambda_3|}{\Lambda_0 - |\Lambda_3|} \quad \text{(double degenerate)}\,, \\
m^2_{H_i} &= \frac{1}{2}(|\Lambda_3| + \Lambda_2)v^2 = \frac{\sqrt{3}M_0}{2}\,\frac{|\Lambda_3| + \Lambda_2}{\Lambda_0 - |\Lambda_3|} \quad \text{(double degenerate)}\,, \\
&\quad \frac{1}{2}(|\Lambda_3| + \Lambda_1)v^2 = \frac{\sqrt{3}M_0}{2}\,\frac{|\Lambda_3| + \Lambda_1}{\Lambda_0 - |\Lambda_3|} \quad \text{(double degenerate)}\,, \\
m^2_h &= \frac{2}{3}(\Lambda_0 - |\Lambda_3|)v^2 = \frac{2}{\sqrt{3}}M_0\,.
\end{aligned} \tag{3.21}
$$

It is hard to miss a remarkable symmetry between these mass spectra: upon exchange $\Lambda_1 \leftrightarrow \Lambda_3$ they almost turn into one another. The only quantity that violates this otherwise perfect symmetry is the mass of one pair of neutral Higgses.

The bizarre aspect of this almost perfect symmetry is that it is not a symmetry of the model. It would be a symmetry if there existed a transformation of fields that could swap x and z while keeping y unchanged. But such transformation does not exist. This is also consistent with the fact that $\Lambda_1 \leftrightarrow \Lambda_3$ does not lead to an exact matching of the two Higgs spectra.

The origin of this near symmetry can be traced from the shape of the orbit space Γ in the (x,y,z) space. The numerical study offers very strong hints that this shape is indeed $x \leftrightarrow z$ symmetric; unfortunately, there is no analytic proof of this fact. Provided this is true, it explains why conditions (3.16) and (3.19) and the charged Higgs masses (which are also related with the shape of the orbit space) are exactly symmetric.

It is interesting to notice that, for both VEV alignments, the spectrum of the Higgs bosons is 2HDM-like. Namely, there are only one value for the charged Higgs masses and three values for neutral Higgs masses, just as expected for the generic 2HDM. How this situations can be distinguished from the true 2HDM experimentally, and which observable quantities should be looked at, is a separate issue worth investigating further. However the origin of this 2HDM-like spectra is different in these two cases. In the VEV alignment $(1,1,1)$ it comes form the unbroken S_3-symmetry of the model, [116], while for the $(1,0,0)$

alignment, the origin is the $O(2)$-symmetry mixing the second and third doublets, which is manifest in the VEVs and the mass terms. These two symmetry arguments are non-equivalent and cannot be related to each other. After all, the two VEV alignments also differ in the number of degenerate vacuum points: four for the $(1,1,1)$ and three for $(1,0,0)$.

The same relation holds between the other two possible VEV alignments, see Appendix B.2. It would be interesting to see if this approximate symmetry leads to other phenomenological similarities between these pairs of minima.

3.3.6 The orbit space in the A_4 case

The generic potential of the A_4-symmetric 3HDM (3.4) is written in the way suggested in Sec. 3.2.1:

$$V = -M_0 r_0 + r_0^2(\Lambda_0 + \Lambda_1 x + \Lambda_2 y + \Lambda_3 z + \Lambda_4 t)\,, \tag{3.22}$$

with the same x, y, z as in Eq. (3.9) and with $t = (r_1 r_2 + r_4 r_5 + r_6 r_7)/r_0^2$.

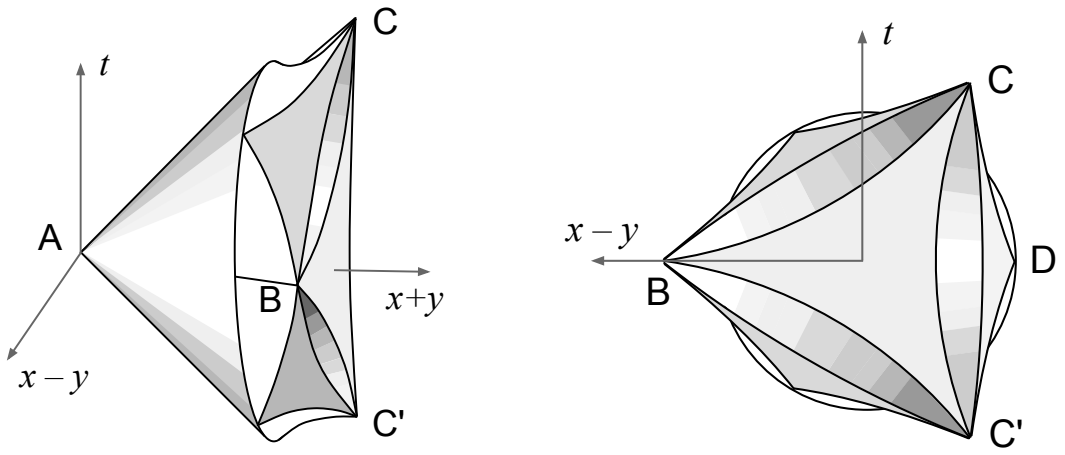

Figure 3.5: *Sketch of the neutral orbit space in the tetrahedral 3HDM viewed from two angles. Uniformly shaded regions correspond to flat faces, graded shading indicates curved faces.*

Again, the neutral orbit space Γ is considered, for which x, y, and t are chosen as independent variables, and then $z = 1-x-y$. The shape of Γ which arises from numerical study is shown in Fig. 3.5 in the (x, y, t) space. Despite being rather complicated, it displays a remarkable triangle symmetry. Basically, it is a right circular cone oriented along the direction $x - y = t = 0$ with the apex at the origin and with opening angle $\pi/2$ and with directrix lines of length 1. Parts of this cone starting from distance $3/4$ from the apex are carved out. It has four flat faces which have the shape of deltoid (3-vertex cusped closed curve). These are located at the bottom face (defined by $z = 0$) and at three side faces (one is $y = 3/4$ and the remaining two are obtained by the $2\pi/3$ rotation of the cone). Directrix lines opposite to these three side faces have length 1 and extend up to the points B, C and C' where three flat deltoid regions meet. The remaining portions of Γ are concave regions. The two-dimensional neutral orbit space for the S_4-symmetric model, Fig. 3.4, right, is simply the (x, y)-projection of this Γ; correspondence between

the vertex points in the two shapes should be clear. Point D, which was a vertex in the S_4 case, becomes a regular point on the rim of the cone in the A_4 case.

The conical shape of the orbit space can be understood in the following way. Two real vectors are introduced as

$$\vec{a} = \frac{1}{r_0}(r_1, r_4, r_6)\,, \quad \vec{b} = \frac{1}{r_0}(r_2, r_5, r_7)\,, \tag{3.23}$$

and the angle between them is denoted by ξ. Then, $x = \vec{a}^2$, $y = \vec{b}^2$, $t = (\vec{a}\vec{b}) = \sqrt{xy}\cos\xi$. If it is possible for a given point (x, y) to find two parallel vectors $\vec{a}$ and $\vec{b}$, then the orbit space extends in the t-direction up to $t = \sqrt{xy}$, which precisely defines the cone. It turns out that parallel vectors $\vec{a}$ and $\vec{b}$ exist within the triangle $0 \leq x + y \leq 3/4$ (VEV alignment is $(v_1, v_2 e^{i\alpha}, 0)$), and along the straight segments defined by $y = 0$ (VEV alignment (v_1, v_2, v_3)) and defined by $y/x = 3$ (alignment $(v_1 e^{i\pi/3}, v_2 e^{-i\pi/3}, v_3)$).

The emergent triangle symmetry of the orbit space is not related to the symmetry of the potential, but is a feature of the orbit space itself. There is simply no field transformation that realizes rotations of the cone. In this aspect, this emergent symmetry is similar to the (x, z) reflection symmetry of the orbit space in the S_4-symmetric model.

3.3.7 Minimization of the A_4-symmetric potential

The shape of the orbit space immediately leads to the list of possible phenomenologically acceptable global minima (i.e. minima not leading to additional massless scalars). These are: the apex of the cone (point A), the three vertices (points B, C and C'), and the rim of the cone ($x + y = 3/4$, $t^2 = xy$). Any other point either leads to additional Goldstone bosons or is never a global minimum.

In Appendix B.3, all these points are analyzed in some detail and the Higgs mass spectra is given. Comparing these spectra for different minimum points also shows an intriguing relation with the triangle symmetry of the orbit space.

This is the first complete solution of the minimization problem in the A_4-symmetric 3HDM.

3.4 Discussion

3.4.1 Origin of geometric CP-violation

The possibility for spontaneous CP-violation is one of the motivations behind studying multi-Higgs-doublet models. In this context it is often proposed not only that a Higgs-family symmetry should allow for spontaneous CP-violation but also that it should stabilize the VEV phases in the global minimum against variation of the free parameters. This situation is known as geometric CP violation, [117, 118] and was originally found in the $\Delta(27)$-symmetric 3HDM (though the true Higgs-family symmetry group of that model is $\Delta(54)/\mathbb{Z}_3$, see discussion in [115]). The relative VEV phases arising in geometric CP-violation are called calculable because their values follow from group theoretic arguments and do not depend on the exact values of the parameters of the potential.

Using the method described in the present Chapter, the mathematical origin of calculable phases in such models can be pinpointed. They arise due to the presence of vertices

in the orbit space Γ, see Fig. 3.1b,c,d, or to be more specific, vertices at points corresponding to non-zero relative phases. Absence of geometric CP phases would imply convexity of the orbit space, Fig. 3.1a. So, it is not the symmetry of the model *per se* that allows for calculable phases but the choice of coordinates x_i selected by the symmetry, in which the orbit space has vertices.

It is noticed that the higher the finite symmetry group, the simpler is the geometric shape of the orbit space Γ, and the more vertices linked by straight segments it possesses. This explains why it is natural that geometric CP violation starts to appear only for sufficiently large finite symmetry groups.

3.4.2 Coexistence of different minima

A priori, it might happen that, for some values of the parameters of the potential, two (or more) different types of the global minimum coexist and are degenerate. Fig. 3.1c illustrates this situation. Upon small variation of the parameters around this special point, one minimum point becomes the global minimum while the other turns into a local one, and it is clearly possible to make either of them the global minimum. This feature leads to a possibility of a first order phase transition upon smooth variation of the parameters, leading to important phenomenological consequences. It is therefore desirable to know, which models allow for such a possibility.

It can be inferred from Fig. 3.1c that this can happen if the orbit space vertices separated by a concave region, that is, if it has cusps. If instead the orbit space is a convex body, this possibility is excluded. Possibility of a first order phase transition is, therefore, linked to the non-convexity of the orbit space.

The above analysis shows that the orbit space of the S_4-symmetric 3HDM is convex. Therefore, phenomenologically relevant global minima of different type cannot coexist in this case.

In the A_4-symmetric 3HDM, this possibility arises. Namely, generic points on the rim of the cone and one of the three vertices B, C, or C' in Fig. 3.5 can be degenerate. It is also possible to make two among these three points degenerate, but not all three. Examples of such potentials can be readily constructed from geometric analysis of Fig. 3.5.

3.4.3 How general is the proposed method?

In which cases does the geometric minimization method proposed in this Chapter become useful? Strictly speaking, it has no intrinsic limitation. For example, in the context of the multi-Higgs-doublet models an absolutely general Higgs potential can be defined, a $GL(N, \mathbb{C})$ transformation can be performed in the space of doublets that brings the quadratic term to the form $M_0 r_0$ and then the procedure as discussed in Section 3.2.1 can be applied. Of course, the potential will contain very many different terms, so that the orbit space becomes a highly non-trivial multi-dimensional shape. However comprehending it is only a human limitation, and a hypothetical computer algorithm could be able to analyze this shape looking for edges, cusps and vertices.

This method becomes much more useful when the number of distinct terms becomes small. In particular, when the dimension of the neutral orbit space is three or less, the shape can be relatively easily visualized, and one can develop a much more intuitive

picture of the model than from the usual algebra. For example, in the 3HDM, this situation takes place for the following finite Higgs-family symmetry groups (based on the classification of [115]): A_4, S_4, $\Delta(54)/\mathbb{Z}_3$, and $\Sigma(36)$ (the last two cases are not discussed in this Chapter). It would be interesting to see if other useful examples appear in other models.

Part II

Fermionic extensions of the Standard Model

INTRODUCTION

In 1930, W. Pauli proposed a solution to the missing energy problem in nuclear β decays [119]. He proposed that this energy was carried by a new neutral particle with spin 1/2 in order to save energy and angular-momentum conservation. Fermi, in 1933, named the particle the neutrino and built a theory out of them to calculate the simultaneous emission of an electron with a neutrino. In 1956, the electron neutrino was discovered (indeed, due to the experimental setup it was the electron antineutrino) by Reines and Cowan through the inverse-β decay reaction ($\bar{\nu}_e + p^+ \to n^0 + e^+$) by using the neutrino flux stemming from a nuclear reactor [120]. After this discovery, and during several decades, neutrinos produced in the Sun, the atmosphere and in Supernovae were detected. During the same period, the theoretical possibility of neutrino flavor oscillations was pointed out in a milestone work by Bruno Pontecorvo [121]. After a first experimental observation of neutrino oscillations in the 60's [122], it is now well known, thanks to recent experimental results [123–128], that at least two neutrinos are massive and have non-vanishing mixing angles among the different generations. Since in the SM neutrinos are massless these experimental results can be regarded, in addition with the cosmic baryon asymmetry, as the most solid evidence that at certain energy scale new degrees of freedom should be operating.

Neutrinos being electrically neutral can be either Dirac or Majorana particles. Experimentally determining their nature requires measuring lepton number violating observables, of which neutrinoless double-β ($0\nu\beta\beta$) decay provides—certainly—the most sensitive probe. Observing a $0\nu\beta\beta$ decay signal constitutes a demonstration that lepton number is not conserved in nature and, according to the Schechter-Valle black-box theorem [15], that neutrinos are Majorana particles. The non-observation, however, does not prove otherwise. The $0\nu\beta\beta$ decay rate is highly sensitive to the neutrino mass spectrum: for an inverted mass spectrum ($m_{\nu_3} < m_{\nu_1} < m_{\nu_2}$) there is sizeable lower limit for this rate whereas for a normal mass spectrum ($m_{\nu_1} < m_{\nu_2} < m_{\nu_3}$) the leptonic CP phases can conspire leading to a vanishing rate [129]. Thus, only in the case of neutrinos having an inverted spectrum definitive conclusions can be drawn from the non-observation of $0\nu\beta\beta$.

Given the absence of a $0\nu\beta\beta$ signal the two possibilities are viable. If neutrinos are assumed to be Dirac particles, the addition of fermion EW singlets to the SM content allows the construction of new renormalizable Yukawa operators. After EWSB, neutrinos as any other SM fermion acquire mass. If instead neutrinos are assumed to be of Majorana

nature their masses are well described by the dimension-five effective operator $\mathcal{O}_5 \sim Y_{ij}\ell_i\ell_j\phi\phi$ (the so-called Weinberg operator) [130]. Although Dirac neutrinos are a suitable possibility, the working hypothesis in the second part of this thesis is that neutrinos are Majorana particles.

Any possible "incarnation" of the Weinberg operator corresponds to a model for Majorana neutrino masses, described by a beyond SM set of renormalizable interactions. Among these realizations the type-I seesaw [11–15] is certainly the most widely considered, due to its simplicity and "well-grounded" motivations [2]. Despite all its appealing features, the type-I seesaw—in its most simple version—has a serious drawback: it cannot be experimentally tested either in high-energy or in high-intensity experiments. Moreover, an attempt of reconstructing its parameter space through low-energy neutrino data fails, due to the mismatch between the low-energy observables and the number of parameters the model contain. Any approach leading to a seesaw variation leading to sizeable observables of any kind is therefore welcome

The second part of this thesis is organized as follows. Chapter 4 deals with generalities of neutrino physics. Starting with some non-exhaustive historical aspects of neutrino oscillation experiments, it gives the current values of the different neutrino oscillation parameters briefly discussing what it is at present known about absolute neutrino masses (mainly reporting the current upper limits). Some comments and upper bounds for different lepton-flavor-violating processes are given. Finally, this Chapter finishes with a general discussion about Majorana neutrino masses, starting with the Weinberg operator and emphasizing on general approaches that can be followed in the construction of testable neutrino mass models. In Chapter 5, the implications of the global $U(1)$ factor of the seesaw kinetic Lagrangian (the remaining two can be identified with global lepton number and hypercharge), assumed to be slightly broken, are discussed. The analysis focus on the consequences that this slightly broken symmetry has for lepton-flavor-violating processes, in particular for rare muon decays. This analysis is complemented by the determination of the regions of parameter space where the resulting schemes are compatible with preserving a preexisting $B - L$ in the range required to fit the indirectly measured baryon asymmetry [132–134]. This Chapter contains the novel contributions of the second part of this thesis.

2. In addition, the type-I seesaw constitutes a rather natural framework for baryogenesis via leptogenesis [25, 26, 131]. The Sakharov conditions [53] are both qualitatively and quantitatively satisfied, thus providing a common framework for the origin of neutrino masses and the cosmic baryon asymmetry.

CHAPTER 4

NEUTRINO PHYSICS

4.1 Neutrino flavor oscillations

Neutrinos are produced in weak interactions and therefore are produced as weak eigenstates, $|\nu_\alpha\rangle$ with $\alpha = e, \mu, \tau$. Since the mass eigenstates ($|\nu_i\rangle$ with $i = 1, 2, 3$) are different from the flavour eigenstates, this implies that the probability of finding a neutrino created in a given flavor to be in the same state (or in a different flavor state) oscillates with time. The weak and mass eigenstate basis are related via the lepton mixing matrix, namely

$$|\nu_\alpha\rangle = \sum_i U^*_{\alpha i} |\nu_i\rangle \,. \tag{4.1}$$

The time evolution of a given flavor eigenstate $|\nu_\alpha\rangle$, created at $t = 0$, is thus given by

$$|\nu_\alpha(t)\rangle = \sum_i U^*_{\alpha i} e^{-iE_i t} |\nu_i\rangle \,, \tag{4.2}$$

which then implies that the probability of finding the neutrino at the time t in a flavor state $|\nu_\beta\rangle$ is

$$P(\nu_\alpha \to \nu_\beta, t) = |\sum_i U^*_{\beta i} e^{-iE_i t} U_{\alpha i}|^2 \,. \tag{4.3}$$

In the two flavor case, that is to say

$$\begin{pmatrix} \nu_e \\ \nu_\mu \end{pmatrix} = U \begin{pmatrix} \nu_1 \\ \nu_2 \end{pmatrix} \,, \tag{4.4}$$

with the leptonic mixing matrix in this case given by

$$U = \begin{pmatrix} \cos\theta & \sin\theta \\ -\sin\theta & \cos\theta \end{pmatrix} \,, \tag{4.5}$$

the $\nu_e - \nu_\mu$ flavor transition probability simplifies to

$$P(\nu_e \to \nu_\mu, E) = \sin^2(2\theta) \sin^2\left(\Delta m^2 \frac{L}{4E}\right) \,. \tag{4.6}$$

Here $\Delta m^2 = m_2^2 - m_1^2$ is the mass-squared difference, θ is the mixing angle and L is the distance travelled by neutrinos from the source to the detector. From Eq. (4.6) it becomes clear that neutrino oscillation experiments allow the determination of the mass splittings and the mixing angles.

In the realistic 3-flavor case the transition probabilities involve two mass-squared differences:

$$\Delta m^2_{\rm sol} = m_2^2 - m_1^2, \quad \Delta m^2_{\rm atm} = m_3^2 - m_1^2\,, \tag{4.7}$$

and three mixing angles encoded in the leptonic mixing matrix which is conventionally parametrized in a CKM way:

$$U = \begin{pmatrix} c_{12}c_{13} & s_{12}c_{13} & s_{13}e^{-i\delta} \\ -s_{12}c_{23} - c_{12}s_{13}s_{23}e^{i\delta} & c_{12}c_{23} - s_{12}s_{13}s_{23}e^{i\delta} & c_{13}s_{23} \\ s_{12}s_{23} - c_{12}s_{13}c_{23}e^{i\delta} & -c_{12}s_{23} - s_{12}s_{13}c_{23}e^{i\delta} & c_{13}c_{23} \end{pmatrix}\,,$$

where $c_{ij} = \cos\theta_{ij}$ ($s_{ij} = \sin\theta_{ij}$) and where $\theta_{12} = \theta_{\rm sol}$, $\theta_{23} = \theta_{\rm atm}$, $\theta_{13} = \theta_{\rm reactor}$ and δ is a CP violating phase.

4.2 Neutrino flavor oscillations: experimental evidence

The experimental determination of the neutrino flavor oscillation phenomena was the result of the combination of different pieces coming from different experimental sources and setups. In the Earth neutrinos are produced either by natural or artificial sources: the Sun (solar neutrinos), the atmosphere (atmospheric neutrinos), nuclear reactors (reactors neutrinos) and accelerators (accelerator neutrinos). Although regardless of its origin, at the fundamental level, the production is to a large extent driven by EW charged and neutral current processes the properties of the produced neutrinos strongly depend upon the particular source.

In the Sun neutrinos are produced via β-decay and electron capture processes in different sub-chains of the *pp* chain, the main reaction chain in the Hydrogen-Helium thermonuclear fusion process

$$4p + 2e \rightarrow {}^4\,\mathrm{He} + 2\nu_e + \gamma\ \ , \tag{4.8}$$

which is responsible for about 99% of the solar energy. More specifically, solar neutrinos are produced in the following processes [137]:

$$pp: \quad p + p \rightarrow d + e^+ + \nu_e \tag{4.9}$$
$$pep: \quad p + e^- + p \rightarrow d + \nu_e \tag{4.10}$$
$$hep: \quad {}^3\mathrm{He} + p \rightarrow {}^4\,\mathrm{He} + e^+ + \nu_e \tag{4.11}$$
$${}^7\mathrm{Be}: \quad {}^7\mathrm{Be} + e^- \rightarrow {}^7\,\mathrm{Li} + \nu_e \tag{4.12}$$
$${}^8\mathrm{B}: \quad {}^8\mathrm{B} \rightarrow {}^8\,\mathrm{Be} + e^+ + \nu_e\ , \tag{4.13}$$

of which the ^{7}Be and *pep* reactions produce monochromatic neutrinos while the remaining yield continuous energy spectra, as can be seen in Fig. 4.1.

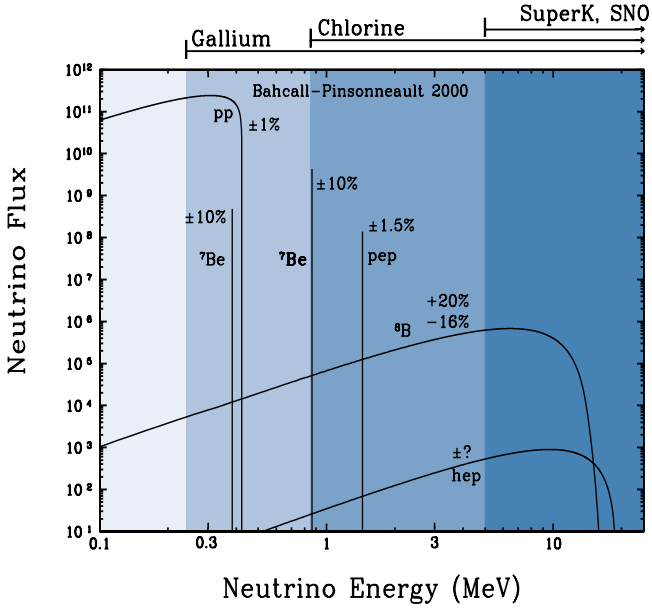

Figure 4.1: *Spectrum of solar neutrinos arising from the pp chain as predicted by the standard solar model. The different bands indicate the threshold of the different detection techniques, while the lines and curves the characteristic neutrino energy spectra, The neutrino fluxes are given in units of* cm^{-1} s^{-1} MeV^{-1} *for continuous spectra and* cm^{-1} s^{-1} *for line spectra. The numbers associated with the neutrino sources show theoretical errors of the fluxes, [135, 136].*

Atmospheric neutrinos instead are produced as by-products of hadronic showers resulting from collisions of cosmic rays with nuclei in the upper atmosphere. Production of electron and muon neutrinos is dominated by pion and subsequent muon decay:

$$\begin{aligned} \pi^{\pm} \rightarrow & \mu^{\pm} + \nu_{\mu}(\bar{\mu}) \\ & e^{\pm} + \nu_e(\bar{\nu}_e) + \bar{\nu}_{\mu}(\nu_{\mu}) + \nu_{\mu}(\bar{\nu}_{\mu}) \ . \end{aligned} \tag{4.14}$$

In contrast to solar neutrinos, which have order MeV energies (see Fig. 4.1), atmospheric neutrinos have energies in the order GeV range, as a consequence of being indirectly produced by high-energy cosmic rays events.

Reactor neutrinos stem from nuclear reactor cores as by-products of fission chains of nuclear isotopes: ^{235}U, ^{238}U, ^{239}Pu and ^{241}Pu, and their average energies are—as for solar neutrinos—of order few MeV. Finally, accelerator neutrinos are produced by proton beams interacting on a target. The pions and kaons produced in the collision are extracted and their decay by-products, except neutrinos and antineutrinos, are then stopped by absorbers. As a result, a muon neutrino beam with a rather small electron neutrino contamination (due to the kaon semileptonic decay $K^+ \rightarrow \pi^0 + e^+ + \nu_e$) is produced. As atmospheric neutrinos, accelerator neutrinos being produced by "high-energy" sources have as well order GeV average energies.

Once produced, the physical process through which they can be detected, which in turn determines the experimental setup, strongly depends on their (average) energy, E_{ν}. Three main reactions can be identified:

- Neutrino-nucleon scattering: These processes are driven by charged current reactions, and so the lepton flavor of the scattered neutrino depends on its energy. For order MeV neutrinos, as those stemming from the Sun or reactor cores, the relevant processes are

$$\bar{\nu}_e + p \to e^+ + n \ , \quad \nu_e + n \to e^- + p \ . \tag{4.15}$$

  Above the threshold for muon production ($\mathcal{O}(E_\nu) \sim$ GeV) these processes become also useful for muon and antimuon neutrino detection via

$$\bar{\nu}_\mu + p \to \mu^+ + n \ , \quad \nu_\mu + n \to \mu^- + p \ . \tag{4.16}$$

- Neutrino-electron scattering: it is a purely weak reaction which is different for ν_e and other neutrino flavors. Indeed, both charged current and neutral current processes contribute to the neutrino-electron cross section ($\sigma(\nu_e)$) whereas for the muon and tau neutrino only the neutral current process contributes. This renders the neutrino-muon and neutrino-tau scattering cross sections (($\sigma(\nu_{\mu,\tau})$)) suppressed with respect to $\sigma(\nu_e)$.
- Neutrino-nucleus scattering: These reactions turn out to be important for low energy neutrinos

$$\begin{aligned} \nu_e + A(Z,N) &\to e^- + A(Z+1,N) \ , \\ \bar{\nu}_e + A(Z,N) &\to e^+ + A(Z-1,N) \ . \end{aligned} \tag{4.17}$$

Neutrino production from all the aforementioned sources and their further detection through (mainly) the reactions in (4.15)-(4.17), have lead to a clear picture were neutrino flavor oscillations have been proved to be one of their fundamental properties. Although a large number of specific experiments have been carried out and are still undertaken—certainly—the historically conclusive experiments are (chronologically) related with atmospheric neutrinos (Super-Kamiokande (SK)) and solar neutrinos (the Sudbury Neutrino Observatory (SNO) and the Kamioka Liquid Scintillator Anti-Neutrino Detector (KamLAND))[1].

In SK (a water Cherenkov experiment), atmospheric neutrinos are detected through charged current processes interactions of neutrinos on nuclei (neutrino-nucleon scattering in (4.15)):

$$\nu_l + N \to l + N' \, , \tag{4.18}$$

the flavour l of the outgoing lepton tags the flavour of the incoming neutrino. The SK collaboration reported a deficit in the muon-like events [123] which confirmed the previous results of the water Cherenkov detectors Kamiokande [Kamiokande] and Irvine-Michigan-Brookhaven (IMB) [139] as well as the Soudan-2 iron-calorimeter experiment [140]. SK also found a zenith angle deficit in the muon-like events which is well described by neutrino oscillations. Further experimental results of the SK collaboration (1489 live-day exposure data) [138], in which the survival probability of muon neutrinos as a function of L/E [km]/[GeV] was studied, showed that the neutrino survival probability obeys a sinusoidal function as predicted by neutrino oscillations. Furthermore, this result show that other hypothesis, such as neutrino decay [141] and neutrino decoherence [142], that

1. It can be argued as well that Homestake [122], understood as a pioneer experiment, is historically the most relevant one.

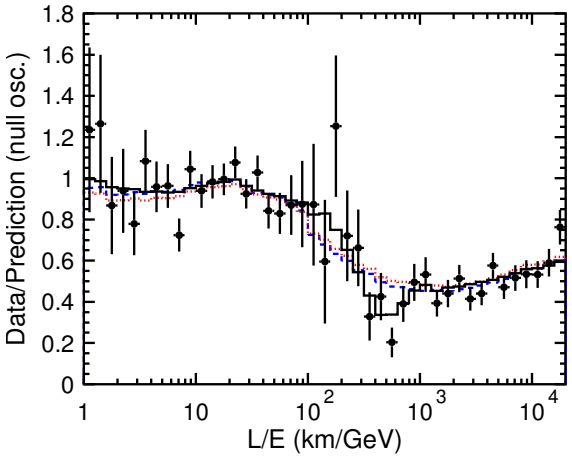

Figure 4.2: *Ratio of the data to the Monte Carlo (MC) events without neutrino oscillation (points) as a function of the reconstructed L/E together with the best-fit expectation for 2-flavor $\nu_\mu \leftrightarrow \nu_\tau$ oscillations (solid line). The error bars are statistical only. Also shown are the best-fit expectation for neutrino decay (dashed line) and neutrino decoherence (dotted line). Figure taken from [138].*

could also explain the zenith-angle dependent deficit, were disfavored (see Fig. 4.2). The SK results—indeed—were the first to establish conclusively that atmospheric neutrinos oscillate.

In contrast to SK, SNO [143] uses heavy water (D_2O), so providing deuterons as a target for charged current (CC) and neutral current (NC) interactions, as well as electrons for elastic scattering (ES) processes with solar neutrinos:

$$\text{CC}: \quad \nu_e + d \to p + p + e^- \tag{4.19}$$

$$\text{NC}: \quad \nu_\alpha + d \to n + p + \nu_\alpha \tag{4.20}$$

$$\text{ES}: \quad \nu_\alpha + e^- \to \nu_\alpha + e^-. \tag{4.21}$$

Due to background kinematical thresholds, in SNO, as in Kamiokande and in SK, the primary solar neutrino signal comes from the *pp* chain ^{8}B reaction in Eq. (4.13).

In the SNO experiment the CC reaction is exclusively sensitive to ν_e while the NC interaction is sensitive to all active neutrino flavours. The ES on electron is sensitive to all active flavours as well, but with a further reduced sensitive to ν_μ and ν_τ due the the suppressed $\sigma(\nu_{\mu,\tau})$ cross sections, as previously argued. SNO results found that the measured total ν_x flux (through the NC channel) was greater than the measured ν_e flux (through the CC channel and in ES with electrons), thus providing a conclusively demonstration that solar neutrinos are subject to flavour transformation since their production in the solar core.

Despite being conclusive, the SNO results could not shed light on the underlying mechanism responsible for solar neutrino transformation. It was not until KamLAND that the neutrino oscillation hypothesis was proved to be the correct one [144]. KamLAND is a reactor experiment which detects $\bar{\nu}_e$, produced by a network of nuclear reactors, via the inverse β decay process

$$\bar{\nu}_e + p \to e^+ + n \ , \tag{4.22}$$

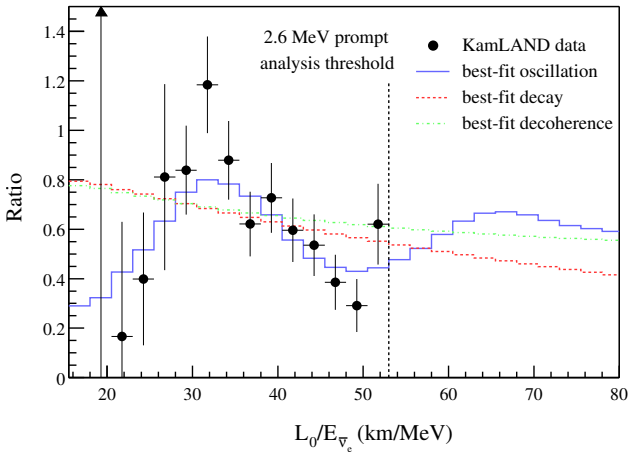

Figure 4.3: *Ratio of the observed $\bar{\nu}_e$ spectrum to the expectation for no oscillation versus L_0/E. The curves show the expectation for the best-fit oscillation, best-fit decay and best-fit decoherence models taking into account the individual time-dependent flux variations of all reactors and detector effects. The data points and models are plotted with L_0=180 km, as if all anti-neutrinos detected in KamLAND were due to a single reactor at this distance (taken from [145]).*

For that aim, a neutrino detector/target of 1 kton of ultrapure liquid scintillator placed in a 13-m-diameter spherical balloon made of 135-μm-thick transparent nylon/EVOH (ethylene vinyl alcohol copolymer) is used. KamLAND results showed a deficit of neutrinos with a distribution in L/E ([km]/[MeV]) consistent with the neutrino oscillation hypothesis with oscillation parameters in the Large Mixing Angle (LMA) region [145], thus providing a conclusive demonstration that the solar neutrino flavour conversion is due to the LMA-MSW neutrino oscillation mechanism (see Fig. 4.3).

4.3 Summary of experimental data

4.3.1 Present status of neutrino oscillation data

Precise acknowledge of the neutrino oscillation parameters arises from global fits to available neutrino oscillation data. The analysis from which the values shown in Table 4.1 and Figure 4.4 (extracted from Ref. [146]) include the following data: For atmospheric neutrinos, results from Super-Kamiokande from phase SK1-4 [147]. For long baseline accelerator experiments, K2K [148], MINOS [149], and T2K [150]. For reactor experiments, results from the finalized experiments CHOOZ [151], Paolo Verde [152], Double CHOOZ [126], Daya Bay [153], RENO [128] and KamLAND [154]. For solar neutrinos, results from radiochemical experiments: Chlorine [122] and Borexino [155, 156], Gallex/GNO [157], SAGE [158], as well as results from SK-1 [159] and SNO phases I-III [160].

It is worth mentioning that the values of the atmospheric and reactor parameters suffer from an ambiguity determined by whether the neutrino mass spectrum follows a normal or an inverted mass hierarchy, if $\Delta m^2_{\rm atm} = \Delta m^2_{31} > 0$, then neutrinos follow a normal

parameter	best fit	1σ range	2σ range	3σ range
Δm^2_{21} $[10^{-5}\text{eV}^2]$	7.62	7.43–7.81	7.27–8.01	7.12–8.20
$\lvert\Delta m^2_{31}\rvert$ $[10^{-3}\text{eV}^2]$	2.55 2.43	$2.46 - 2.61$ $2.37 - 2.50$	$2.38 - 2.68$ $2.29 - 2.58$	$2.31 - 2.74$ $2.21 - 2.64$
$\sin^2\theta_{12}$	0.320	0.303–0.336	0.29–0.35	0.27–0.37
$\sin^2\theta_{23}$	0.613 (0.427) 0.600	0.400-0.461 & 0.573–0.635 0.569–0.626	0.38–0.66 0.39–0.65	0.36–0.68 0.37–0.67
$\sin^2\theta_{13}$	0.0246 0.0250	0.0218–0.0275 0.0223–0.0276	0.019–0.030 0.020–0.030	0.017–0.033
δ	0.80π -0.03π	$0 - 2\pi$	$0 - 2\pi$	$0 - 2\pi$

Table 4.1: *Neutrino oscillation parameters summary as reported by [146]. For* Δm^2_{31}, $\sin^2\theta_{23}$, $\sin^2\theta_{13}$, *and* δ *the upper (lower) row corresponds to a normal (inverted) neutrino mass hierarchy [52].*

spectrum in which

$$m_1 < m_2 = \sqrt{m_1^2 + \Delta^2_{\text{sol}}} < m_3 = \sqrt{m_1^2 + \Delta^2_{\text{atm}}}\,. \tag{4.23}$$

Otherwise the mass spectrum is inverted ($\Delta m^2_{\text{atm}} = \Delta m^2_{32} < 0$) in which case

$$m_1 = \sqrt{m_3^2 + \Delta^2_{31}} < m_2 = \sqrt{m_1^2 + \Delta^2_{\text{sol}}} < m_3\,. \tag{4.24}$$

4.3.2 Present status of absolute neutrino masses

Neutrino oscillation experiments are only sensitive to squared-mass differences. Accessing this quantity requires other facilities and in some cases even physics beyond that directly related to neutrinos. The absolute neutrino mass scale can be determined through three possible experimental means:

- Kinematic experiments: Nuclear or particle-decay processes through ordinary β decay, e.g. through tritium decay [161–163];
- Neutrinoless double β decay experiments [164–166];
- Astrophysical and cosmological observations [167, 168].

Bounds from kinematical experiments

Direct information on the electron neutrino mass can be obtained in a precise and model-independent way through a kinematical analysis of the final region of the β decay spectra [169]. These types of experiments are based on measurements of the end-point behavior of the β-decay tritium spectrum:

$$^3\text{H} \rightarrow {}^3\text{He} + e^- + \nu_e\,, \tag{4.25}$$

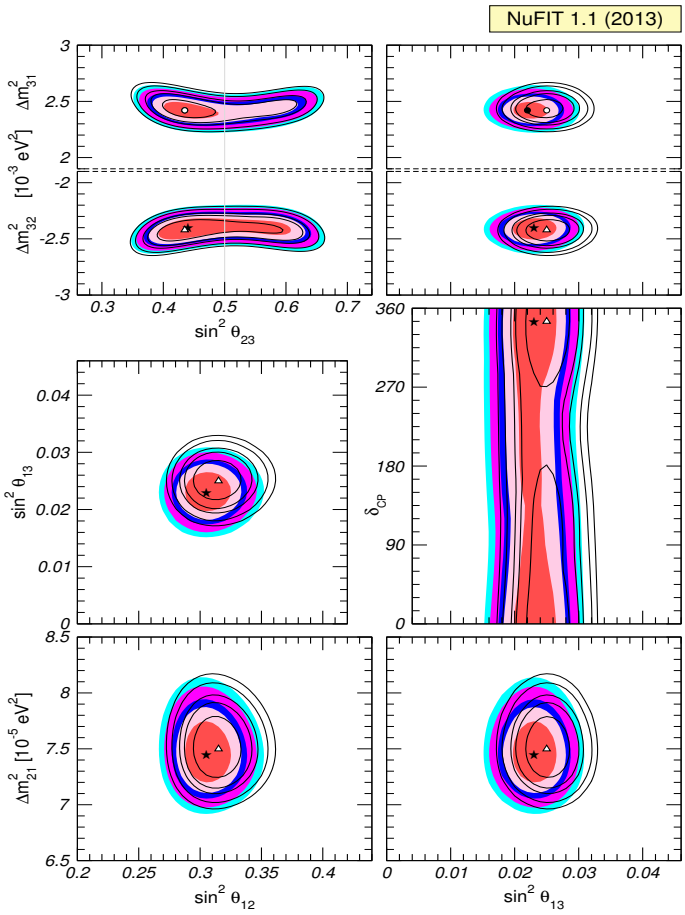

Figure 4.4: *Global 3ν oscillation analysis including all available neutrino oscillation data. The different contours correspond to the two-dimensional allowed regions at 1σ, $90\%, 95\%, 99\%$ and 3σ CL. [146].*

and the observable places bounds on

$$m(\nu_e) = \sqrt{\sum_i |U_{ei}|^2 m_i^2}\,. \tag{4.26}$$

Current limits come from Troitsk [170] and Mainz [171] experiments which have established the limits: $m_\nu < 2.05$ eV at 95% CL (Troitsk); $m_\nu < 2.2$ eV at 90% CL (Mainz). The KArlsruhe TRItium Neutrino experiment (KATRIN), using the same measurement technique, is aiming at improving present bounds or perform a measurement of the electron neutrino mass [172]. According to their proposal, unprecedented sensitivity of 0.2 eV at 90% CL is expected to be reached improving present limits by one order of magnitude, or discovery of the actual mass will be possible if it is larger than 0.35 eV.

Bounds from neutrinoless double β decay

Neutrinoless double β decay ($0\nu2\beta$) is a rare nuclear process in which two neutrons in a parent nucleus are simultaneously changed into two protons emitting two electrons but

without emitting any antineutrinos:

$$(A, Z) \rightarrow (A, Z + 2) + 2e^{-} . \tag{4.27}$$

This process, that violates lepton number by two units, is only possible if neutrinos are massive Majorana particles (see Appendix C.1). A signal would provide information on the neutrino nature and on their absolute mass scale. The signature for such a process would be a peak in the energy spectrum deposited in the detector by the 2 electrons at the endpoint energy. Constraints on the $(0\nu 2\beta)$ lifetime, which can be written as

$$(T_{\frac{1}{2}})^{-1} = G_{0\nu}|M_{0\nu}|^2 m_{ee}^2 , \tag{4.28}$$

where $G_{0\nu}$ is a phase-space factor, $M_{0\nu}$ is the nuclear decay matrix element (which depends on the kind of isotope used) imply indirectly bounds on (or a measurement of) the effective neutrino mass matrix element m_{ee}:

$$m_{ee} = \langle m_\nu \rangle = |\sum_i U_{ei}^2 m_i| . \tag{4.29}$$

Before the Enriched Xenon Observatory (Exo-200) experiment [165] released their data, the most stringent bounds on the $0\nu 2\beta$ lifetime was derived from the Heidelberg-Moscow Double Beta Decay (HMBB) experiment [166] from which the bound is,

$$m_{\beta\beta} \lesssim (0.29 - 0.35) \quad \text{eV}, \qquad 90\% \quad \text{CL} . \tag{4.30}$$

At present the tightest limit comes from EXO-200:

$$m_{\beta\beta} \lesssim (0.14 - 0.38) \quad \text{eV}, \qquad 90\% \quad \text{CL} . \tag{4.31}$$

Bounds from cosmology

Cosmology at present yields some of the strongest bounds on the overall scale for neutrino masses. The small perturbations in the early Universe, which possibly come from quantum fluctuations, evolve to the large scale structure of the present Universe. After neutrinos decouple, shortly before electron-positron annihilation, the neutrino becomes a free-streaming particle that can have effects on the growth of large scale structures and so influence the structure formation of the early Universe. So massive neutrinos with masses much larger than the present temperature are, at present time, non-relativistic and thus contribute to the cosmological matter density. The neutrino density Ω_ν is related to the number of massive neutrinos, namely

$$\Omega_\nu h^2 = \frac{\sum_i m_i}{93.2 \ \text{eV}} , \tag{4.32}$$

where h is the reduced Hubble parameter in units of 100 km/s/Mpc. Limits on $\Omega_\nu h^2$ therefore, constraint the observable $\sum_i m_i$. The Wilkinson Microwave Anisotropy Probe (WMAP) collaboration combining CMB, baryon acoustics oscillation, and supernovae type-Ia data has provided an upper bound on the neutrino masses sum assuming three neutrino species [173]:

$$\sum_i m_i \leq 0.6 \quad \text{eV}, \qquad 95\% \quad \text{CL} . \tag{4.33}$$

Reaction	Current upper bound	Collaboration
$\mu^- \to e^-\gamma$	2.4×10^{-12}	MEG [179]
$\mu^- \to e^-e^+e^-$	10^{-12}	SINDRUM [180]
$\mu^- \to 2e^-\gamma$	10^{-11}	[180]
$\tau^- \to e^-\gamma$	3.3×10^{-8}	MEG [181]
$\tau^- \to \mu^-\gamma$	4.4×10^{-8}	MEG [181]
$\tau^- \to e^-e^+e^-$	2.7×10^{-8}	[182]
$\tau^- \to \mu^-\mu^+\mu^-$	2.1×10^{-8}	[182]
$\tau^- \to e^-\mu^+\mu^-$	10^{-8}	[182]
$\tau^- \to \mu^-e^+e^-$	10^{-8}	[182]
$\mu^-\text{Au} \to e^-\text{Au}$	7×10^{-13}	SINDRUM II [183]
$\mu^-\text{Ti} \to e^-\text{Ti}$	4.3×10^{-12}	SINDRUM II [183]

Table 4.2: *Present experimental upper bounds on lepton-flavor-violating processes for pure leptonic decays. All the limits are given at 90% CL [39].*

Recently Planck measurements [174] of the CMB gave another bound which is comparable to the one reported by WMAP:

$$0.05 < \sum_i m_{\nu_i} < 0.15\text{eV}, \qquad 68\% \quad \text{CL}\,. \tag{4.34}$$

Future experiments including PLANCK lensing [175] and CMBpol lensing [176] are aiming to reach sensitivities of 0.05 eV.

4.3.3 Present status of charged lepton flavor violation

The observation of neutrino flavor oscillations constitutes an experimental proof of lepton flavor violation (LFV) in the SM neutral sector [52]. Once the SM is extended to account for neutrino masses LFV should also take place in the charged lepton sector (for a review see [177, 178]). However, until now, charged lepton flavor violating signals have not been observed despite the impressive experimental efforts. Table 4.2 shows the current experimental upper bounds on lepton flavor violating processes involving charged leptons.

Ongoing experiments and near future plans will reach sensitivities well below the value reported in Table 4.2 (for a review see [184]). Rare decays are expected to be measured in Super B factories with sensitivities reaching values two orders of magnitude smaller than present bounds. Rare μ decays, in particular, $\mu \to e\gamma$, is expected to be measured in MEG final stage with precisions exceeding 10^{-14} [185] [2], while the Mu3e experimental

2. Recently the MEG experiment released its result for $\mu \to e\gamma$ reporting the following upper limit,

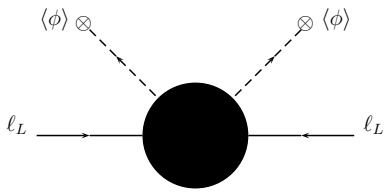

Figure 4.5: *Dimension five effective operator (Weinberg operator) responsible for Majorana neutrino masses.*

proposal at PSI aims at measuring $\mu \to 3e$ with sensitivities reaching levels of order 10^{-16} [187]. Finally, intensity upgrades at Fermilab and the proposal PRISM/PRIME at J-PARC are expected to improve the $\mu - e$ conversion branching fractions to values below 10^{-17} [188–190].

4.4 Neutrino masses: theoretical perspective

In this Section the issue of Majorana neutrino masses is discussed. The approach followed is to a certain extent novel, since it partially involves unpublished results which will make part of a future publication [191].

As has been already pointed out in the introduction, a model independent approach to the origin of neutrino masses is provided by the Weinberg operator

$$\mathcal{O}_5 = \frac{h_{\alpha\beta}}{\Lambda} \left(\ell_\alpha^T C i\tau_2 \vec{\tau} \ell_\beta\right) \left(\phi^T i\tau_2 \vec{\tau} \phi\right) \quad , \tag{4.35}$$

which diagrammatically can be represented as shown in Fig. 4.5. In principle, below the EW scale this operator suffices to account for neutrino data, the different couplings as well as the scale can be precisely fitted yielding a consistent effective phenomenological description of neutrino masses and mixings. Addressing the issue of the ultraviolet (UV) completion responsible for this operator, rather than being driven by a "simple" phenomenological requirement is given by a fundamental question, the precise origin of neutrino masses. The goal of finding the exact UV completion, implies finding the renormalizable Lagrangian which when added to the SM Lagrangian yields a complete picture.

The Weinberg operator can be understood as a "tower" of operators appearing at different orders in perturbation theory:

$$\mathcal{O}_5 = \sum_i \mathcal{O}_5^{i-\text{loop}} \quad , \tag{4.36}$$

where the order up to which the sum can be extended has to be determined by phenomenological requirements. Dimensional analysis combined with the loop suppression factors can be used in a quite generic way to deduce at which point the sum (4.36) should be truncated. In order to proceed, the four-loop diagram in Fig. 4.6 can be considered. Taking a generic trilinear scalar coupling μ for the three-point scalar vertices, as well as a generic Yukawa coupling y for the fermion-scalar-scalar couplings in the diagram, the

$\text{Br}(\mu \to e\gamma) < 5.7 \times 10^{-13}$ at the 90% CL [186].

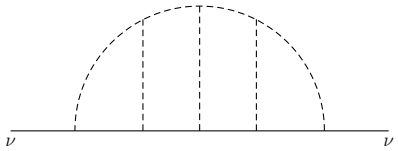

Figure 4.6: *Four-loop order realization of the Weinberg operator from which is has been argued the phenomenologically inconsistency of those realizations.*

mass matrix can be estimated to be:

$$\begin{aligned} m_\nu &\sim \left(\frac{1}{16\pi^2}\right)^4 \left(\frac{m_F}{m_S}\right)^4 y^5 \mu^3 \ , \\ &\sim 10^3 y^5 \, \text{eV} \ , \end{aligned} \tag{4.37}$$

where in the last step the fermion mass (m_F), the scalar mass (m_S) and the μ parameter have been taken to be universal and equal to 1 TeV. Taking the heavier neutrino to have a mass of 1 eV, this expression shows that consistency with neutrino data requires, in these setups, the Yukawa couplings to be order one. Unavoidably, in these schemes, the presence of the new Yukawa couplings induce lepton-flavor-violating processes, which when combined with order one Yukawa couplings and order TeV degrees of freedom render these models phenomenologically inconsistent. Although these arguments are not at all a rigorous proof, they can be used to argue that four-loop realizations of the Weinberg operator are ruled out by data. The same procedure applied to three-loop order realizations, shows that despite being still viable a certain tension appears when reconciling neutrino data with lepton-flavor-violating current limits.

From the statements given above a quite reasonable truncation turns out to be $i = 2$. Arguing a certain operator within that tower determines $\mathcal{O}_5$ requires the absence of leading realizations, which is typically accomplished by either the particle content or the presence of a certain symmetry [3]. In the literature, the usual approach for Majorana neutrino mass generation has been the consideration of particular UV completions. Such approach, although interesting by itself, is limited to the predictions (phenomenological consequences) of the corresponding realization. A much more interesting option would be that in which the analysis is not limited to a specific realization and instead at a certain level (tree level, one-loop level or two-loop level) all the possible realizations are determined. Indeed, at the tree level this "program" was already carried out, finding that there are three and only three tree level UV completions of the Weinberg operator [192]: type-I seesaw [11–15], type-II seesaw [14, 57–59] and type-III seesaw [193], for which the corresponding diagrammatic representation of the neutrino mass matrix are shown in Fig. 4.7

In the type-I seesaw model as well as in the type-III seesaw model the Majorana neutrino mass matrix arises due to the interchange of new fermions (generally three), EW singlets (RH neutrinos, N_R) in the former case while EW triplets (T) in the latter case. A thorough discussion of the type-I seesaw Lagrangian, used in Chapter 5, is presented in Appendix C.2. The type-II, in contrast, relies on a UV completion where the new degree of

3. An example corresponds to the radiative seesaw[Ma-RAD-SS], where due to the presence of an exactly conserved $\mathbb{Z}_2$ symmetry the type-I seesaw neutrino mass matrix is forbidden. The mass matrix is then generated via a one-loop realization of the Weinberg operator (see the discussion below).

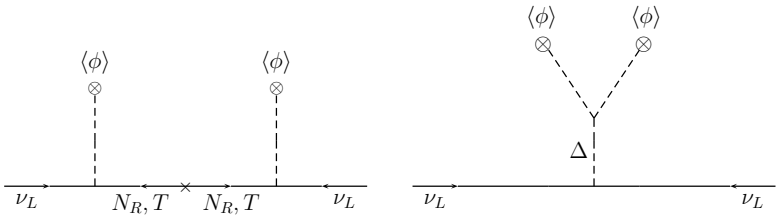

Figure 4.7: *Tree level realizations of the Weinberg operator which define the type-I, type-II and type-III seesaw models.*

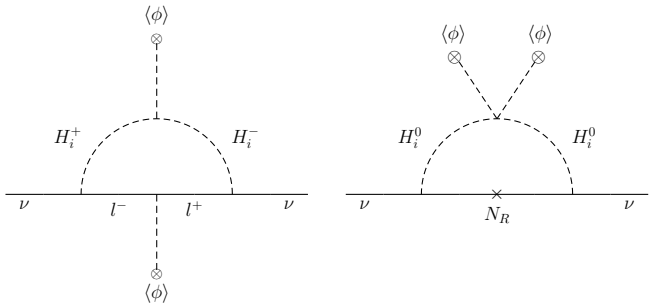

Figure 4.8: *Feynman diagrams accounting for the Zee model (left plot) and the radiative seesaw (right plot).*

freedom (one is sufficient to fit neutrino data) is a scalar EW triplet (Δ). These scenarios lead to quite a few interesting possibilities. For instance, the type-I seesaw provides a natural playground for baryogenesis via leptogenesis (see next Section) whereas the type-II and type-III seesaws, involving states with non-trivial EW quantum numbers, open the possibility of "testing" the origin of neutrino masses at the collider level, provided they have order TeV masses.

At the one-loop level the "program" was initially undertaken in Ref. [192], by considering only irreducible topologies. And was recently completed by considering as well reducible topologies [194]. In contrast to Ref. [192], where the analysis was carried out by hand, in Ref. [194] a novel strategy for tackling the problem was developed. It is based on a "certain" algorithm which is somehow inherited from `FeynArts` [195], which is indeed the tool used by the authors to exhaustively cover all possibilities. When determining all possible realizations of $\mathcal{O}_5$ at the one-loop level the following "recipe" proves to be useful:

A. Determine with the aid of `FeynArts` all possible topologies associated with $\mathcal{O}_5$.

B. Once all possible relevant topologies are determined, proceed with fermion and scalar propagator insertions.

C. By using the SM gauge quantum numbers of the external lines determine the gauge quantum numbers of the fields flowing in the loop.

D. Calculate one-loop integrals.

In that way the analyses in Ref. [192,196] covers all the possibilities which—of course—include well known one-loop realizations: the Zee model [60] and the radiative seesaw [90]. The UV completions in these two cases are such that a tree level neutrino mass cannot be constructed: (*i*) in the Zee model case, the beyond SM field content involves an extra scalar EW doublet and a single-charged scalar EW singlet, which render the construction

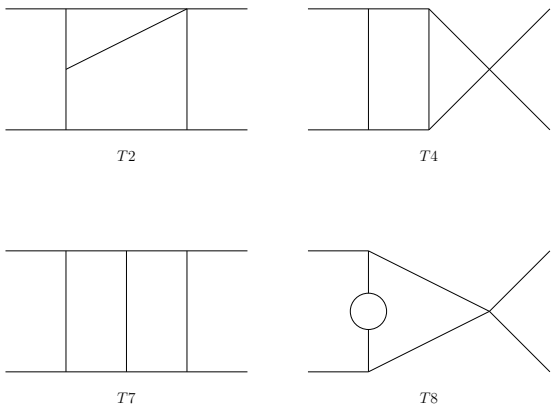

Figure 4.9: *Some examples of two-loop topologies associated with two-loop realizations of the Weinberg operator.*

of a tree level mass matrix impossible; (*ii*) in the radiative seesaw the new particle content involves in addition to the RH neutrinos a second scalar EW doublet, however by enforcing the SM (beyond SM) fields to be even (odd) under $\mathbb{Z}_2$ the standard type-I seesaw tree level neutrino mass matrix is forbidden, leading to a one-loop setup (see Fig. 4.8).

Providing a full picture for Majorana neutrino masses implies carrying out the same "program" for the two-loop case. This task is obviously much more demanding and involves much more topologies and possible diagrams, which from naive considerations might lead to the conclusion that the number of possibilities is so large that a comprehensive study will end up being useless. This however is not the case, as it is now discussed. The "recipe" sketched in items A-D is readily extended to the two-loop analysis case. Accordingly, with the aid of `FeynArts` and following those steps, a reduced number of topologies is found. Focusing on irreducible topologies, 29 inequivalent topologies are found. By renormalizability and the criteria of dealing with "genuine" two-loop realizations (meaning two-loop diagrams for which a leading tree or one-loop level contribution does not exist), this number is reduced to 11 topologies. Some examples are shown in Fig. 4.9, where the notation used is TX ($X = 1, \ldots, 11$). With the full list of topologies, item A in the recipe is over. When moving ahead to item B, it has been found that the number of Feynman diagrams for each topology is still under control, being in the "worse" case 17. To complete the classification, items C and D should be addressed. This is something in which there is still some work to be done.

As expected, among the topologies found well known two-loop models have been found. For example, with the appropriate field insertion and gauge quantum numbers topology $T7$ in Fig. 4.9 corresponds to the Cheng-Li-Babu-Zee model [61, 197, 198]. This two-loop UV completion of the Weinberg operator includes one singled-charged and one doubled-charged scalar EW singlets. It turns out that with this particle content there is no way of constructing either a tree level or one-loop level neutrino mass matrix. Thus, implying this model correspond to a "genuine" two-loop realization of the Weinberg operator where the particle content constraints neutrino masses to be generated at the two-loop order as shown in Fig. 4.10.

This analysis corresponds to the most simple approach. A much more intrincated possibility, but anyway viable, will be that in which a certain unknown mechanism e.g.

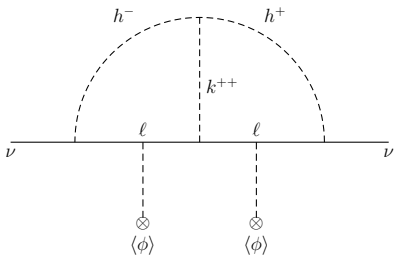

Figure 4.10: *Feynman diagram accounting for light neutrino masses in the Cheng-Li-Babu-Zee model*

a certain symmetry fordids the Weinberg operator. In that case, the next lepton number violating effective operator (the dimension seven) will account for neutrino masses. These approaches are to a large extent not very natural, since *a priori* there is no reason for this to be the case. However, those constructions have certain interest, in particular because due to the intrinsic suppression of the operator (Λ^{-3}) the UV completions are naturally light (order TeV) and the involved couplings large. Scenarios of this kind almost unavoidably lead to a rich high-energy as well as high-intensity phenomenology e.g. in these schemes a rich lepton-flavor-violating phenomenology is always expected.

4.5 The baryon asymmetry of the Universe

There is robust observational evidence that the Universe is made of matter, and not antimatter. The Earth, the Sun and the Moon are made of matter. In cosmics rays, the antiproton-proton ratio is about 10^{-4} [199, 200] and the antiprotons are supposed to be secondaries produced by cosmic-ray collisions with the interstellar medium. Therefore, there is no indication of antimatter in the galaxy. At larger scales, no strong γ-ray emission from nucleon-antinucleon annihilations from galaxies colliding with antimatter galaxies in the same cluster, have been observed [201]. Since matter is made of electrons orbiting neutrons and protons (both a type of baryon), this is a clear indication that there is a baryon asymmetry in the Universe. Precise measurements of the acoustic peaks of the CMB as well as of the relative abundance of light-elements (^{4}He, ^{3}He, D and Li) have allowed an indirect experimental determination of the baryon asymmetry (see e.g. [39] for a review) [132–134]:

$$Y_{\Delta B} = \frac{n_B - n_{\bar{B}}}{s} = (8.75 \pm 0.23) \times 10^{-11} \ , \tag{4.38}$$

where n_B, $n_{\bar{B}}$ and s are, respectively, the number densities of baryon, antibaryons and the entropy density (see next Section and Appendix C.3).

The conventional wisdom is that the baryon asymmetry is generated by a dynamical mechanism (baryogenesis), for which the fundamental rules, the so-called Sakharov rules, are well known [53]. In short, a baryonic asymmetric Universe is possible provided the following conditions are satisfied:

A. Baryon number (B) violating interactions exist.

B. Those interactions violate the C and CP symmetries.

C. During the evolution of the primordial Universe, an stage where these interactions are out-of-equilibrium exist.

Any particle physics model in which these conditions are satisfied provides a framework where the cosmic asymmetry puzzle can be addressed. Given the precise value of $Y_{\Delta B}$, it turns out that certain scenarios, although satisfying the conditions at the qualitative level fail quantitatively. The most remarkable example is certainly the SM, where baryon number is violated at the non-perturbative level via EW sphaleron reactions, CP violation is provided by the CKM CP violating phase and departure from thermodynamical equilibrium is given by the EW phase transition. However, despite containing all the ingredients required by the Sakharov conditions, at the quantitative level in the SM framework a baryon asymmetry with a value given by (4.38) cannot be generated. This fact is indeed a clear and strong evidence in favor of beyond SM physics.

Scenarios for baryogenesis are plenty, and cover quite a large number of particle physics models. Despite the large number, they can be classified into two categories, depending on how the departure from thermal equilibrium is achieved: baryogenesis models where departure from thermal equilibrium is attained via a phase transition (associated with the breaking of a gauge or global symmetry) and baryogenesis models where departure from thermal equilibrium is provided by the expansion of the Universe.

A viable possibility within baryogenesis scenarios, is that in which the B (or $B-L$, depending on the model) asymmetry is generated at a very high-energy scale. Regardless of the high-energy scenario, what is known is that the dynamics of the heavy degrees of freedom at some stage will cease to produce an asymmetry i.e. the asymmetry will be frozen. If the asymmetry matches the observed one, and below the freeze-out temperature ($T_{\rm Fo}$) there are no extra degrees of freedom that can wipe out what was generated, an explanation (physics model) for (4.38) is given. However, even if the produced $Y_{\Delta B}$ falls in the indirectly measured range, if new degrees of freedom below $T_{\rm Fo}$ are present this is not necessarily the case. Indeed, such an observation can provide an useful tool to constraint the parameter space of TeV scale particle physics models (as it is done in Chapter 5). For that aim an analysis relying on the Boltzmann EQuation (BEQ) is needed.

4.5.1 Boltzmann equations

With the aim of putting into context the discussion of the last section of Chapter 5, in this section a rather general discussion of the BEQ is presented. This section does not aim to provide an exhaustive review of technical and/or physical aspects of the BEQ, instead only few qualitative aspects are discussed.

The Boltzmann equation (BEQ) determines the evolution of a particle phase space distribution function, $f(p^\mu, x^\mu)$. In its more general form it can be written according to

$$\hat{\mathbf{L}}[f] = \mathbf{C}[f] \ , \tag{4.39}$$

where $\hat{\mathbf{L}}$ is the Liouville operator and $\mathbf{C}$ is the collision operator. From its covariant relativistic generalization and using the Robertson-Walker metric, the Liouville operator has a rather simple form:

$$\hat{\mathbf{L}}[f] = E\frac{\partial f}{\partial t} - \frac{\dot{R}}{R}|\vec{p}|^2\frac{\partial f}{\partial E} \ . \tag{4.40}$$

In terms of the number density

$$n(t) = \frac{g}{(2\pi)^3} \int d^3|\vec{p}|\, f(E,t) \ , \tag{4.41}$$

where g is the number of degrees of freedom of the corresponding species, the BEQ can be recasted as

$$\frac{d}{dt} n_X + 3\frac{\dot{R}}{R} n_X = \frac{g}{(2\pi)^3} \int \frac{d^3|\vec{p}|}{E}\, \mathbf{C}[f] \ . \tag{4.42}$$

The second term in the left-hand side accounts for the expansion of the Universe, for it can be expressed in terms of the Hubble expansion $H = \dot{R}(t)/R(t)$ (with $R(t)$ the scale factor). The collision term in the right-hand side has a rather involved form, and nevertheless for the following discussion its explicit structure is not relevant. Given a specific set of interactions, the number density of a species X can then be calculated by integration of (4.42). There are, however, a couple of convenient change of variables:

- ⋆ The Universe expansion effects can be scaled out by replacing the number density by the number density-to-entropy ratio ($Y_X = n_X/s$), as can be readily seen by using the conservation of entropy per comoving volume ($s\,R =$ constant):

$$\begin{aligned} s\, Y_X &= \dot{n} + 3\frac{\dot{R}}{R} n \\ &= \dot{n} + 3Hn \end{aligned} \tag{4.43}$$

- ⋆ Since the collision term usually depend explicitly upon T rather than time, introducing the dimensionless temperature parameter

$$z = \frac{M_X}{T} \ , \tag{4.44}$$

turns out to be convenient. In that case the time derivative can be replaced by derivative in z through

$$\frac{dz}{dt} = -\frac{M_X}{T^2}\dot{T} \quad \Rightarrow \quad \frac{dz}{dt} = zH(z) \ . \tag{4.45}$$

With those changes the BEQ can then be rewritten according to

$$\frac{d}{dz} Y_X = \frac{1}{s\, H\, z} \left[\frac{g}{(2\pi)^3} \int d|\vec{p}|^3\, \mathbf{C}[f] \right] \ . \tag{4.46}$$

Studying the evolution of the number density-to-entropy ratio for a given species is therefore entirely determined by particle physics processes, encoded in the collision term.

If there are no further Q violating reactions, asymmetries $Y_{\Delta Q}$ generated via X and $\bar{X}$ decays can be produced in the thermal bath if the decay by-products carry a Q charge, its reactions violate C and CP and departure from thermal equilibrium. In that simplified scenario, the BEQ accounting for the evolution of $Y_{\Delta Q}$ can be sketched without loss of generality as follows:

$$\frac{d}{dz} Y_{\Delta Q} = S + W \ , \tag{4.47}$$

where the factor $(s\,H\,z)^{-1}$ has been absorbed in the source, S, and washout, W, terms. The source term contains those reactions that "feed" the asymmetry while the washout those that tend to wipe it out, and their explicit form depend is model dependent.

In the case in which in addition to X, there is another species Y with Q breaking interactions as well the situation is different. Depending on the mass differences between the two species, M_X and M_Y, three cases can be identified:

- ⋆ Comparable M_X, M_Y masses ($M_X \sim M_Y$): in that case the Q asymmetry will be determined by both X and Y dynamics: $Y_{\Delta Q} = Y^X_{\Delta Q} + Y^Y_{\Delta Q}$. The evolution of $Y_{\Delta Q}$ is then dictated by a system of coupled BEQs, which schematically can be written as:

$$\frac{d}{dz}Y^X_{\Delta Q} = S_X + W_X \quad \text{and} \quad \frac{d}{dz}Y^Y_{\Delta Q} = S_Y + W_Y \ . \tag{4.48}$$

- ⋆ Either $M_X \gg M_Y$ (or $M_Y \gg M_X$): the generation of the Q asymmetry will undergo two stages. First, production via X dynamics at $T \sim M_X$. The asymmetry produced in that stage ($Y^X_{\Delta Q}$), after freeze-out will remain frozen until Y dynamics becomes effective. At that stage, Y-related processes will tend to wipe out $Y^X_{\Delta Q}$, and the final $Y_{\Delta Q}$ asymmetry will be basically entirely determined by Y dynamics. A particular interesting case (Chapter 5) is that in which S_Y is either vanishing or negligible. In that case, if any Q asymmetry is to be present at low temperatures ($T \ll M_Y$) will be solely to $Y^X_{\Delta Q}$ circumventing the Y-related washout effects, which are determined by

$$\frac{d}{dz}Y_{\Delta Q} = W_Y \ . \tag{4.49}$$

In models with TeV RH neutrinos (TEV scale seesaw models), as those considered in Chapter 5, Q turns out to be lepton number L (more precisely $B - L$). Production of the $B - L$ asymmetry can proceed via their dynamics, provided resonant enhancements of the source term are present [4]. Barring that possibility a lepton asymmetry cannot be generated through RH neutrino dynamics. However, that dynamics can affect (and even completely wipe out) a preexsiting asymmetry generated at higher temperatures by heavier different degrees of freedom. In that case, the RH neutrino induced washouts are quantified by an equation having the form (4.49). Explicitly, the following equation [203]:

$$\frac{d}{dz}Y_{\Delta_\alpha} = -\frac{\kappa_\alpha}{4}\sum_{\beta=e,\mu,\tau} C^{(\ell)}_{\alpha\beta}Y_{\Delta_\beta}K_1(z)z^3 \tag{4.50}$$

where the κ_α parameter determines the strength of washouts in each lepton flavor and its value is in turn determined by Yukawa couplings, the matrix $\boldsymbol{C^{(\ell)}}$ (so-called flavor coupling matrix) is determined by those reactions which are in thermal equilibrium when the RH neutrino dynamics become effective, $K_1(z)$ is a Bessel function (see Appendix C.3) and $\Delta_\alpha = L_\alpha + B/3$ with $L_\alpha = e_\alpha + 2\ell_\alpha$. The precise definitions of the the different quantities are given in Chapter 5, Appendix C.3 and more precisely [25].

4. Technically speaking, whenever the CP violating asymmetry, more precisely the wave-function correction, is resonantly enhanced (see e.g. [202]).

Summary

In this Chapter several aspects of neutrino physics have been treated. Aiming to give a motivation for Chapter 5 a historical discussion of neutrino oscillation experiments has been presented as well as the current status of neutrino oscillation data has been provided. Some comments on absolute neutrino mass measurements have been done, paying special attention to their current experimental upper limits. The theoretical approach to Majorana neutrino masses, based on the Weinberg operator have been discussed, focusing on certain specific realizations. Finally rather general statements about the BEQ have been elaborated, in order to fix the notation and technical aspects needed at the end of Chapter 5.

CHAPTER 5

MLFV REALIZATIONS OF MINIMAL SEESAW

5.1 Introduction

Neutrino flavor oscillations provide an unquestionable experimental proof of LFV. While it is a fact in the neutral sector, until now LFV in the charged sector has escaped all experimental scrutinies, thus implying only upper limits on the different lepton-flavor-violating rates exist. The size of lepton-flavor-violating effects is tightly related with the mechanism responsible for neutrino masses, so from that point of view predictions for LFV physics are entirely model dependent. Models for Majorana neutrinos masses yielding sizable lepton-flavor-violating effects have a common feature: tiny neutrino masses do not require neither tiny couplings nor decoupled degrees of freedom.

The type-I seesaw, already introduced in Chapter 4, is a clear example where the smallness of neutrino masses is due to either heavy degrees of freedom or tiny Yukawa couplings, and accordingly SM charged lepton-flavor-violating rates within this framework have values far below any foreseen experiment. Scenarios where neutrino data can be fitted and at the same time LFV becomes observable can be grouped in three categories: (i) models where neutrino masses arise through a specific radiative realization of the Weinberg operator (see Chapter 4); (ii) models stemming not from the Weinberg operator but instead by the next lepton number violating effective operator ($D = 7$); (iii) models with slightly broken lepton number.

Besides the $SU(3)^3$ global flavor symmetry, the type-I seesaw kinetic terms are also $U(1)^3$ invariant. Two of these $U(1)$ global factors are readily identifiable with hypercharge and lepton number, the remaining $U(1)$ is an additional global symmetry for which a "clear" identification is not possible, but that anyway it is explicitly broken at the Yukawa coupling level, and so probably for that reason has not received too much attention.

In this chapter, the role played by this additional factor (from now on denoted $U(1)_R$) is explored under the following assumptions: (a) The different SM lepton fields as well as the RH neutrinos have non-trivial R charges; (b) $U(1)_R$ is slightly broken. The analysis is carried out in a minimal RH neutrino seesaw model (2 RH neutrinos), focusing on the possible implications this slightly broken symmetry can have on lepton-flavor-violating effects. Interestingly, among the families of possible models that can be envisaged (via

R charge assignments), there is a category which realizes the Minimal Lepton-Flavor-Violating (MLFV) hypothesis in the sense that all the couplings are entirely determined by low-energy neutrino data. Moreover, is for that category that with TeV RH neutrino masses lepton-flavor-violating effects turn out to be sizable, in particular rare muon decays: $\mu^{\pm} \to e^{\pm}\gamma$, $\mu^{\pm} \to e^{\pm}e^{\mp}e^{\pm}$ and $\mu - e$ conversion in nuclei. So, from that point of view it can be fairly said that these models are within a new class of models where LFV is not due to any of the mechanisms defined in items $(i) - (iii)$.

This Chapter is organized as follows: in Section 5.2 the scenarios arising from the different R-charge assignments are discussed in detail. In Section 5.3 the phenomenology of charged-lepton-flavor-violating decays in the emerging models is discussed. In Section 5.4, as a complementary analysis, the implications of such constructions for scenarios of high scale baryogenesis are studied. Instead of assuming that the baryon asymmetry is produced by the out-of-equilibrium and CP-violating decays of the TeV RH states (via resonant leptogenesis), the constraints on the Yukawa couplings imposed by the requirement of not erasing an existing asymmetry (produced at much higher scales by an arbitrary mechanism) are derived.

5.2 The setups

Though several realizations of the MLFV hypothesis exist in the literature [204–207] all of them are based on the same approach: first, the full flavor group G is determined by the global flavor invariance of all the SM gauge and kinetic terms. G can be decomposed into a product of global $U(1)$ phase rotations and a non-Abelian subgroup G_F. Next, the charged lepton and neutrino Yukawa couplings are promoted to dimensionless auxiliary fields (spurions) with definitive flavor group transformation properties that leave the corresponding Yukawa terms in the Lagrangian invariant under G_F. It is then required that the entire Lagrangian also respects G_F. This includes any higher-dimensional effective operator contributions, which should thus be constructed from appropriate spurion insertions [1]. With the operators at hand and—if needed—under certain restrictions on G_F the lepton-flavor-violating effects can be estimated by means of low-energy neutrino data (see Table 4.1 and ref. [204, 207]).

The kinetic and gauge interaction Lagrangian of the SM extended with two RH neutrinos exhibits a global $G = U(3)_e \times U(3)_\ell \times U(2)_N$ symmetry. Factorizing three $U(1)$ factors from G, the global symmetry can be rewritten as $U(1)_Y \times U(1)_L \times U(1)_R \times G_F$ where $U(1)_{Y,L}$ can be identified with global hypercharge and lepton number whereas the $U(1)_R$ is a new global symmetry [207, 208]. The remaining direct product group $G_F = SU(3)_e \times SU(3)_\ell \times SU(2)_N$ determines the flavor symmetry which is explicitly broken in the Yukawa sector.

As explained above, the usual procedure is based on an effective-theory approach. Here, instead, the seesaw Lagrangian is explicitly considered with a slightly broken $U(1)_R$ and the possible realizations according to the R-charge assignments are classified. Under these considerations, in the models featuring sizable lepton-flavor-violating effects, the flavor structure is determined by low-energy observables as well (up to a global normalization factor), not as a consequence of a restricted MLFV hypothesis but by the intrinsic

1. An exception are the explicit MLFV models discussed in Ref. [206].

structure of the resulting models, thus realizing in that way the MLFV hypothesis.

Models for which the R charges allow for large Yukawa couplings and TeV RH neutrino masses should lead to sizable charged-lepton-flavor-violating processes. Consistent models of $\mathcal{O}$(TeV) RH states and large Yukawa couplings are achievable if cancellations among different pieces of the light neutrino mass matrix are allowed, and the RH neutrino mass spectrum is not strongly hierarchical [209] [2]. The TeV-scale seesaw models arising from the presence of the $U(1)_R$ symmetry are expected to be in that sense different: no cancellations are needed because the suppression in the effective light neutrino mass matrix is no longer constrained to be related with the heaviness of the RH neutrinos. Indeed, depending on the R-charge assignments two classes of generic models can be identified: models in which the mechanism that suppresses the light neutrino masses propagates to lepton-flavor-violating observables, thus rendering their values far below planned experimental sensitivities; and models in which the mechanism decouples in such a way that lepton-flavor-violating effects become sizable. This is in contrast to models where $U(1)_L$ is slightly broken so that lepton number and LFV occur at the same scale.

Depending on the R-charge assignments two classes of generic models can be identified. This is discussed in more detail just below. Requiring $U(1)_R$ invariance of the charged lepton Yukawa terms determines $R(e)$ in terms of $R(\ell)$ and $R(\phi)$. After fixing $R(\phi) = 0$, to avoid charging the quark sector, the remaining charges can be fixed by starting with $R(N_{1,2})$. In order to have sizable lepton-flavor-violating effects both the $N_{1,2}$ Majorana mass terms should be suppressed by R-breaking parameters (generically denoted by ϵ), so $R(N_{1,2}) \neq 0$. Thus one has only three possibilities: (A) $R(N_1) = R(N_2)$, (B) $R(N_1) = -R(N_2)$ and (C) $|R(N_1)| \neq |R(N_2)|$. The phenomenology of case (C), however, is expected to be similar to the one arising from models with R-charge assignments of type (A). The reason is that in that case the $N_1 - N_2$ mixing is always $U(1)_R$ suppressed, which in turn implies suppressed charged lepton-flavor-violating processes (equivalently, the effective neutrino mass matrix will not be ϵ suppressed, forcing tiny Yukawas or heavy $N_{1,2}$ states). This is to be compared with models based on R-charge assignments of type (B), where the $N_1 - N_2$ turns out to be maximal and a set of unsuppressed $\ell - N$ Yukawa couplings can always be obtained by properly choosing $R(\ell)$ (in these models the effective neutrino mass matrix involves extra ϵ suppression factors).

In summary depending on the R-charge assignments two classes of generic models can be identified: models in which the mechanism that suppresses the light neutrino masses propagates to lepton-flavor-violating observables, thus rendering their values far below planned experimental sensitivities; and models in which the mechanism decouples in such a way that lepton-flavor-violating effects become sizable. In what follows, in order to illustrate this is actually the case, two examples of models of type A and B are discussed.

Type-A models [207]: $R(N_{R_a}) = +1$ and $R(\ell_{L_\alpha}) = R(e_{R_\alpha}) = R(\phi) = 0$

In this case, in the basis in which the charged lepton Yukawa couplings and the Majorana RH neutrino mass matrix are diagonal, the Lagrangian in Eq. (C.12) reads

$$\mathcal{L} = -\bar{\ell}\hat{\boldsymbol{Y}}_{\boldsymbol{e}}\, e\phi - \epsilon\, \bar{\ell}\boldsymbol{\lambda}^*\, N\tilde{\phi} - \frac{1}{2}\epsilon^2\, \mu N^T\, C\, \hat{\boldsymbol{Y}}_{\boldsymbol{N}}\, N + \text{H.c.}\,. \tag{5.1}$$

2. In the case of a large hierarchy among the different RH neutrino masses the one-loop finite corrections to the light neutrino mass matrix can exceed the corresponding tree-level contributions. Neglecting such corrections can in this case lead to a model inconsistent with neutrino data [210].

where $\hat{\boldsymbol{Y}}_{\boldsymbol{e}}$, $\boldsymbol{\lambda}^*$ and $\hat{\boldsymbol{Y}}_{\boldsymbol{N}} = \text{diag}(Y_{N_1}, Y_{N_2})$ are the Yukawa coupling matrices. The dimensionless parameter $\epsilon \ll 1$ slightly breaks $U(1)_R$ whereas, due to the assignment $L(N) = 1$, the lepton number $U(1)_L$ factor is broken by μ. With this setup the 5×5 neutral fermion mass matrix in Eq. (C.18) can be written as

$$\boldsymbol{\mathcal{M}_N} = \begin{pmatrix} \boldsymbol{0} & \epsilon\, v\boldsymbol{\lambda} \\ \epsilon\, v\boldsymbol{\lambda}^T & \epsilon^2\, \mu \hat{\boldsymbol{Y}}_{\boldsymbol{N}} \end{pmatrix} , \tag{5.2}$$

where for convenience the VEV has been rescaled according to $v \to v/\sqrt{2}$, with v given by Eq. (1.6). Using the notation introduced in Appendix C, in the seesaw limit, which in this case reads $v\boldsymbol{\lambda} \ll \epsilon\mu\hat{\boldsymbol{Y}}_{\boldsymbol{N}}$ the effective light-neutrino mass matrix in Eq. (C.26), is given by

$$\boldsymbol{m}_{\boldsymbol{\nu}}^{\textbf{eff}} = -\frac{v^2}{\mu} \sum_{a=1,2} \frac{\boldsymbol{\lambda_a} \otimes \boldsymbol{\lambda_a}}{Y_{N_a}} , \tag{5.3}$$

with $\boldsymbol{\lambda_a} = (\lambda_{ea}, \lambda_{\mu a}, \lambda_{\tau a})$. The corresponding light neutrino masses are obtained from the leptonic mixing matrix (Eq. (4.8)):

$$\boldsymbol{U}^T\, \boldsymbol{m}_{\boldsymbol{\nu}}^{\textbf{eff}}\, \boldsymbol{U} = \hat{\boldsymbol{m}}_{\boldsymbol{\nu}}^{\textbf{eff}} . \tag{5.4}$$

In the 2 RH neutrino mass model the constrained parameter space enforces one of the light neutrinos to be massless. Thus, in the normal hierarchical (see Eq. (4.23)) mass spectrum case $m_{\nu_1} = 0$ and $m_{\nu_2} < m_{\nu_3}$ whereas in the inverted case (see Eq. (4.24)) $m_{\nu_3} = 0$ and $m_{\nu_1} < m_{\nu_2}$.

Since the dimension five effective operator (see Eq. (4.35)) is $U(1)_R$-invariant, the neutrino mass matrix does not depend on ϵ; the suppression ensuring light neutrino masses is solely provided by the lepton number breaking parameter μ. On the other hand, the RH neutrino mass spectrum is determined by

$$\hat{\boldsymbol{\mathcal{M}}}_{\boldsymbol{N}} = \epsilon^2\, \mu\, \hat{\boldsymbol{Y}}_{\boldsymbol{N}} . \tag{5.5}$$

From this expression it can be seen that as long as the $U(1)_R$ global symmetry is an approximate symmetry of the Lagrangian ($\epsilon \ll 1$) the RH neutrino mass scale is decoupled from the lepton-number-violating scale. Thus, the RH neutrino masses do not lie at the same scale as that at which lepton-number breaking takes place.

Assuming $\hat{\boldsymbol{Y}}_{\boldsymbol{N}}, \boldsymbol{\lambda} \lesssim \mathcal{O}(1)$ an estimation of the lepton number breaking parameter μ can be made, $\mu \sim 10^{15}$ GeV using $\sqrt{\Delta m^2_{31}} \sim 0.05$ eV as an estimate of the largest light neutrino mass [39]. From this estimation and Eq. (5.5) it can be seen that values of ϵ of the order of $\sim 10^{-6}$ allow to lower the lightest RH neutrino mass below 1 TeV.

Formal invariance of the Lagrangian under G_F is guaranteed if the Yukawa matrices, promoted to spurion fields, transform according to

$$\boldsymbol{Y_e} \sim (\bar{\boldsymbol{3}}_e, \boldsymbol{3}_\ell, \boldsymbol{1}_N) , \quad \boldsymbol{\lambda}^* \sim (\boldsymbol{1}_e, \boldsymbol{3}_\ell, \bar{\boldsymbol{2}}_N) , \quad \boldsymbol{Y_N} \sim (\boldsymbol{1}_e, \boldsymbol{1}_\ell, \bar{\boldsymbol{3}}_N) . \tag{5.6}$$

The constraints imposed by G_F imply

$$\boldsymbol{\lambda} = \boldsymbol{\lambda_\ell} \otimes \boldsymbol{\lambda_N} , \tag{5.7}$$

where $\boldsymbol{\lambda_\ell}$ is a $SU(3)_\ell$ triplet and $\boldsymbol{\lambda_N}$ a $SU(2)_N$ doublet in flavor space. Accordingly, in this kind of models an unequivocal determination of the flavor structure via the MLFV hypothesis is possible by means of a restrictive flavor symmetry $G'_F \subset G_F$. Though several possibilities may be envisaged we do not discuss further details since, as shown below, in this type of models, contributions to lepton-flavor-violating processes of charged leptons are always negligible.

Type-B models: $R(N_{R_1}) = R(\ell_{L_\alpha}) = R(e_{R_\alpha}) = +1$, $R(N_{R_2}) = -1$, $R(\phi) = 0$. Changing R charges to L charges, this case resembles models where lepton number is slightly broken (see for example [206, 211]). The Lagrangian is given by

$$\mathcal{L} = -\bar{\ell}\,\hat{\boldsymbol{Y}}_{\boldsymbol{e}}\, e\phi - \bar{\ell}\,\boldsymbol{\lambda_1}^*\, N_1\tilde{\phi} - \epsilon_\lambda\,\bar{\ell}\,\boldsymbol{\lambda_2}^*\, N_2\tilde{\phi} - \frac{1}{2}N_1^T\, CM\, N_2 - \frac{1}{2}\epsilon_N N_a^T\, CM_{aa}\, N_a + \text{H.c.}\,. \quad (5.8)$$

The $\epsilon_{\lambda,N}$ parameters determine the amount of $U(1)_R$ breaking and are thus tiny. The diagonalization of the Majorana RH neutrino mass matrix leads to two quasi-degenerate states with masses given by

$$M_{N_{1,2}} = M \mp \frac{M_{11} + M_{22}}{2}\epsilon_N\,. \quad (5.9)$$

In the basis in which the RH neutrino mass matrix is diagonal the Yukawa couplings become

$$\lambda_{ka} \to -\frac{(i)^a}{\sqrt{2}}\left[\lambda_{k1} + (-1)^a\epsilon_\lambda\lambda_{k2}\right]\,, \qquad (k = e,\mu,\tau \;\text{ and }\; a = 1,2)\,, \quad (5.10)$$

and the 5×5 neutral fermion mass matrix is similar as in type A models. However, due to the structure of the Yukawa couplings the effective light neutrino matrix, up to $\mathcal{O}(\epsilon_N\epsilon_\lambda^2)$, has the following form

$$\boldsymbol{m}_{\boldsymbol{\nu}}^{\mathbf{eff}} = -\frac{v^2\epsilon_\lambda}{M}|\boldsymbol{\lambda_1}||\boldsymbol{\Lambda}|\left(\hat{\boldsymbol{\lambda}}_{\mathbf{1}}^*\otimes\hat{\boldsymbol{\Lambda}}^* + \hat{\boldsymbol{\Lambda}}^*\otimes\hat{\boldsymbol{\lambda}}_{\mathbf{1}}^*\right)\,, \quad (5.11)$$

with

$$\hat{\boldsymbol{\Lambda}}^* = \hat{\boldsymbol{\lambda}}_{\mathbf{2}}^* - \frac{M_{11}+M_{22}}{4M}\frac{\epsilon_\lambda}{\epsilon_N}\hat{\boldsymbol{\lambda}}_{\mathbf{1}}^*\,. \quad (5.12)$$

Here aiming at relating the flavor structure of these models with low-energy observables, and following ref. [206], we expressed the parameter space vectors $\boldsymbol{\lambda_1}, \boldsymbol{\Lambda}$ in the light neutrino mass matrix in terms of their moduli $|\boldsymbol{\lambda_1}|, |\boldsymbol{\Lambda}|$ and unitary vectors $\hat{\boldsymbol{\lambda}}_{\mathbf{1}}, \hat{\boldsymbol{\Lambda}}$.

Note that in these models lepton number is broken even when $U(1)_R$ is an exact symmetry of the Lagrangian. However due to the Yukawa structure and degeneracy of the RH neutrino mass spectrum at this stage $\boldsymbol{m}_{\boldsymbol{\nu}}^{\mathbf{eff}} = 0$. Although a non-zero Majorana neutrino mass matrix arises only once the R breaking terms are present this does not imply that in the absence of lepton-number-violating interactions a Majorana mass matrix can be built. In that case—as can seen from Eq. (5.8)—only Dirac masses (see Appendix C.1) can be generated, as must be.

Since $\epsilon_\lambda \ll 1$ small neutrino masses do not require heavy RH neutrinos or small Yukawa couplings, thus potentially implying large lepton-flavor-violating effects. In that sense, as already stressed, these models resemble those in which lepton number is slightly broken but with lepton number as well as LFV taking place at the same scale M.

In contrast to models of type A, in this case due to the structure of the light Majorana neutrino mass matrix the vectors $\boldsymbol{\lambda_1}$ and $\boldsymbol{\Lambda}$ can be entirely determined by means of the solar and atmospheric mass scales and mixing angles, up to the factors $|\boldsymbol{\lambda_1}|$ and $|\boldsymbol{\Lambda}|$, without invoking a restrictive MLFV hypothesis. The relations are different for normal and inverted light neutrino mass spectra [206]:

- Normal hierarchical mass spectrum

$$\boldsymbol{\lambda_1} = |\boldsymbol{\lambda_1}|\,\hat{\boldsymbol{\lambda}}_{\mathbf{1}} = \frac{|\boldsymbol{\lambda_1}|}{\sqrt{2}}\left(\sqrt{1+\rho}\,\boldsymbol{U_3}^* + \sqrt{1-\rho}\,\boldsymbol{U_2}^*\right), \tag{5.13}$$

$$\boldsymbol{\Lambda} = |\boldsymbol{\Lambda}|\,\hat{\boldsymbol{\Lambda}} = \frac{|\boldsymbol{\Lambda}|}{\sqrt{2}}\left(\sqrt{1+\rho}\,\boldsymbol{U_3}^* - \sqrt{1-\rho}\,\boldsymbol{U_2}^*\right), \tag{5.14}$$

  where $\boldsymbol{U_i}$ denote the columns of the leptonic mixing matrix and

$$\rho = \frac{\sqrt{1+r}-\sqrt{r}}{\sqrt{1+r}+\sqrt{r}}\,, \qquad r = \frac{m_{\nu_2}^2}{m_{\nu_3}^2 - m_{\nu_2}^2}\,. \tag{5.15}$$

- Inverted hierarchical mass spectrum

$$\boldsymbol{\lambda_1} = |\boldsymbol{\lambda_1}|\,\hat{\boldsymbol{\lambda}}_{\mathbf{1}} = \frac{|\boldsymbol{\lambda_1}|}{\sqrt{2}}\left(\sqrt{1+\rho}\,\boldsymbol{U_2}^* + \sqrt{1-\rho}\,\boldsymbol{U_1}^*\right), \tag{5.16}$$

$$\boldsymbol{\Lambda} = |\boldsymbol{\Lambda}|\,\hat{\boldsymbol{\Lambda}} = \frac{|\boldsymbol{\Lambda}|}{\sqrt{2}}\left(\sqrt{1+\rho}\,\boldsymbol{U_2}^* - \sqrt{1-\rho}\,\boldsymbol{U_1}^*\right), \tag{5.17}$$

with

$$\rho = \frac{\sqrt{1+r}-1}{\sqrt{1+r}+1}\,, \qquad r = \frac{m_{\nu_2}^2 - m_{\nu_1}^2}{m_{\nu_1}^2}\,. \tag{5.18}$$

With these results at hand, the most relevant lepton-flavor-violating processes, which we discuss in turn, can be calculated.

5.3 Lepton-flavor-violating processes

In type A models the RH neutrino masses can be readily at the TeV scale for $\epsilon \sim 10^{-6}$. Since the Yukawa couplings scale with ϵ as well, type A models are—in that sense—on the same footing as the canonical type-I seesaw model (discussed in Appendix C), i.e. TeV RH neutrino masses imply tiny Yukawa couplings and thus negligible charged-lepton-flavor-violating-decay branching ratios. The main difference is that in the canonical case, sizable charged LFV via fine-tuned cancellations in the effective neutrino mass matrix, while no such effects are possible in the minimal type A models, since the relevant couplings are completely determined by light-neutrino mass and mixing parameters.

Type-B models, in contrast, may exhibit naturally large Yukawa couplings even for TeV-scale RH-neutrino masses (or even lighter masses, depending on the value of the $U(1)_R$ breaking parameter ϵ_λ). Accordingly, several charged-lepton-flavor-violating transition rates—induced by the RH neutrinos at the 1-loop level—can in principle reach observable levels. In what follow the allowed mass and Yukawa-normalization-factor ranges are studied by considering the following lepton-flavor-violating processes: $l_\alpha \to l_\beta\gamma$, $l_\alpha \to 3l_\beta$ and $\mu - e$ conversion in nuclei.

5.3.1 $l_\alpha \to l_\beta \gamma$ processes

Among these lepton-flavor-violating processes, presently the $\mu \to e\gamma$ transition is the most severely constrained. The MEG collaboration recently established an upper bound of 2.4×10^{-12} at the 90% CL [179]. For $\tau \to e\gamma$ and $\tau \to \mu\gamma$ on the other hand, the bounds are 3.3×10^{-8} and 4.4×10^{-8} at 90% CL [181], respectively. In the limit $m_{l_\beta} \ll m_{l_\alpha}$ the partial decay width for $l_\alpha \to l_\beta\gamma$ processes reads [212]

$$\Gamma(l_\alpha \to l_\beta\gamma) = \frac{\alpha\,\alpha_W^2}{256\,\pi^2}\,\frac{m_\alpha^5}{M_W^4}\,\left|G_\gamma^{l_\alpha l_\beta}\right|^2 = \frac{\alpha}{1024\,\pi^4}\,\frac{m_\alpha^5}{M_W^4}\,\left|\left(\boldsymbol{\lambda}\boldsymbol{G_\gamma}\boldsymbol{\lambda}^\dagger\right)_{\alpha\beta}\right|^2 , \tag{5.19}$$

where M_W is the $W^\pm$ mass, $\alpha_W = g^2/4\pi$ and the elements of the diagonal matrix $\boldsymbol{G_\gamma}$ are given in Eq. (D.1) in Appendix D. This function is such that in the limit $M_{N_a} \gg M_W$, $(G_\gamma)_{aa} \to M_W^2/2M_{N_a}^2$. The corresponding decay branching ratios are determined from the partial decay width after normalizing to $\Gamma^{l_\alpha}_{\rm Tot} = \hbar\,\tau_{l_\alpha}$, with τ_{l_α} the l_α charged lepton mean lifetime. In the limit $r_a \ll 1$, using Eq. (5.5) and taking into account the Yukawa rescaling $\boldsymbol{\lambda} \to \epsilon\boldsymbol{\lambda}$ the decay branching ratio in type A models can be written as

$$\mathrm{BR}(l_\alpha \to l_\beta\gamma) \simeq \frac{\alpha}{4096\pi^4}\,\frac{m_i^5}{\mu^4\epsilon^4}\,\frac{1}{\Gamma^{l_\alpha}_{\rm Tot}}\,\left|\left(\boldsymbol{\lambda}\boldsymbol{Y_N}^{-2}\boldsymbol{\lambda}^\dagger\right)_{\alpha\beta}\right|^2 . \tag{5.20}$$

Thus, assuming $\mathcal{O}(\boldsymbol{\lambda}, \boldsymbol{Y_N}) \sim 1$, for which $\mu \sim 10^{15}$ GeV and taking $\epsilon = 10^{-6}$, the value required for $\mathcal{O}$(TeV) RH neutrino masses, reads $\mathrm{BR}(\mu \to e\gamma) \simeq 10^{-30}$. As this behavior is extensible to other lepton-flavor-violating processes, this shows that in type-A models lepton-flavor-violating effects are negligibly small.

In type-B models in contrast such lepton-flavor-violating effects may be sizable. Using expression (5.10) for the Yukawa couplings, neglecting the piece proportional to ϵ_λ and taking the limit $M_{N_a} \gg M_W$, the decay branching ratios can be expressed in terms of the parameters $\boldsymbol{\lambda_1}$:

$$\mathrm{BR}(l_\alpha \to l_\beta\gamma) \simeq \frac{\alpha}{1024\pi^4}\,\frac{m_\alpha^5}{M^4}\,\frac{|\boldsymbol{\lambda_1}|^4}{\Gamma^{l_\alpha}_{\rm Tot}}\,\left|\hat{\lambda}_{\alpha 1}\,\hat{\lambda}^*_{\beta 1}\right|^2 . \tag{5.21}$$

Since the components of the unitary vector $\hat{\boldsymbol{\lambda}}_{\mathbf{1}}$ are entirely determined by low-energy observables (see Eqs. (5.13) and (5.16)) the size of these branching ratios—and that all the others discussed below—are controlled only by the parameters M and $|\boldsymbol{\lambda_1}|$, thus implying that for sufficiently light RH neutrino masses and large $|\boldsymbol{\lambda_1}|$ these processes may be measurable.

In order to quantify the size of these lepton-flavor-violating effects we randomly generate neutrino masses, mixing angles and Dirac and Majorana CP violating phases in their 2σ ranges for both normal and inverted hierarchical light neutrino mass spectra [52]. We also randomly generate the parameters $|\boldsymbol{\lambda_1}|$ and M in the ranges $[10^{-5}, 1]$ and $[10^2, 10^6]$ GeV allowing RH neutrino mass splittings in the range $[10^{-8}, 10^{-6}]$ GeV. With the numerical output we calculate the different lepton-flavor-violating decay branching ratios from Eq. (5.19), using the full loop function given in the Appendix, Eq. (D.1).

We find that radiative τ decay rates are always below their current bounds and barely reach values of 10^{-9} for RH neutrino masses around 100-200 GeV (values exceeding the current bounds are not consistent with the seesaw condition, that for concreteness we take as $\boldsymbol{m_D}\boldsymbol{M_N}^{-1} < 10^{-1}$), we thus focus on the $\mu \to e\gamma$ process. The results for the

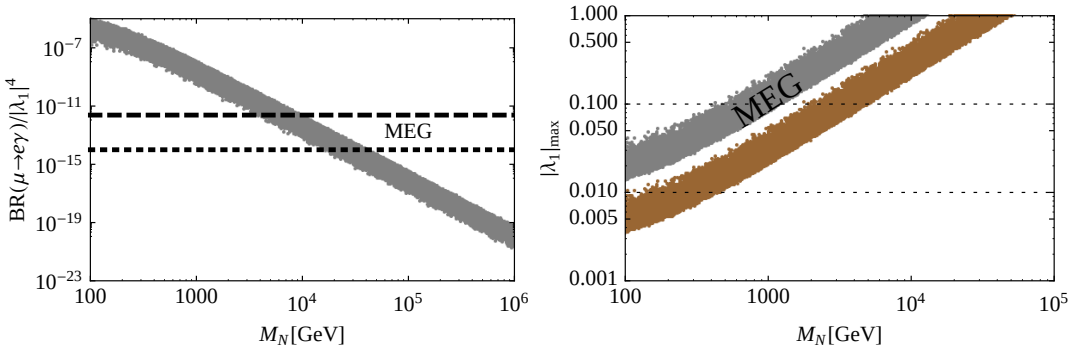

Figure 5.1: *Decay branching ratio $BR(\mu \to e\gamma)$ normalized to $|\boldsymbol{\lambda_1}|^4$ for a normal light neutrino mass spectrum as a function of the common RH neutrino mass (left-hand side plot). The upper horizontal dashed line indicates the current limit on $BR(\mu \to e\gamma)$ from the MEG experiment [179], whereas the lower dotted one marks prospective future experimental sensitivities [213]. The corresponding bounds on $|\boldsymbol{\lambda_1}|$ from the present [179] (upper gray band) and prospective future [213] (lower brown band) experimental searches are shown in the right handside plot. The widths of the bands are due to the uncertainties in the neutrino mass matrix parameters. The results for the inverted neutrino spectrum are very similar and are thus not shown separately.*

normal mass spectrum case are displayed in Figure 5.1 as a function of the common RH neutrino mass, $M_N = M$. We observe that $\mathrm{BR}(\mu \to e\gamma)$ can reach the current experimental limit reported by the MEG experiment [179] for RH neutrino masses $M_N < 0.1$ TeV, 1 TeV, 10 TeV provided $|\boldsymbol{\lambda_1}| \gtrsim 2 \times 10^{-2}$, 10^{-1}, 1, respectively. The results for the inverted light neutrino mass hierarchy are very similar and consistent with these values. Finally we note that the widths of the bands in Figure 5.1 (and similarly for all the other considered processes below) are solely due to the uncertainties in the light neutrino mass matrix parameters (mainly θ_{13} and the CP violating phases) and can thus be improved with more precise light neutrino data.

5.3.2 $l_\alpha \to l_\beta l_\beta l_\beta$ processes

The decay branching ratios for these processes have been calculated in [212]. The most constrained process in this case is $\mu^- \to e^+e^-e^-$ for which the SINDRUM experiment has placed a bound on the decay branching ratio of 10^{-12} at 90% CL [180]. For $\tau^- \to e^+e^-e^-$ and $\tau^- \to \mu^+\mu^-\mu^-$ the current bounds are 2.7×10^{-8} and 2.1×10^{-8}, respectively [182]. The decay branching ratios for these lepton-flavor-violating reactions are given by [212]

$$\begin{aligned}\mathrm{BR}(l_\alpha^- \to l_\beta^- l_\beta^+ l_\beta^-) = \frac{\alpha_W^4}{24576\pi^3}\frac{m_i^5}{M_W^4}\frac{1}{\Gamma^{l_\alpha}_{\mathrm{Total}}} \\ \left\{2\left|\frac{1}{2}F_{\mathrm{Box}}^{l_\alpha 3 l_\beta} + F_Z^{l_\alpha l_\beta} - 2s_W^2\left(F_Z^{l_\alpha l_\beta} - F_\gamma^{l_\alpha l_\beta}\right)\right|^2\right. \\ \left. +4s_W^4\left|F_Z^{l_\alpha l_\beta} - F_\gamma^{l_\alpha l_\beta}\right|^2 + 16 s_W^2 \mathbb{R}\mathrm{e}\left[\left(F_Z^{l_\alpha l_\beta} + \frac{1}{2}F_{\mathrm{Box}}^{l_\alpha 3 l_\beta}\right) G_\gamma^{l_\alpha l_\beta *}\right]\right.\end{aligned}$$

$$-48 s_W^4 \mathbb{R}\mathrm{e}\left[\left(F_Z^{l_\alpha l_\beta} - F_\gamma^{l_\alpha l_\beta}\right) G_\gamma^{l_\alpha l_\beta \beta *}\right] + 32 s_W^4 \left|G_\gamma^{l_\alpha l_\beta}\right|^2 \left(\ln \frac{m_\alpha^2}{m_\beta^2} - \frac{11}{4}\right)\Bigg\} . \tag{5.22}$$

Here $s_W = \sin\theta_W$, where θ_W is the weak mixing angle, and the functions $F_\gamma^{l_\alpha l_\beta}$, $F_Z^{l_\alpha l_\beta}$ and $F_{\text{Box}}^{l_\alpha 3 l_\beta}$ are form factors that involve the Yukawa couplings and loop functions arising from the γ, Z penguin and box diagrams that determine the the full process (see Appendix D for a compilation of these expressions and ref. [212] for their derivation).

Following the same numerical procedure as in the $l_\alpha \to l_\beta \gamma$ case and using the form factors given in the Appendix D we evaluate the $\mu^+ \to e^+e^-e^-$, $\tau^+ \to e^+e^-e^-$ and $\tau^+ \to \mu^+\mu^-\mu^-$ decay branching ratios for both, the normal and inverted light neutrino mass spectra. We find that $\tau^+ \to e^+e^-e^-$ and $\tau^+ \to \mu^+\mu^-\mu^-$ processes are always below $\sim 10^{-9}$ (due to the constraint enforced by the seesaw condition when $|\boldsymbol{\lambda_1}| > 10^{-1}$), so in Figure 5.2 we only display the results for $\mu^+ \to e^+e^-e^-$. We observe that the branching ratio can saturate the current experimental bound for RH neutrino masses $M_N < 0.1$ TeV, 1 TeV, 10 TeV provided $|\boldsymbol{\lambda_1}| \gtrsim 2\times 10^{-2}$, 10^{-1}, 1, respectively, very similar to the $\mu \to e\gamma$ case. The results for the inverted light neutrino mass hierarchy are again very similar and consistent with these values. As can be seen by comparing Figures 5.1 and 5.2, with the sensitivities of the planned future experiments [3] this process has the potential to probe considerably larger values of the RH neutrino masses (compared with $\mu \to e\gamma$), reaching RH neutrino mass scales in excess of $\mathcal{O}(10^5$ GeV) for $|\boldsymbol{\lambda_1}| \sim 1$. Finally we note that due to the strong $|\boldsymbol{\lambda_1}|$ dependence, values of $|\boldsymbol{\lambda_1}|$ below 10^{-3} are not expected to yield observable rates at near future experimental facilities even for RH neutrino masses of the order 100 GeV.

5.3.3 $\mu - e$ conversion in nuclei

Competitive LFV constraints can also be obtained from searches for $\mu - e$ conversion in nuclei. Currently the strongest bounds on $\mathrm{BR}_{\mu e} \equiv \Gamma_{\text{conversion}}/\Gamma_{\text{capture}}$ were set by the SINDRUM collaboration from experiments on titanium with $\mathrm{BR}_{\mu e}^{(\mathrm{Ti})} < 4.3\times 10^{-12}$ [215] and gold target setting $\mathrm{BR}_{\mu e}^{(\mathrm{Au})} < 7\times 10^{-13}$ [183], both at 90 %CL. The $\mu - e$ conversion bounds are expected to be further improved in the future by several orders of magnitude. According to proposals [188] and [189, 190], one can expect a sensitivity of 10^{-16} or even 10^{-18} by the PRISM/PRIME experiment.

To get the constraint in the $\mu - e$ channel from these experiments, one needs to compute the relevant transition matrix elements in different nuclei. A detailed numerical calculation has been carried out by [216] and their formula in Eq. (14) are used to calculate the desired conversion rates. They receive one-loop contributions from photonic penguins contributing to both effective dipole (A_R) and vector ($g_{LV}^{(u,d)}$) couplings, as well as Z penguins and W box diagrams (these only contribute to $g_{LV}^{(u,d)}$). Using the notation of [216] we thus have

$$\Gamma_{\text{conversion}} = 2G_F^2 \left|A_R^* D + (2g_{LV}^{(u)} + g_{LV}^{(d)})V^{(p)} + (g_{LV}^{(u)} + 2g_{LV}^{(d)})V^{(n)}\right|^2 , \tag{5.23}$$

3. The proposed *Mu3e* experiment at PSI aims for a sensitivity of 10^{-15} in its first phase and 10^{-16} in its second phase [214].

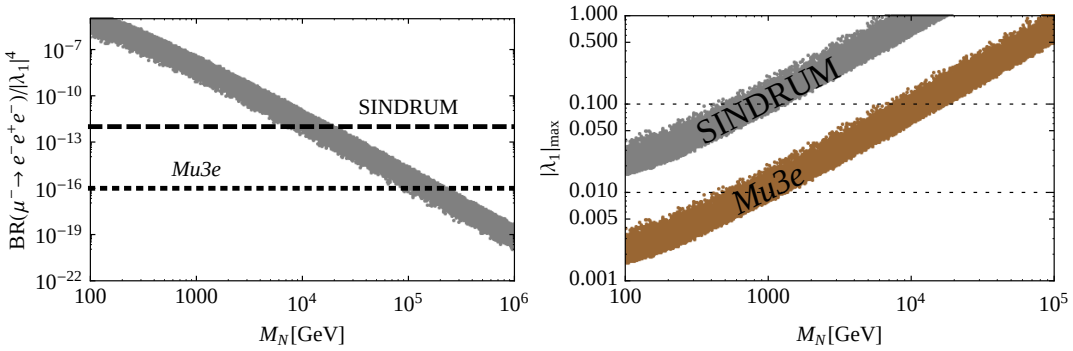

Figure 5.2: *Decay branching ratio $BR(\mu^- \to e^-e^+e^-)$ normalized to $|\boldsymbol{\lambda_1}|^4$ for normal light neutrino mass spectrum as a function of common RH neutrino mass (left-hand side plot). The upper horizontal dashed line indicates the current bound on the $\mu^- \to e^+e^-e^-$ rate placed by the SINDRUM experiment [180], whereas the lower dotted one illustrates prospective future experimental sensitivities of the Mu3e experiment [214]. The corresponding bounds on $|\boldsymbol{\lambda_1}|$ from the present [180] (upper gray band) and prospective future [214] (lower brown band) experimental searches are shown in the right-hand side plot. The widths of the bands are due to the uncertainties in the neutrino mass matrix parameters. The results for the inverted neutrino spectrum are very similar and are thus not shown separately.*

Nucleus	$D[m_\mu^{5/2}]$	$V^{(p)}[m_\mu^{5/2}]$	$V^{(n)}[m_\mu^{5/2}]$	$\Gamma_{\text{capture}}[10^6 s^{-1}]$
Ti^{48}_{22}	0.0864	0.0396	0.0468	2.59
Au^{197}_{79}	0.189	0.0974	0.146	13.07

Table 5.1: Data taken from Tables I and VIII of [216].

where G_F is the SM Fermi coupling constant and A_R, $g_{LV}^{(u,d)}$ are found to be ($Q_{u,d} = 2/3, -1/3$):

$$A_R^* = \frac{\sqrt{2}}{8G_F M_W^2}\frac{\alpha_W}{8\pi} e G_\gamma^{\mu e}\,, \tag{5.24}$$

$$g_{LV}^{(u)} = \frac{\sqrt{2}\alpha_W^2}{8G_F M_W^2}\left[\left(F_Z^{\mu e} + 2F_{\text{Box}}^{\mu 3e(1)}\right) - 4Q_u s_W^2\left(F_Z^{\mu e} - F_\gamma^{\mu e}\right)\right]\,, \tag{5.25}$$

$$g_{LV}^{(d)} = -\frac{\sqrt{2}\alpha_W^2}{8G_F M_W^2}\left[\left(F_Z^{\mu e} + \frac{1}{2}F_{\text{Box}}^{\mu 3e(1)}\right) + 4Q_d s_W^2\left(F_Z^{\mu e} - F_\gamma^{\mu e}\right)\right]\,. \tag{5.26}$$

Following the same numerical procedure as in Sections 5.3.1 and 5.3.2 the resulting $\mu - e$ conversion branching ratios are evaluated. Since both Ti and Au processes feature the same flavor structure, the differences between them are entirely determined by the numerical factors quoted in table 5.1. The Ti parameters entering in the conversion rate are on average a factor ~ 2.5 smaller than the ones for Au, whereas the capture rates differ by a factor ~ 5. Accordingly the difference between these branching ratios is a factor of ~ 2. Due to its more stringent experimental upper bound we thus display only the results for Au in Figure 5.3 for the case of the normal light-neutrino mass spectrum

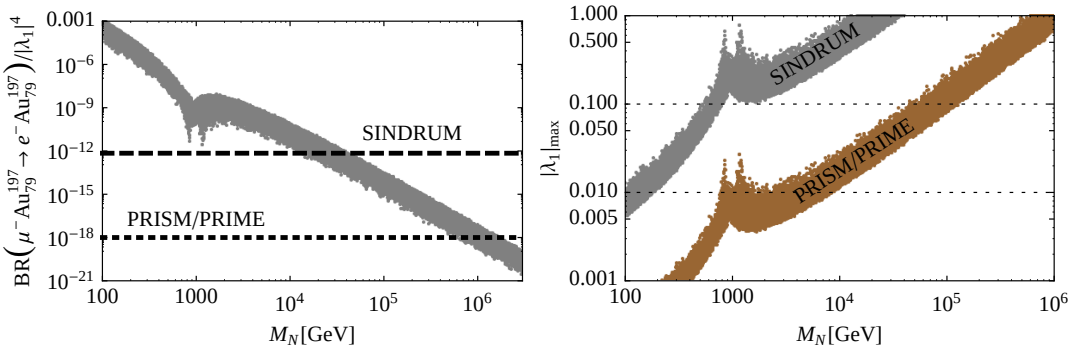

Figure 5.3: *Branching ratio* $BR(\mu^- \mathrm{Au}^{197}_{79} \to e^- \mathrm{Au}^{197}_{79})$ *normalized to* $|\boldsymbol{\lambda_1}|^4$ *as a function of the common RH neutrino mass for the light neutrino normal mass spectrum (left-hand side plot). The upper horizontal dashed line indicates the current bound on this process settled by the SINDRUM experiment [183], whereas the lower one indicates future experimental sensitivities of the PRISM/PRIME experiment [188–190]. The corresponding bounds on* $|\boldsymbol{\lambda_1}|$ *from the present [183] (upper gray band) and prospective future [188–190] (lower brown band) experimental searches are shown in the right-hand side plot. The widths of the bands are due to the uncertainties in the neutrino mass matrix parameters. The results for the inverted neutrino spectrum are very similar and are thus not shown separately.*

(the differences with the inverted mass spectrum case are again tiny). For $M_N \sim 2.5$ TeV the three pieces in Eq. (5.23) cancel. The dip in Figure 5.3 is due to this cancellation.

From Figure 5.3 it can be seen that the current experimental bound on this process imposes a constraint on the RH neutrino mass (as a function of $|\boldsymbol{\lambda_1}|$), which is roughly a factor of 2 stronger compared to bounds from $\mu \to e\gamma$ and $\mu \to 3e$ (except for the region around $M_N \sim 2.5$ TeV, as explained above). Furthermore, given the expected future sensitivities, $\mu^- \mathrm{Au}^{197}_{79} \to e^- \mathrm{Au}^{197}_{79}$ (and $\mu^- \mathrm{Ti}^{48}_{22} \to e^- \mathrm{Ti}^{48}_{22}$) could probe RH neutrino masses up to $\mathcal{O}(10^3$ TeV) , far above the values accessible in $\mu \to e\gamma$ and $\mu^- \to e^- e^+ e^-$, and thus constitutes the primary search channel for such scenarios of heavy RH neutrinos.

5.4 Primordial lepton asymmetries

The issue of primordial lepton asymmetries and the dynamics of the RH neutrinos are now examined. As already discussed, different R-charge assignments allow to define two types of models of which type B may yield sizable charged-lepton-flavor-violating decays. For these effects to take place, RH neutrino masses below 1 TeV as well as Yukawa couplings of order 10^{-2} or larger are needed. The washouts induced by such couplings, in that mass range, are so large that any lepton asymmetry generated via the out-of-equilibrium decays of the RH neutrinos will always yield a baryon asymmetry much smaller than the observed one [132]. [4]

Either producing a baryon asymmetry consistent with the observed value or not erasing a preexisting one via the dynamics of the RH neutrino states (in case the RH neutrinos

4. In models with a slightly broken lepton number the washout is tiny, as it is determined by the amount of lepton-number violation [217]. In the case discussed here since lepton number is broken even in the $U(1)_R$ symmetric phase the washouts are dominated—as usual—by $N_{R_{1,2}}$ inverse decays.

are still *light* and the resonant condition $M_{N_{R_2}} - M_{N_{R_1}} \sim \Gamma_{N_{R_1}}$ is not satisfied) requires small Yukawa couplings, thus rendering charged-lepton-flavor-violating decay branching ratios negligibly small. The phenomenological requirements of sizable charged-lepton-flavor-violating effects and the generation of a $B-L$ asymmetry (or the preservation of a preexisting one) are therefore mutually exclusive. Since these requirements cover non-overlapping regions in parameter space they are from that point of view complementary.

The generation of a $B-L$ asymmetry in the type-B models discussed here follows quite closely the analyzis done in Ref. [218]. Thus, this issue is not discussed here and instead the constraints on parameter space derived from the condition of not erasing an assumed preexisting $B-L$ asymmetry are studied. In type-I seesaw models with flavor symmetries in the lepton sector, as for example in MLFV models, the CP-violating asymmetry in RH-neutrino decays vanishes in the limit of exact flavor symmetry [219]. However, since in type-B models the MLFV hypothesis is a consequence of the intrinsic structure of the model this does not happen.

In order to quantify these effects from now on only the normal hierarchical light neutrino spectrum is considered. Results for the inverted hierarchical case resemble quite closely the ones reported here. It is first recalled that the washouts induced by both RH neutrino states (at $T \sim M$) on any primordial $B-L$ asymmetry are determined by the set of kinetic equations defined in Eq. (4.50). The matrix $\boldsymbol{C^{(\ell)}}$ is determined by the chemical equilibrium conditions imposed by the reactions that at the relevant temperature regime ($T \sim M$) are in thermal equilibrium [220]. The parameter κ_α, that determines the strength of the flavored washouts, is given by

$$\kappa_\alpha = \frac{\tilde{m}_\alpha}{m_\star} \quad \text{where} \quad \tilde{m}_\alpha = 2\frac{v^2}{M}|\lambda_{\alpha 1}|^2 \,. \tag{5.27}$$

The factor $m_\star \simeq 1.1 \times 10^{-12}$ GeV. In the basis in which the RH Majorana neutrino mass matrix is diagonal $N_{R_{1,2}}$ couple to the lepton doublets with strength $\lambda_{\alpha 1}$, the factor 2 in $\tilde{m}_\alpha$ is due to this fact. According to the parametrization in Eq. (5.13) the κ_α parameters can be written as

$$\kappa_\alpha = \frac{v^2}{m_\star}\frac{|\boldsymbol{\lambda_1}|^2}{M}|\hat{\lambda}_{\alpha 1}|^2 = \frac{v^2}{m_\star}\frac{|\boldsymbol{\lambda_1}|^2}{M}\left|\sqrt{1+\rho}\,U^*_{\alpha 3} + \sqrt{1-\rho}\,U^*_{\alpha 2}\right|^2 \,. \tag{5.28}$$

Thus, after fixing low-energy observables the values of the parameters κ_α depend only on M and $|\boldsymbol{\lambda_1}|$. Figure 5.4 (left-hand side plot) shows an example for the values of $\kappa_{e,\mu}$ (the κ_τ is smaller than κ_μ by less than a factor 10) obtained by enforcing neutrino data to lie within their 2σ experimental ranges [52, 221] and fixing for concreteness $|\boldsymbol{\lambda_1}| = 10^{-5}$. As can be seen, if the RH neutrinos are sufficiently light and the preexisting asymmetry is sufficiently large for a sizable asymmetry in the electron flavor to be kept.

An estimation of the $N_{1,2}$ washout effects can easily be done in the one-flavor approximation by taking $\boldsymbol{C^{(\ell)}} = \mathbb{I}$ in Eq. (4.50). The resulting equation can be analytically integrated yielding the following result for the final baryon asymmetry:

$$Y_{\Delta_B} = \frac{12}{37}\, Y^{(\mathrm{in})}_{\Delta_{B-L}}\, e^{-3\pi\kappa/8} \,. \tag{5.29}$$

Taking for $\kappa = \sum_{\alpha=e,\mu,\tau}\kappa_\alpha$, values as the ones shown in Figure 5.4, it becomes clear a primordial asymmetry may always survive the $N_{1,2}$ related washouts and yield a value consistent with the observed one.

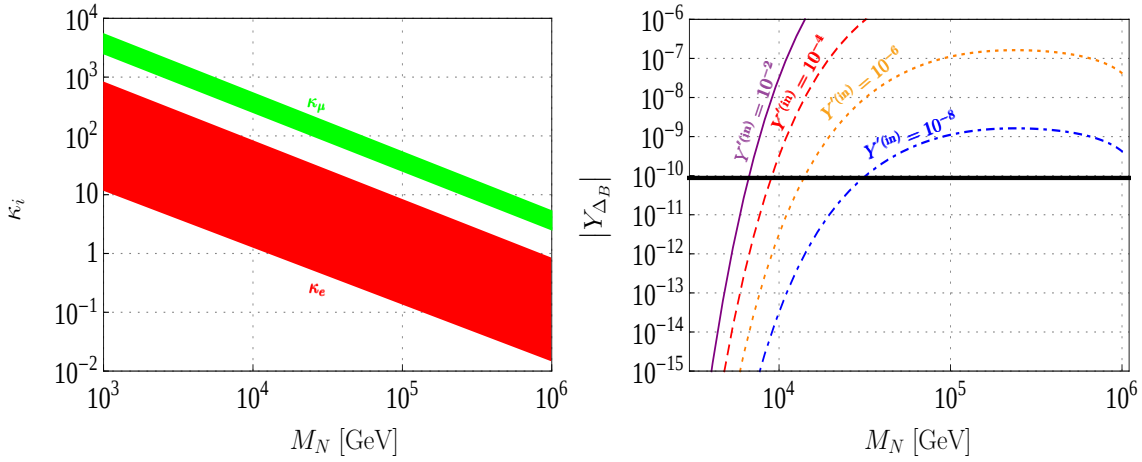

Figure 5.4: *Left-hand side plot: washout factors for muon and electron lepton flavors as a function of the common RH neutrino mass in the case of a normal hierarchical spectrum. Right-hand side plot: $|Y_{\Delta_B}|$ as a function of the common RH neutrino mass for several values of the assumed primordial $B-L$ asymmetry. The solid (black) horizontal line indicates the observed value of the baryon asymmetry.*

A precise treatment, however, requires the inclusion of flavor. In the mass range we are interested in ($[10^3, 10^6]$ GeV) all the standard model Yukawa processes (quarks and leptons) are in thermodynamical equilibrium [220]. Neglecting order one spectator processes, the kinetic eqs. (4.50) consist of three coupled differential equations accounting for the evolution of the $\Delta_{\tau,\mu,e}$ asymmetries. Defining the *asymmetry vector* $Y_\Delta = (Y_{\Delta_\tau}, Y_{\Delta_\mu}, Y_{\Delta_e})$ the system of coupled equations can be arranged in a single equation

$$\frac{d}{dz}\boldsymbol{Y_\Delta} = -\frac{v^2}{4m_\star}\frac{|\boldsymbol{\lambda_1}|^2}{M}\,\tilde{\boldsymbol{C}}^{(\boldsymbol{\ell})}\,\boldsymbol{Y_\Delta} K_1(z) z^3\,, \tag{5.30}$$

where $\tilde{C}^{(\ell)}_{\alpha\beta} = |\hat{\lambda}_{\alpha 1}|^2 C^{(\ell)}_{\alpha\beta}$ and the matrix $C^{(\ell)}$, at this stage, is given by [220]

$$\boldsymbol{C^{(\ell)}} = \frac{1}{711}\begin{pmatrix} 221 & -16 & -16 \\ -16 & 221 & -16 \\ -16 & -16 & 221 \end{pmatrix}. \tag{5.31}$$

By rotating the *asymmetry vector* in the direction in which $\tilde{C}^{(\ell)}$ becomes diagonal ($Y'_\Delta = P\,Y_\Delta$) the system of equations can be decoupled and thus solved analytically for Y'_Δ as in the unflavored regime:

$$\frac{d}{dz}Y'_\Delta = -\frac{v^2}{4m_\star}\frac{|\lambda_1|^2}{M}\,\tilde{C}^{(\ell)}_{\rm diag}\,Y'_\Delta K_1(z) z^3 \quad \text{with} \quad P\tilde{C}^{(\ell)}P^{-1} = \tilde{C}^{(\ell)_{\rm diag}}\,. \tag{5.32}$$

The solution reads

$$Y'_{\Delta_\alpha} = Y'^{(\rm in)}_{\Delta_\alpha}\, e^{-3\pi\kappa\tilde{c}_\alpha/8}\,, \tag{5.33}$$

where the $\tilde{c}_\alpha$'s ($\alpha = \tau, \mu, e$) are the eigenvalues of the matrix $\tilde{\boldsymbol{C}}^{(\boldsymbol{\ell})}$. The final baryon asymmetry in this case is therefore given by

$$Y_{\Delta_B} = \frac{12}{37}\sum_{j=\tau,\mu,e} Y_{\Delta_j} = \frac{12}{37}\sum_{\beta,\alpha=\tau,\mu,e}\left(P^{-1}\right)_{\beta\alpha} Y'^{(\rm in)}_{\Delta_\alpha}\, e^{-3\pi\kappa\tilde{c}_\alpha/8}\,. \tag{5.34}$$

In order to illustrate the effects of the $N_{1,2}$ related washouts on a preexisting $B-L$ asymmetry the light neutrino mixing angles and the atmospheric and solar scales are fixed to their best fit point values [52, 221], $\delta = \pi/2$, $\phi = 0$ and again $|\boldsymbol{\lambda_1}| = 10^{-5}$. Assuming the same primordial Δ_i asymmetries in each flavor, varying them from $10^{-8} - 10^{-2}$, and using Eq. (5.34) the resulting Y_{Δ_B} asymmetry is calculated. The results are displayed in Figure 5.4 (right-hand side plot). It can be seen that for the set of parameters chosen a Y_{Δ_B} in the observed range can always be obtained.

CONCLUSION

As it has been argued, several motivations for expecting new physical degrees of freedom to be present at certain unknown energy scale exist. Along this thesis quite a few arguments supporting that idea have been stressed (Chapters 1 and 4), and although it is true that those statements do not provide definitive conclusions about whether those degrees of freedom will at some point show up, they do provide strong reasons supporting that claim. Motivated by these observations, in this thesis several aspects of beyond SM scalar and fermion sectors have been studied.

In Part I, 2HDMs and 3HDMs were studied as well motivated cases of extended Higgs sectors. The results derived in each case as well as what they lead to are summarized below.

The main result of Chapter 2 is the demonstration that the mass spectrum of the general 2HDM can be studied in a reparametrization-invariant way within the Minkowski-space formalism [94,95]. The traces of the powers of the mass matrix and its determinant for all types of vacuum that can exist in the 2HDM were calculated. These results can now be used to get even more insight into the properties of the general 2HDM. The scalar propagators can be now written explicitly and can be used, for example, to improve the thermal one-loop calculations of [97]. In addition with these results it is now possible to address up to which extend the perturbativity and tree-level unitarity bounds, placed on the scalar potential, constraint the scalar masses. In the SM, there is a strong correlation between the value of the quartic coupling constant λ and the Higgs boson mass. Therefore, an upper limit on λ implies a corresponding upper limit on M_H. In the 2HDM, due to a large number of free parameters, the situation is much more complicated. In certain cases the scalars can be rather heavy without implying violation of the tree-level unitarity conditions [222]. With an explicit expression for the trace of the mass matrix, this problem can now be attacked in the most general case within the Minkowski-space technique. The only piece still missing is a reparametrization-covariant expression for the tree-level unitarity constraints.

In Chapter 3, a simple yet powerful and very intuitive geometric approach to minimization of highly symmetric potentials of non-minimal Higgs sectors was presented. These scenarios of highly symmetric Higgs potentials often need to be minimized. A geometric way of tackling the problem was proposed, which, surprisingly, is often much more efficient than the usual algebraic-based method. By construction, it gives the global

minimum for any set of free parameters of the potential, thus offering an intuitive understanding of how they affect the VEVs. For illustration, this method was applied to the S_4 and A_4-symmetric 3HDMs. Coexistence of minima of different types were discussed, and comments on the mathematical origin of geometrical CP-violation and on a new symmetry linking different minima were made. It has been shown that this method is capable of giving the positions of the global minima with very little calculations; in particular, it avoids the need to differentiate the potential, solve for stationary points, and check the positivity of the Hessian. In a single picture, it shows all points which can be the global minimum for any values of the parameters of the potential. It has been pointed out that this method constitutes a rather powerful tool in all situations where minimization of highly symmetric functions is required.

In Part II, the consequences for LFV of the extra $U(1)_R$ global factor appearing in the seesaw kinetic term have been studied. The analysis has been carried out under three assumptions: (*i*) The $U(1)_R$ symmetry is slightly broken; (*ii*) The leptons as well as the RH neutrinos carry non-trivial R-charges; (*iii*) RH neutrinos are assumed to be "light", $M_{N_R} \lesssim 10^2$ Tev. The results are summarized below.

A quite generic category of models where lepton-flavor-violating effects have large decay rates has been identified. In particular, it has been shown that given future experimental prospects, there is a high probability of observing rare muon decays if it turns out that these schemes are indeed realized in nature. This analysis has been completed with the derivation of further constraints on the parameter space of the corresponding models. These constraints have been derived by enforcing the RH neutrino dynamics to not wipe out a preexisting $B-L$ asymmetry (assumed to be generated at en energy scale much more above the RH neutrino scale) below the value required to address the cosmic baryon asymmetry puzzle. The findings show that both requirements: sizable LFV and preserving a $B-L$ in the correct amount so to generate the observed B asymmetry are mutually exclusive requirements.

APPENDIX A

ALGEBRA OF MATRICES Σ^μ AND Π^μ

In this Appendix the algebra (Σ^μ, Π^μ) formed with the matrices Σ^μ and Π^μ introduced in Chapter 2 is described.

The four-vector of matrices Σ^μ is introduced via Eq. (2.38). The full 8-by-8 matrices Σ^μ have block-diagonal form and are built from two identical 4-by-4 matrices, which are also denoted by the same letter Σ's and whose properties are described here.

Σ^0 is just the unit matrix, while the explicit expressions for Σ^i are:

$$\Sigma^1 = \begin{pmatrix} 0 & 0 & 1 & 0 \\ 0 & 0 & 0 & 1 \\ 1 & 0 & 0 & 0 \\ 0 & 1 & 0 & 0 \end{pmatrix}, \quad \Sigma^2 = \begin{pmatrix} 0 & 0 & 0 & 1 \\ 0 & 0 & -1 & 0 \\ 0 & -1 & 0 & 0 \\ 1 & 0 & 0 & 0 \end{pmatrix}, \quad \Sigma^3 = \begin{pmatrix} 1 & 0 & 0 & 0 \\ 0 & 1 & 0 & 0 \\ 0 & 0 & -1 & 0 \\ 0 & 0 & 0 & -1 \end{pmatrix}. \tag{A.1}$$

These matrices satisfy the Clifford algebra condition:

$$\{\Sigma^i, \Sigma^j\} = 2\delta^{ij}\mathbb{I}_4\,. \tag{A.2}$$

The set of Σ's is not closed under taking commutators. Instead, they can be expressed via real antisymmetric matrices Π^i:

$$\Pi^i \equiv \Pi^0\Sigma^i\,, \quad \text{where} \quad \Pi^0 = \begin{pmatrix} 0 & 1 & 0 & 0 \\ -1 & 0 & 0 & 0 \\ 0 & 0 & 0 & 1 \\ 0 & 0 & -1 & 0 \end{pmatrix}. \tag{A.3}$$

The matrix Π^0 is the generator of the simultaneous $SO(2)$ rotations between the real and imaginary parts of the two doublets; it commutes with all Σ^i and its square is equal to -1. The set of matrices Σ^i and Π^i now forms the algebra:

$$[\Sigma^i, \Sigma^j] = 2\epsilon^{ijk}\Pi^k\,, \quad [\Sigma^i, \Pi^j] = -2\epsilon^{ijk}\Sigma^k\,, \quad [\Pi^i, \Pi^j] = -2\epsilon^{ijk}\Pi^k\,. \tag{A.4}$$

Note that Π^i do form a closed algebra.

The algebra of Σ^i and Π^i is isomorphic to the usual Poincaré algebra of the generators of boosts and rotations. Using this, the following matrices can be introduced

$$X^i_\pm = \frac{1}{4}\left(\pm\Sigma^i - i\Pi^i\right), \tag{A.5}$$

which satisfy the following commutation laws:

$$[X^i_\pm, X^j_\pm] = i\epsilon^{ijk} X^k_\pm \,, \quad [X^i_\pm, X^j_\mp] = 0 \,. \tag{A.6}$$

Finally, note that any four-vector a_μ can be associated with a real symmetric matrix $A = a_\mu \Sigma^\mu$, which has the following properties:

$$\det A = (a_\mu a^\mu)^2 \,, \quad A^{-1} = \frac{a_\mu \bar{\Sigma}^\mu}{a_\mu a^\mu} \,, \quad \text{with} \quad \bar{\Sigma}^\mu \equiv (\Sigma^0, -\Sigma^i) \,. \tag{A.7}$$

APPENDIX B

THE S_4- AND A_4-SYMMETRIC 3HDM POTENTIALS

In this Appendix, the constraints on the borders of the orbit space of the S_4-symmetric potential presented in Chapter 3 are derived (see Figure 3.4). Moreover, for completeness, the Higgs mass spectra for all global minima possible in S_4- and A_4-symmetric 3HDM are presented.

B.1 The orbit space of the S_4-symmetric potential

In Chapter 3, it is claimed that the three-dimensional orbit space of the S_4-symmetric potential, Γ, must lie inside the truncated pyramid defined by

$$x, y, z \geq 0\,, \quad \frac{1}{4} \leq x + y + z \leq 1\,, \tag{B.1}$$

meaning that the orbit space sits inside a 3-dimensional pyramid in the (x, y, z)-space. However, it does not fill the entire pyramid. Below, the constraints on the borders of the orbit space inside the pyramid, which are represented in Figure 3.4, are presented.

These constraints are the following:

- Points F and B:
  The XZ plane was studied in detail in the toy model introduced in Section 3.3.2. From $1/4 \leq x + z \leq 1$, the minimum and maximum values of x on the X-axis are respectively $x_F = 1/4$ and $x_B = 1$, which are realized with

$$F : \begin{pmatrix} 0 \\ v \end{pmatrix} \begin{pmatrix} v\sin(\pi/3) \\ v\cos(\pi/3) \end{pmatrix} \begin{pmatrix} v\sin(-\pi/3) \\ v\cos(-\pi/3) \end{pmatrix}, \qquad B : \begin{pmatrix} 0 \\ v \end{pmatrix} \begin{pmatrix} 0 \\ v \end{pmatrix} \begin{pmatrix} 0 \\ v \end{pmatrix}. \tag{B.2}$$

- Points G and A:
  Resulting from $1/4 \leq x + z \leq 1$, the minimum and maximum values of z on the Z-axis are respectively $x_G = 1/4$ and $x_A = 1$, which are realized with

$$G : \begin{pmatrix} 0 \\ v \end{pmatrix} \begin{pmatrix} v \\ 0 \end{pmatrix} \begin{pmatrix} 0 \\ 0 \end{pmatrix}, \qquad A : \begin{pmatrix} 0 \\ v \end{pmatrix} \begin{pmatrix} 0 \\ 0 \end{pmatrix} \begin{pmatrix} 0 \\ 0 \end{pmatrix}. \tag{B.3}$$

- Point E:
  On the Y-axis $z = 0$, which in terms of the doublets translates to $|\phi_i^\dagger \phi_i| = v^2$. The most general case satisfying this condition is realized with VEVs of the form

$$\begin{pmatrix} 0 \\ v \end{pmatrix} \begin{pmatrix} v \sin\alpha \\ v \cos\alpha e^{i\eta_2} \end{pmatrix} \begin{pmatrix} v \sin\beta e^{i\eta_3} \\ v \cos\beta e^{i\eta_4} \end{pmatrix}.$$

  With this VEV x can be calculated

$$x = \frac{1}{3}\left[\cos^2\alpha\cos^2\eta_2 + (\cos\alpha\cos\beta\cos(\eta_4-\eta_2) + \sin\alpha\sin\beta\cos\eta_3)^2 + \cos^2\beta\cos^2\eta_4\right]. \tag{B.4}$$

  Since it is situated on the Y-axis, $x = 0$. The following four sets of conditions vanish x:

$$\begin{aligned}
1: &\quad \cos\eta_2 = 0, \quad \cos\eta_4 = 0, \quad \sin\alpha\sin\beta\cos\eta_3 = -\cos\alpha\cos\beta, \\
2: &\quad \cos\alpha = 0, \quad \cos\beta = 0, \quad \cos\eta_3 = 0\,, \\
3: &\quad \cos\alpha = 0, \quad \cos\eta_4 = 0, \quad \sin\beta\cos\eta_3 = 0\,, \\
4: &\quad \cos\eta_2 = 0, \quad \cos\beta = 0, \quad \sin\alpha\cos\eta_3 = 0\,.
\end{aligned} \tag{B.5}$$

  Substituting any of these sets in y

$$y = \frac{1}{3}\left[\cos^2\alpha\sin^2\eta_2 + (\cos\alpha\cos\beta\sin(\eta_4-\eta_2) + \sin\alpha\sin\beta\sin\eta_3)^2 + \cos^2\beta\sin^2\eta_4\right] \tag{B.6}$$

  results in $y = 1/3$, which proves that this point is the only point for which the orbit space touches the Y-axis. This point is realized at point E with

$$E: \begin{pmatrix} 0 \\ iv \end{pmatrix} \begin{pmatrix} v \sin\alpha \\ v \cos\alpha \end{pmatrix} \begin{pmatrix} v \sin\beta e^{i\eta_3} \\ v \cos\beta \end{pmatrix}, \quad \cos\alpha\cos\beta + \sin\alpha\sin\beta\cos\eta_3 = 0\,.$$

- Point D:
  In the YZ-plane $x = 0$, which in terms of the doublets translates to $\mathbb{R}\mathrm{e}(\phi_i^\dagger \phi_j) = 0$. The most general case satisfying this condition is realized with VEVs of the form

$$\begin{pmatrix} 0 \\ v_1 \end{pmatrix} \begin{pmatrix} 0 \\ iv_2 \end{pmatrix} \begin{pmatrix} 0 \\ 0 \end{pmatrix}. \tag{B.7}$$

  With this VEV y can be calculated

$$y = \frac{\mathbb{I}\mathrm{m}^2(\phi_i^\dagger \phi_j)}{r_0^2} = \frac{3(v_1 v_2)^2}{({v_1}^2 + {v_2}^2)^2}\,, \tag{B.8}$$

  which has maximum value $y_{max} = 3/4$ at $v_1 = v_2$. Therefore, point C in the YZ-plane realizes a vertex of the orbit space with

$$D: \begin{pmatrix} 0 \\ v \end{pmatrix} \begin{pmatrix} 0 \\ iv \end{pmatrix} \begin{pmatrix} 0 \\ 0 \end{pmatrix}. \tag{B.9}$$

- Point C:
  In the XY-plane $z = 0$, which in terms of the doublets translates to $|\phi_i^\dagger \phi_i| = v^2$. The most general neutral VEV satisfying this condition is realized with

$$\begin{pmatrix} 0 \\ ve^{i\eta_2} \end{pmatrix} \begin{pmatrix} 0 \\ ve^{i\eta_3} \end{pmatrix} \begin{pmatrix} 0 \\ v \end{pmatrix} . \tag{B.10}$$

  With this VEV y can be calculated

$$y = \frac{1}{3}\left(\sin^2\eta_2 + \sin^2(\eta_3 - \eta_2) + \sin^2\eta_3\right) . \tag{B.11}$$

  Trying to maximize y, one gets the condition $\sin(2\eta_2) = -\sin(2\eta_3) = \sin 2(\eta_3 - \eta_2)$, which requires $\eta_2 = -\eta_3$ or $\eta_2 = n\pi/2 \pm \eta_3$, for $\eta_2 = n\pi/2$ or $\eta_2 = n\pi/2 + \pi/6$. Substituting each of these four conditions in y, leads to $y_{max} = 3/4$, which is realized in

$$C : \begin{pmatrix} 0 \\ ve^{2i\pi/3} \end{pmatrix} \begin{pmatrix} 0 \\ ve^{-2i\pi/3} \end{pmatrix} \begin{pmatrix} 0 \\ v \end{pmatrix} . \tag{B.12}$$

- Edge CD;
  The border of the orbit space at $y = 3/4$ represents neutral vacua, therefore the upper components of the most general VEV satisfying this condition are all zero. With $y = 3/4$, the condition $x + z = 1/4$ which is satisfied in the most general case hold with

$$\begin{pmatrix} 0 \\ v_2 e^{i\xi} \end{pmatrix} \begin{pmatrix} 0 \\ v_2 e^{-i\xi} \end{pmatrix} \begin{pmatrix} 0 \\ v_1 \end{pmatrix} . \tag{B.13}$$

  With this VEV y can be calculated as

$$y = \frac{\mathbb{I}\mathrm{m}^2(\phi_i^\dagger \phi_j)}{r_0^2} = \frac{3}{(1+2r)^2}\left[2r\sin^2\xi + r^2\sin^2(2\xi)\right] , \tag{B.14}$$

  where $(v_2/v_1)^2 = r^2$. To maximize y, $\cos(2\xi) = -r^2/2$. Substituting this value in y, results in $y = 3/4$ for any value of r, which means that $x + z = 1/4$ for any value of r. This condition represents the edge CD.
- Edge AB:
  In the XZ-plane $y = 0$, which in terms of the doublets translates into $\mathbb{I}\mathrm{m}(\phi_i^\dagger \phi_j) = 0$. The most general case satisfying this condition is realized with VEVs of the form

$$\begin{pmatrix} 0 \\ v_1 \end{pmatrix} \begin{pmatrix} 0 \\ v_2 \end{pmatrix} \begin{pmatrix} 0 \\ v_3 \end{pmatrix} .$$

  With this VEV x can be calculated as

$$x = \frac{3(v_1v_2)^2 + 3(v_2v_3)^2 + (v_3v_1)^2}{(v_1^2+v_2^2+v_3^2)^2}, \quad z = \frac{v_1^4 + v_2^4 + v_3^4 - v_1^2v_2^2 - v_2^2v_3^2 - v_3^2v_1^2}{(v_1^2+v_2^2+v_3^2)^2} . \tag{B.15}$$

  For every value of v_1, v_2 and v_3, $x+z = 1$, which represents the AB edge in Figure 3.4.

- Edge AD:
  In the YZ-plane $x = 0$, the most general case satisfying the condition $\mathbb{R}\mathrm{e}(\phi_i^\dagger \phi_j) = 0$ is realized with
  $$\begin{pmatrix} 0 \\ v_1 \end{pmatrix} \begin{pmatrix} 0 \\ iv_2 \end{pmatrix} \begin{pmatrix} 0 \\ 0 \end{pmatrix}.$$
  With this VEV y can be calculated as
  $$y = \frac{3(v_1 v_2)^2}{({v_1}^2 + {v_2}^2)^2}, \quad z = \frac{v_1^4 + v_2^4 - v_1^2 v_2^2}{({v_1}^2 + {v_2}^2)^2}. \tag{B.16}$$
  Introducing $\left(\frac{v_2}{v_1}\right)^2 = r^2$, y and z can be rewritten
  $$y = \frac{3r^2}{(1+r^2)^2}, \quad z = \frac{1 + r^4 - r^2}{(1+r^2)^2}. \tag{B.17}$$
  Thus, for any value of r, $y(r) + z(r) = 1$, which represents the border line in the YZ-plane, the AD edge.
- Edge BC:
  In the XY-plane $z = 0$, the most general VEV satisfying the condition $|\phi_i^\dagger \phi_i| = v^2$ is realized with
  $$\begin{pmatrix} 0 \\ ve^{i\xi_1} \end{pmatrix} \begin{pmatrix} 0 \\ ve^{i\xi_2} \end{pmatrix} \begin{pmatrix} 0 \\ ve^{i\xi_3} \end{pmatrix},$$
  which can be rotated to
  $$\begin{pmatrix} 0 \\ v \end{pmatrix} \begin{pmatrix} 0 \\ ve^{i\eta_2} \end{pmatrix} \begin{pmatrix} 0 \\ ve^{i\eta_3} \end{pmatrix}.$$
  With this VEV y and x can be calculated as
  $$y = \frac{1}{3}\left(\sin^2\eta_2 + \sin^2(\eta_3 - \eta_2) + \sin^2\eta_3\right) \quad , \quad x = \frac{1}{3}\left(\cos^2\eta_2 + \cos^2(\eta_3 - \eta_2) + \cos^2\eta_3\right). \tag{B.18}$$
  For every value of η_2 and η_3, $x + y = 1$, which represents the BC edge in Figure 3.4.

B.2 Higgs spectra of the S_4-symmetric potential

In the case of S_4-symmetric 3HDM analyzed in Chapter 3 the two simple VEV alignments were shown to be approximately related to each other by an unexpected symmetry of the orbit space. The remaining two points also follow this pattern. The alignment $(1, i, 0)$ becomes the global minimum if
$$\Lambda_2 < 0\,, \quad |\Lambda_2| > |\Lambda_3|\,, \quad \Lambda_1 > \Lambda_3\,, \quad 4\Lambda_0 + \Lambda_3 > 3|\Lambda_2|\,. \tag{B.19}$$
At this point the minimum condition and the charged Higgs masses read
$$v^2 = \frac{4\sqrt{3}M_0}{4\Lambda_0 + \Lambda_3 - 3|\Lambda_2|}\,, \quad m^2_{H_i^\pm} = \frac{1}{2}|\Lambda_2|v^2\,, \quad \frac{1}{4}(|\Lambda_2| - \Lambda_3)v^2\,, \tag{B.20}$$

and the neutral Higgs masses are

$$\begin{aligned} m^2_{H_i} &= \frac{1}{4}(\Lambda_1-\Lambda_3)v^2 \quad \text{(double degenerate)} \\ & \quad \frac{1}{2}(|\Lambda_2|+\Lambda_3)v^2\,, \quad \frac{1}{2}(|\Lambda_2|+\Lambda_1)v^2 \\ m^2_h &= \frac{1}{6}(4\Lambda_0+\Lambda_3-3|\Lambda_2|)v^2 = \frac{2}{\sqrt{3}}M_0\,. \end{aligned} \tag{B.21}$$

The alignment $(\pm 1, e^{i\pi/3}, e^{-i\pi/3})$ is the global minimum if

$$\Lambda_2<0\,, \quad |\Lambda_2|>|\Lambda_1|\,, \quad \Lambda_3>\Lambda_1\,, \quad 4\Lambda_0+\Lambda_1>3|\Lambda_2|\,. \tag{B.22}$$

At this point the minimum condition and the charged Higgs masses read

$$v^2=\frac{4\sqrt{3}M_0}{4\Lambda_0+\Lambda_1-3|\Lambda_2|}\,, \quad m^2_{H_i^\pm}=\frac{1}{2}|\Lambda_2|v^2, \quad \frac{1}{4}(|\Lambda_2|-\Lambda_1)v^2\,, \tag{B.23}$$

and the neutral Higgs masses are

$$\begin{aligned} m^2_{H_i} &= (a+b\pm\sqrt{a^2+b^2})\,v^2 \quad \text{(double degenerate)}, \quad a=\frac{|\Lambda_2|+\Lambda_1}{4}\,, \quad b=\frac{\Lambda_3-\Lambda_1}{6}\,, \\ m^2_h &= \frac{4\Lambda_0+\Lambda_1-3|\Lambda_2|}{6}v^2=\frac{2}{\sqrt{3}}M_0\,. \end{aligned} \tag{B.24}$$

Again, the perfect $\Lambda_1 \leftrightarrow \Lambda_3$ symmetry in v^2 is observed, in the minimum conditions and in the charged Higgs masses.

B.3 Higgs spectra of the A_4-symmetric potential

For completeness the Higgs mass spectrum at all four possible points of global minimum found in Chapter 3 are written.

- The VEV alignment $(1,1,1)$ remains stable in the presence of non-zero Λ_4 if it is not too large:

$$\Lambda_4^2<12\Lambda_1^2\,, \quad \Lambda_4^2<2(\Lambda_3+|\Lambda_1|)(\Lambda_2+|\Lambda_1|)\,. \tag{B.25}$$

  The value of v^2 is the same as in (3.17), while the masses become

$$\begin{aligned} m^2_{H_i^\pm} &= \left(\frac{1}{2}|\Lambda_1|\pm\frac{1}{4\sqrt{3}}\Lambda_4\right)v^2\,, \quad m^2_h=\frac{2}{3}(\Lambda_0-|\Lambda_1|)v^2\,, \\ m^2_{H_i} &= \frac{v^2}{12}\left[5|\Lambda_1|+3\Lambda_2+2\Lambda_3\pm\sqrt{(|\Lambda_1|+3\Lambda_2-2\Lambda_3)^2+12\Lambda_4^2}\right], \end{aligned}$$

  where the masses $m^2_{H_i}$ are double degenerate. Note that the presence of Λ_4 splits the charged Higgs masses while it preserves the degeneracy of the neutral Higgses.

- The vev alignment $(1,0,0)$ is also stable if Λ_4 satisfies

$$\Lambda_4^2 < 4(\Lambda_1 + |\Lambda_3|)(\Lambda_2 + |\Lambda_3|)\,. \tag{B.26}$$

The value of v^2 and the masses of the charged Higgs and the non-degenerate neutral bosons are the same as in (3.20), while the neutral Higgses from the second and third doublets get masses

$$m_{H_i}^2 = \frac{v^2}{4}\left[\Lambda_1 + \Lambda_2 + 2|\Lambda_3| \pm \sqrt{(\Lambda_1 - \Lambda_2)^2 + \Lambda_4^2}\right] \quad \text{(double degenerate)}\,.$$

Note that this Higgs spectrum remains 2HDM-like as it was in the S_4 case.

- The alignment $(1, e^{i\alpha}, 0)$ for a generic α parametrizes the points around the rim of the cone. For a given value of Λ_4, the value of α corresponding to the global minimum is fixed by the relation

$$\sin 2\alpha = -\frac{\Lambda_4}{\sqrt{(\Lambda_1 - \Lambda_2)^2 + \Lambda_4^2}}\,, \quad \cos 2\alpha = -\frac{\Lambda_1 - \Lambda_2}{\sqrt{(\Lambda_1 - \Lambda_2)^2 + \Lambda_4^2}}\,. \tag{B.27}$$

Geometrically, this result means that the global minimum lies on the rim in the same direction as the vector $\vec{n}$ projected on the plane of the rim. In this case the minimum condition is

$$v^2 = \frac{4\sqrt{3}M_0}{4\Lambda_0 + \Lambda_3 - 3\tilde{\Lambda}}\,, \tag{B.28}$$

where

$$\tilde{\Lambda} \equiv -(\Lambda_1 c_\alpha^2 + \Lambda_2 s_\alpha^2 + \Lambda_4 c_\alpha s_\alpha) = \frac{1}{2}\left[\sqrt{(\Lambda_1 - \Lambda_2)^2 + \Lambda_4^2} - (\Lambda_1 + \Lambda_2)\right] > 0\,, \tag{B.29}$$

and the mass spectrum is

$$\begin{aligned}
m_{H_i^\pm}^2 &= \frac{1}{2}v^2\tilde{\Lambda}\,, \quad \frac{1}{4}v^2(\tilde{\Lambda} - \Lambda_3), \\
m_{H_i}^2 &= \frac{1}{4}v^2\left[-(\Lambda_3 + \tilde{\Lambda}) + (1 \pm \cos 3\alpha)\sqrt{(\Lambda_1 - \Lambda_2)^2 + \Lambda_4^2}\right], \\
&\quad \frac{1}{2}v^2(\Lambda_1 + \Lambda_2 + 2\tilde{\Lambda})\,, \qquad \frac{1}{2}v^2(\Lambda_3 + \tilde{\Lambda})\,, \\
m_h^2 &= \frac{v^2}{6}(4\Lambda_0 + \Lambda_3 - 3\tilde{\Lambda}) = \frac{2M_0}{\sqrt{3}}\,.
\end{aligned} \tag{B.30}$$

Note that presence of $\cos 3\alpha$ in one pair of masses is natural and it reflects the triangle symmetry of the A_4 orbit space shown in Figure. 3.4. All other quantities are rotationally invariant, corresponding to the rotational symmetry of the cone.
In the limit $\Lambda_4 \to 0$, the minimum is obtained at $\alpha \to \pi/2$, $\tilde{\Lambda} \to -\Lambda_2$, and these spectra turn into the S_4-spectra found in Section 3.3.5. Note also that the three points on the rim with $\cos 3\alpha = \pm 1$ can never be "good minima" because mass terms are obtained with coefficients $\pm(\Lambda_3 + \tilde{\Lambda})$, which cannot be made positive simultaneously. These three points lie, in fact, on the three long directrices of the cone.

- Finally, in the case of the alignment $(\pm 1, e^{i\alpha}, e^{-i\alpha})$, with $\alpha = \pi/3$, a convenient notation is introduced

$$\sin\gamma = \frac{\Lambda_4}{\sqrt{(\Lambda_1-\Lambda_2)^2+\Lambda_4^2}}\,, \quad \cos\gamma = \frac{\Lambda_1-\Lambda_2}{\sqrt{(\Lambda_1-\Lambda_2)^2+\Lambda_4^2}}\,, \tag{B.31}$$

and

$$\tilde{\Lambda} = \Lambda_1 c_\alpha^2 + \Lambda_2 s_\alpha^2 + \Lambda_4 c_\alpha s_\alpha = \frac{1}{2}\left[\Lambda_1+\Lambda_2+\cos(2\alpha-\gamma)\sqrt{(\Lambda_1-\Lambda_2)^2+\Lambda_4^2}\right]\,. \tag{B.32}$$

Then, the value of v^2 is

$$v^2 = \frac{\sqrt{3}M_0}{\Lambda_0+\tilde{\Lambda}}\,, \tag{B.33}$$

the charged Higgs masses are

$$m^2_{H_i^\pm} = -\frac{1}{2}v^2\left(\Lambda_2+\frac{\sqrt{3}}{2}\Lambda_4\right) \quad \text{and} \quad -\frac{1}{4}v^2\left(\Lambda_1+\Lambda_2+\frac{2}{\sqrt{3}}\Lambda_4\right)\,. \tag{B.34}$$

The neutral Higgs spectrum contains, as usual, h with mass $m_h^2 = 2M_0/\sqrt{3}$ and two pairs of degenerate Higgses with masses

$$\begin{aligned} m^2_{H_i} \;=\; & \frac{v^2}{6}\Bigg[\Lambda_3+\frac{3}{2}(\Lambda_1+\Lambda_2)-4\tilde{\Lambda} \\ & \pm\sqrt{\left(\Lambda_3-\frac{3}{2}(\Lambda_1+\Lambda_2)+2\tilde{\Lambda}\right)^2+3\left[(\Lambda_1-\Lambda_2)^2+\Lambda_4^2\right]\sin^2(2\alpha-\gamma)}\Bigg]\,. \end{aligned} \tag{B.35}$$

In the S_4-symmetric case ($\Lambda_4 = 0$ and $\gamma = 0$), the results of Section 3.3.5 is recovered.

APPENDIX C

STANDARD SEESAW LAGRANGIAN

In this Appendix some well standard results as well as the notation used in Chapter 4 and 5 are presented. It mainly deals with the type-I seesaw Lagrangian but it also covers some details about early Universe thermodynamics [223].

C.1 Dirac and Majorana neutrinos

In relativistic quantum field theory, a massless fermion is described by a two-component Weyl spinor field, $\chi_{L,R}$, whereas a massive fermion consists of a four-component spinor:

$$\chi = \chi_L + \chi_R = P_L\chi + P_R\chi\,, \tag{C.1}$$

with $P_{L,R}$ the chirality projector operators obeying $P_{L,R}^2 = P_{L,R}, P_L P_R = P_R P_L, P_L + P_R = 1$, and χ, for the moment, a four-component Dirac fermion. Accordingly, the mass term has the form

$$m\bar{\chi}\chi = m\overline{(\chi_L + \chi_R)}(\chi_L + \chi_R) = m(\bar{\chi}_L\chi_R + \bar{\chi}_R\chi_L)\,, \tag{C.2}$$

which means the mass term couples the LH and RH components of the fermion field, and therefore a massive field must have both components and couple fields of opposite chirality.

In the Dirac case the LH and RH components are independent. The field defined in that way involves four independent degrees of freedom: $\chi_L, \chi_R, \chi_L^c, \chi_R^c$ with

$$\chi^c = C\bar{\chi}^T = \gamma_2\chi^*, \tag{C.3}$$
$$\overline{\chi^c} = \chi^T C, \tag{C.4}$$

and where the particle-antiparticle conjugation operator C is defined according to

$$C = i\gamma_2\gamma_0\,, \tag{C.5}$$

and satisfies the following relations:

$$C^\dagger = C^T = -C, \quad C^2 = -1, \quad C\gamma_\mu C^{-1} = -\gamma_\mu^T\,. \tag{C.6}$$

From Eq. (C.3), (C.4), (C.6) and from the anti-commutation properties of the γ matrices, it can be seen that the C operator produces chirality flips when acting on fermion fields, namely

$$\begin{aligned} (\chi_{L,R})^c &= (\chi^c)_{R,L} = P_{L,R}\chi^c, \\ \overline{\chi^c}_{L,R} &= \overline{\chi^c} P_{L,R}. \end{aligned} \tag{C.7}$$

In the Majorana case, the Weyl spinors are subject to the constraint $\chi_R = (\chi_L)^c = (\chi^c)_R$ ans so Eq. (C.1) becomes

$$\chi = \chi_L + \eta(\chi^c)_R = \chi_L + \eta(\chi_L)^c\,, \tag{C.8}$$

where $\eta = e^{i\alpha}$ is a phase factor with an arbitrary phase α. Thus, for a C-conjugate field $\chi^c = \eta^*\chi$ holds. Consequently, for Majorana fermions with $\chi^c_{L,R}$ given by $\chi^c_{L,R} = C\bar{\chi}^T_{L,R}$, the mass term in (C.2) turns out to have the form

$$-\mathcal{L}_m = \frac{1}{2}[\overline{\chi}_L m^T(\chi_L)^c + \overline{\chi^c}_R m\chi_R] + \text{H.c.} = \frac{1}{2}(m^\dagger\chi^\dagger P_R C\chi^* - m\chi^T C P_R\chi)\,. \tag{C.9}$$

Note that charged particles can only have a Dirac mass term. The Majorana mass term is not invariant under $U(1)$ transformations and thus breaks $U(1)$ charges.

Few words are in order before proceeding with the seesaw Lagrangian. If neutrinos were to be Dirac particles, of course their mass terms must have Dirac form i.e. must have a structure given by (C.2). This observation, coupled with their gauge quantum numbers, requires an extension of the SM fermion sector to include RH neutrinos N_R. Once this is done, the Yukawa couplings are determined by the following Lagrangian

$$-\mathcal{L}_Y = \ell_L \boldsymbol{\lambda} N_R\tilde{\phi} + \text{H.c.}\,. \tag{C.10}$$

This means that after EWSB the neutrino mass matrix will have the form:

$$m_{\nu_{ij}} = v\lambda_{ij}\,. \tag{C.11}$$

Consistency with data (see Table (4.1)) then requires the largest Yukawa coupling to be of order $O(\lambda) \sim 10^{-11}$. On the other hand, the RH neutrinos being SM singlets allow the introduction of a Majorana mass term, that if added completely changes the resulting picture, as it is now discussed in turn.

C.2 RH neutrinos

In the basis where the RH neutrinos mass matrix as well as the charged lepton Yukawa matrix are diagonal, the most general Lagrangian, once RH neutrinos are included, reads

$$-\mathcal{L}_Y = \bar{\ell}_L \boldsymbol{\lambda^*} N_R\tilde{\phi} + \frac{\mu}{2} N_R^T C\hat{\boldsymbol{Y}}^*_{\boldsymbol{N}} N_R + \text{H.c.}\,, \tag{C.12}$$

where the RH Majorana mass matrix has been written as $\hat{\boldsymbol{M}}_{\boldsymbol{N}} = \mu\hat{\boldsymbol{Y}}_{\boldsymbol{N}}$. With the SM scalar doublet parametrized as [1]

$$\phi = \frac{1}{\sqrt{2}}\begin{pmatrix} G^+ \\ (h^0 + iG^0 + v)/\sqrt{2} \end{pmatrix}\,, \tag{C.13}$$

1. In order to follow the usual notation used in seesaw contexts, from now on the notation adopted in Chapter 1 (Eqs. (1.17) and (1.45)) is changed.

and with $\tilde{\phi} = i\tau_2\phi^*$, the different pieces of the Lagrangian in C.12 read

$$-\mathcal{L}_m = \overline{\nu}_L \boldsymbol{m_D}^* N_R + \overline{N}_R \boldsymbol{m_D}^T \nu_L + \frac{\mu}{2}\overline{N}_R C\hat{\boldsymbol{Y}}_{\boldsymbol{N}}\overline{N}_R^T + \frac{\mu}{2}N_R^T C\hat{\boldsymbol{Y}}_{\boldsymbol{N}}^* N_R\,, \tag{C.14}$$

$$\mathcal{L}_{h^0} = \frac{-h^0}{\sqrt{2}}(\overline{\nu}_L \boldsymbol{\lambda}^* N_R + \overline{N}_R \boldsymbol{\lambda}^T \nu_L), \tag{C.15}$$

$$\mathcal{L}_{G^0} = \frac{-iG^0}{\sqrt{2}}(\overline{\nu}_L \boldsymbol{\lambda}^* N_R - \overline{N}_R \boldsymbol{\lambda}^T \nu_L), \tag{C.16}$$

$$\mathcal{L}_{G^\pm} = \frac{G^-}{\sqrt{2}}\bar{l}_L \boldsymbol{\lambda}^* N_R + \frac{G^+}{\sqrt{2}}\overline{N}_R \boldsymbol{\lambda}^T l_L. \tag{C.17}$$

In order to facilitate the following calculation, in Eq. (C.14) the full Lagrangian, including the Hermitian conjugate part, has been written, and as usual the Dirac mass matrix has been defined as $\boldsymbol{m_D} = v\boldsymbol{\lambda}$ where $(\sqrt{2})^{-1}$ factor has been absorbed in the VEV so now $v \simeq 174$ GeV. The Lagrangian in (C.14) can be expressed in terms of the flavor vector $\Psi_L = (\nu_L, N_R^C)$:

$$\begin{aligned}
-\mathcal{L}_m &= \overline{N}_R \boldsymbol{m_D}^T \nu_L + \frac{\mu}{2}\overline{N}_R C\hat{\boldsymbol{Y}}_{\boldsymbol{N}}\overline{N}_R^T + \text{H.c.} \\
&= \frac{1}{2}\overline{N}_R \boldsymbol{m_D}^T \nu_L + \frac{1}{2}\overline{N}_R \boldsymbol{m_D}^T \nu_L + \frac{\mu}{2}(C\overline{N}_R^T)^T C\hat{\boldsymbol{Y}}_{\boldsymbol{N}} C\overline{N}_R^T + \text{H.c.} \\
&= \frac{1}{2}(C\overline{N}_R^T)^T C\boldsymbol{m_D}^T \nu_L + \frac{1}{2}\nu_L^T C\boldsymbol{m_D} C\overline{N}_R^T + \frac{\mu}{2}(C\overline{N}_R^T)^T C\hat{\boldsymbol{Y}}_{\boldsymbol{N}} C\overline{N}_R^T + \text{H.c.} \\
&= \frac{1}{2}(N_R^c)^T C\boldsymbol{m_D}^T \nu_L + \frac{1}{2}\nu_L^T C\boldsymbol{m_D} N_R^c + \frac{\mu}{2}(N_R^c)^T C\hat{\boldsymbol{Y}}_{\boldsymbol{N}} N_R^c + \text{H.c.} \\
&= \frac{1}{2}\Psi_L^T C \begin{pmatrix} \boldsymbol{0}_{3\times 3} & \boldsymbol{m_D} \\ \boldsymbol{m_D}^T & \mu\hat{\boldsymbol{Y}}_{\boldsymbol{N}} \end{pmatrix} \Psi_L + \text{H.c.} \\
&= \Psi_L^T C\boldsymbol{\mathcal{M}_N}\Psi_L + \text{H.c.}\,.
\end{aligned} \tag{C.18}$$

In terms of the mass eigenstates defined as

$$\chi_L = \boldsymbol{W}^\dagger \Psi_L\,, \tag{C.19}$$

with $\boldsymbol{W}$ a 6×6 unitary matrix, the Lagrangian in (C.18) can be recasted according to

$$\begin{aligned}
-\mathcal{L}_m &= \frac{1}{2}C\chi_L^T \hat{\boldsymbol{\mathcal{M}}}_{\boldsymbol{N}}\chi_L + \text{H.c.} \\
&= \frac{1}{2}\sum_{i=1}^{6} m_{\chi_i}\left(\chi_{L_i}^T C\chi_{L_i} + \chi_{L_i}^\dagger C^\dagger \chi_{L_i}^*\right) \\
&= \frac{1}{2}\sum_{i=1}^{6} m_{\chi_i}\left(\overline{\chi}_{L_i}^c \chi_{L_i} + \overline{\chi}_{L_i}\gamma_0 C^\dagger \gamma_0 \gamma_0 \chi_{L_i}^*\right) \\
&= \frac{1}{2}\sum_{i=1}^{6} m_{\chi_i}\left(\overline{\chi}_{L_i}^c \chi_{L_i} + \overline{\chi}_{L_i}\chi_{L_i}^c\right).
\end{aligned} \tag{C.20}$$

With the aid of Eq. (C.8) finally the Lagrangian in (C.20) can be written in a quite compact form:

$$-\mathcal{L}_m = \frac{1}{2}\sum_{i=1}^{6} m_{\chi_i}\overline{\chi}_i\chi_i\,. \tag{C.21}$$

with $\chi_i = \chi_{L_i} + \chi^c_{L_i}$. The 6×6 neutral mass matrix $\boldsymbol{\mathcal{M}_N}$ in the limit

$$-\boldsymbol{\xi} = \boldsymbol{m_D}(\mu\hat{\boldsymbol{Y}}_{\boldsymbol{N}})^{-1} \ll 1\,, \tag{C.22}$$

can be perturbatively diagonalized via the mixing matrix given by

$$\boldsymbol{W} = \begin{pmatrix} \mathbb{I}_{3\times 3} & -\boldsymbol{\xi}^* \\ \boldsymbol{\xi}^T & \mathbb{I}_{3\times 3} \end{pmatrix}\,, \tag{C.23}$$

where $\mathbb{I}_{3\times 3}$ is the 3×3 identity matrix. From (C.19) and (C.23), the massive Majorana fields can therefore be regarded as a superposition of EW doublets and singlets namely

$$\begin{aligned} \chi_{L_i} &= \Psi_{L_i} + \sum_{j=4}^{6}\xi^*_{ij}\Psi_{L_j}, \qquad i=1,2,3, \\ \chi_{L_i} &= -\sum_{j=1}^{3}\xi_{ij}\Psi_{L_j} + \Psi_{L_i}, \qquad i=4,5,6. \end{aligned} \tag{C.24}$$

The perturbative block-diagonalization of the mass matrix leads to

$$-\mathcal{L}_m = \frac{1}{2}\chi_L^T C\begin{pmatrix} \boldsymbol{m^{\nu}_{\text{eff}}} & \boldsymbol{0} \\ \boldsymbol{0} & \mu\hat{\boldsymbol{Y}}_{\boldsymbol{N}} \end{pmatrix}\chi_L + \text{H.c.}\,, \tag{C.25}$$

with the effective neutrino mass matrix given by

$$\boldsymbol{m^{\nu}_{\text{eff}}} = -\boldsymbol{m_D}\frac{\hat{\boldsymbol{Y}}_{\boldsymbol{N}}^{-1}}{\mu}\boldsymbol{m_D}^T = -\sum_{\alpha=1,2,3}\frac{Y^{-1}_{N_\alpha}}{\mu}m_{D_\alpha}\otimes m_{D_\alpha}\,, \tag{C.26}$$

where in the last equality the mass matrix has been written as the outer product of the parameter space vectors $m^T_{D_\alpha} = (m_{D_{\alpha 1}}, m_{D_{\alpha 2}}, m_{D_{\alpha 3}})$. The diagonalization of this mass matrix through the leptonic mixing matrix $\boldsymbol{U}$ gives rise to the LH neutrino mass spectrum:

$$\hat{\boldsymbol{m}}^{\boldsymbol{\nu}} = \boldsymbol{U}^T\boldsymbol{m^{\nu}_{\text{eff}}}\boldsymbol{U}\,. \tag{C.27}$$

Splitting the mixing matrix $\boldsymbol{W}$ according to

$$\boldsymbol{W} = \begin{pmatrix} (\boldsymbol{W_L})_{3\times 6} \\ (\boldsymbol{W_R}^*)_{3\times 6} \end{pmatrix} = \begin{pmatrix} \mathbb{I}_{3\times 3} & -\boldsymbol{\xi}^*_{3\times 3} \\ \boldsymbol{\xi}^T_{3\times 3} & \mathbb{I}_{3\times 3} \end{pmatrix}\,, \tag{C.28}$$

where $\boldsymbol{W_L}$ and $\boldsymbol{W_R}$ account for the doublet and singlet components of the massive Majorana fields, the LH and RH fields can be expressed as

$$\nu_L = \boldsymbol{W_L}\chi_L = \boldsymbol{W_L}P_L\chi, \tag{C.29}$$

$$N_R^c = \boldsymbol{W_R}^* \chi_L = \boldsymbol{W_R}^* \chi_R^c \Rightarrow N_R = \boldsymbol{W_R} P_R \chi. \tag{C.30}$$

In terms of the expressions in (C.29) and (C.30), the Lagrangian in (C.15), (C.16) and (C.17) can be rewritten as follows:

$$\mathcal{L}_{h^0} = -\frac{h^0}{\sqrt{2}} \overline{\chi} (\boldsymbol{W_L}^\dagger \boldsymbol{\lambda}^* \boldsymbol{W_R} P_R + \boldsymbol{W_R}^\dagger \boldsymbol{\lambda}^T \boldsymbol{W_L} P_L) \chi, \tag{C.31}$$

$$\mathcal{L}_{G^0} = -\frac{iG^0}{\sqrt{2}} \overline{\chi} (\boldsymbol{W_L}^\dagger \boldsymbol{\lambda}^* \boldsymbol{W_R} P_R - \boldsymbol{W_R}^\dagger \boldsymbol{\lambda}^T \boldsymbol{W_L} P_L) \chi, \tag{C.32}$$

$$\mathcal{L}_{G^\pm} = \frac{G^-}{\sqrt{2}} \bar{l} \boldsymbol{\lambda}^* \boldsymbol{W_R} P_R \chi + \frac{G^+}{\sqrt{2}} \overline{\chi} \boldsymbol{W_R}^\dagger \boldsymbol{\lambda}^T P_L l. \tag{C.33}$$

Due to the field rotation in (C.29) the gauge boson interactions in (**??**) and (**??**) get modified as well. The resulting Lagrangians read:

$$\mathcal{L}_{W^\pm} = -\frac{g}{\sqrt{2}} \left(\overline{\chi} \gamma^\mu \boldsymbol{W_L} P_L l W_\mu^+ + \bar{l} \gamma^\mu \boldsymbol{W_L} P_L \chi W_\mu^- \right), \tag{C.34}$$

$$\mathcal{L}_Z = -\frac{g}{\cos\theta_W} \overline{\chi} \gamma^\mu \boldsymbol{W_L}^\dagger \boldsymbol{W_L} P_L \chi Z_\mu. \tag{C.35}$$

C.3 Thermodynamic of the early Universe

In this Appendix the conventions and the relevant equations that have been used in Section 4.5.1 and in Chapter 5 for the discussion of leptogenesis are presented. Using Maxwell-Boltzmann distribution functions for massless (relativistic) as well as massive species, and expressing the temperature dependence with the dimensionless temperature variable $z = M_{N_{R_a}}/T$, the equilibrium number densities are namely:

$$n_{N_{R_1}}^{\text{Eq}}(z) = \frac{M_{N_{R_1}}^3}{\pi^2} \frac{K_2(z)}{z}, \quad n_\ell^{\text{Eq}} = \frac{2M_{N_1}^3}{\pi^2} \frac{1}{z^3}, \tag{C.36}$$

where $K_2(z)$ is the modified Bessel function of the second type. With this approximation the energy density $\rho(z)$ and pressure $p(z)$ become

$$\rho(z) = \frac{3M_{N_{R_1}}^4}{z^4 \pi^2} g_*, \quad p(z) = \frac{M_{N_{R_1}}^4}{z^4 \pi^2} g_*, \tag{C.37}$$

where $g_* = \sum_{i=\text{All species}} g_i$ is the number of SM relativistic degrees of freedom (118, for $T > 300$ GeV). Accordingly, the expansion rate of the Universe and entropy density can be written as

$$H(z) = \sqrt{\frac{8g_*}{\pi}} \frac{M_{N_{R_1}}^2}{M_{\text{Planck}}} \frac{1}{z^2}, \quad s(z) = \frac{4M_{N_{R_1}}^3}{z^3 \pi^2} g_*, \tag{C.38}$$

with the Planck mass given by $M_{\text{Planck}} = 1.22 \times 10^{19}$ GeV. Using the expression for the entropy density in (C.38), the number-density-to-entropy ratio for both non-relativistic as well as relativistic species reads

$$Y_{N_{R_1}}^{\text{Eq}}(z) = \frac{n_{N_{R_1}}^{\text{Eq}}}{s(z)} = \frac{z^2 K_2(z)}{4g_*}, \quad Y_\ell^{\text{Eq}} = \frac{1}{2g_*}. \tag{C.39}$$

Finally, the decay reaction density, that is to say the number of reactions per unit volume and per unit time, is given by

$$\gamma_D(z) = \frac{1}{\pi^3} \frac{M_{N_{R_1}}^2}{v^2} \frac{K_1(z)}{z} \tilde{m}_1 \,, \tag{C.40}$$

with $K_1(z)$ the Bessel function of first type and the parameter $\tilde{m}_1$ defined according to

$$\tilde{m}_1 = \frac{M_{N_{R_1}}}{v^2} (\lambda^\dagger \lambda)_{11} \,. \tag{C.41}$$

APPENDIX D

FORMULAS AND FEYNMAN DIAGRAMS FOR LFV PROCESSES

In this Appendix the formulas used for the calculation of the charged lepton-flavor-violating decays discussed in Sections 5.3.1 and 5.3.2 are summarized. The results presented here were extracted from Ref. [212] and adapted to our notation. In what follows the parameters r_a are defined according to $r_a = M_W^2/M_{N_{R_a}}^2$.

The Feynman diagrams contributing to the $l_\alpha \to l_\beta \gamma$ process in the type-I seesaw model are illustrated in Figure D.1. The various contributions to the $l_\alpha \to l_\beta l_\beta l_\beta$ process can be divided in two classes: penguin and box diagrams. The former proceeding via either γ or Z penguins are illustrated in Figures D.1 and D.2 (taking into account that two external fermion lines should be attached to the corresponding vector boson line). The latter are illustrated in Figure D.3. For $\mu - e$ conversion in nuclei the relevant Feynman diagrams are shown in Figure D.4, where the calculation involves in addition extra nuclear form factors (see Chapter 5 and [216] for precise details).

The γ penguin contribution can be split in two pieces corresponding to the photon being either on-shell or off-shell. For the on-shell piece, the one that determines the $l_\alpha \to l_\beta \gamma$ process, the following functions are used

$$G_\gamma^{l_\alpha l_\beta} = \frac{2}{g^2} \left(\boldsymbol{\lambda} \cdot \boldsymbol{G_\gamma} \cdot \boldsymbol{\lambda}^\dagger \right)_{\alpha\beta} , \tag{D.1}$$

$$G_\gamma(r_a) = \frac{r_a}{4(1-r_a)^4} \left(2 + 3r_a - 6r_a^2 + r_a^3 + 6r_a \log r_a \right) , \tag{D.2}$$

whereas for the off-shell photon piece

$$F_\gamma^{l_\alpha l_\beta} = \frac{2}{g^2} \left(\boldsymbol{\lambda} \cdot \boldsymbol{F_\gamma} \cdot \boldsymbol{\lambda}^\dagger \right)_{\alpha\beta} , \tag{D.3}$$

$$F_\gamma(r_a) = -\frac{r_a}{12(1-r_a)^4} \left[7 - 8r_a - 11r_a^2 + 12r_a^3 - (2 - 20r_a + 24r_a^2) \log r_a \right] . \tag{D.4}$$

The Z penguin contribution can be split in two parts, namely

$$F_Z^{l_\alpha l_\beta} = F_Z^{l_\alpha l_\beta (1)} + F_Z^{l_\alpha l_\beta (2)} , \tag{D.5}$$

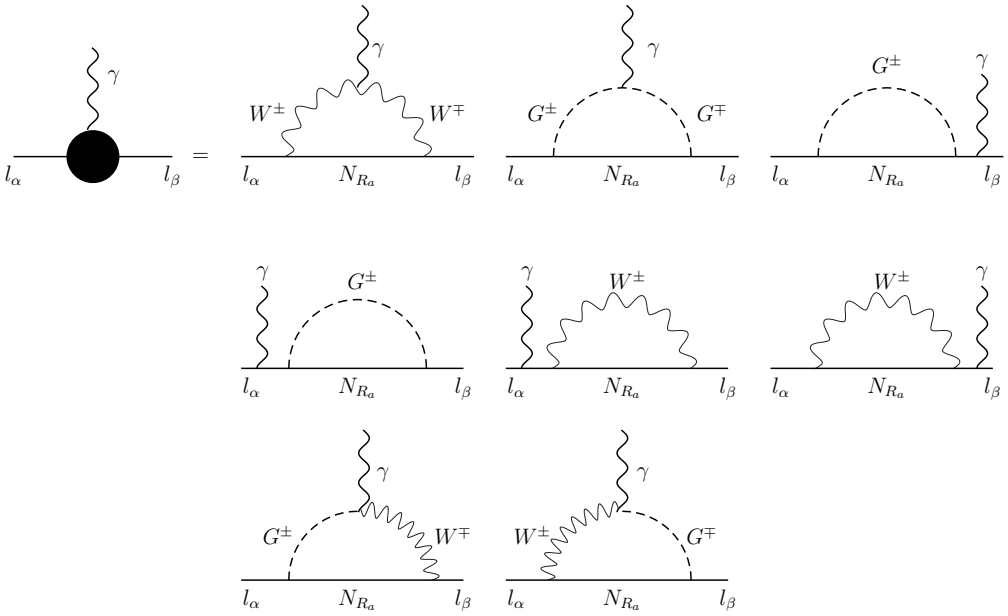

Figure D.1: *Feynman diagrams contributing to $l_\alpha \to l_\beta\gamma$, and, with external fermion legs attached to the γ line, to $l_\alpha \to l_\beta l_\beta l_\beta$ processes (see Figure D.3) in the type-I seesaw model.*

where the first piece can be written as

$$F_Z^{l_\alpha l_\beta (1)} = \frac{2}{g^2}\left[\boldsymbol{\lambda}\cdot\left(\hat{\boldsymbol{F}}_{\boldsymbol{Z}} + \hat{\boldsymbol{G}}_{\boldsymbol{Z}}^{(\mathbf{1})}\right)\cdot\boldsymbol{\lambda}^\dagger\right]_{\alpha\beta}, \tag{D.6}$$

$$F_Z(r_a) = \frac{5r_a}{2(1-r_a)^2}\left(1 - r_a + \log r_a\right), \tag{D.7}$$

$$G_Z^{(1)}(r_a) = -\frac{r_a}{1-r_a}\log r_a, \tag{D.8}$$

while the second contribution according to

$$F_Z^{l_\alpha l_\beta (2)} = \frac{4}{g^4}\left[\boldsymbol{\lambda}\cdot\left(\tilde{\boldsymbol{G}}_{\boldsymbol{Z}}^{(\mathbf{2})} + \tilde{\boldsymbol{G}}_{\boldsymbol{Z}}^{(\mathbf{3})} + \tilde{\boldsymbol{G}}_{\boldsymbol{Z}}^{(\mathbf{4})} + \tilde{\boldsymbol{H}}_{\boldsymbol{Z}}\right)\cdot\boldsymbol{\lambda}^\dagger\right]_{\alpha\beta}, \tag{D.9}$$

$$\tilde{G}_Z^{(A)}(r_a, r_b) = (\boldsymbol{\lambda}^\dagger\cdot\boldsymbol{\lambda})_{ab} G_Z^{(A)}(r_a, r_b) \quad \text{with} \quad A = 2,3,4, \tag{D.10}$$

$$G_Z^{(2)}(r_a, r_b) = -\frac{r_a r_b}{2(r_a - r_b)}\left(\frac{1-r_b}{1-r_a}\log r_a - \frac{1-r_a}{1-r_b}\log r_b\right), \tag{D.11}$$

$$G_Z^{(3)}(r_a, r_b) = \frac{r_a r_b}{2(1-r_a)}\log r_a, \tag{D.12}$$

$$G_Z^{(4)}(r_a, r_b) = \frac{r_a r_b}{2(1-r_b)}\log r_b, \tag{D.13}$$

$$\tilde{H}_Z(r_a, r_b) = \left(\boldsymbol{\lambda}^T\cdot\boldsymbol{\lambda}^*\right)_{ab} H_Z(r_a, r_b), \tag{D.14}$$

$$H_Z(r_a, r_b) = -\frac{\sqrt{r_a r_b}}{4(r_a - r_b)}\left[\frac{r_b(1-4r_a)}{1-r_a}\log r_a - \frac{r_a(1-4r_b)}{1-r_b}\log r_b\right]. \tag{D.15}$$

Note that due to the constraint implied by the $SU(3)_{\ell_L + N_R}$ flavor symmetry the off-diagonal elements of the matrices $\tilde{G}_Z^{(A)}(r_a, r_b)$ and $\tilde{H}_Z^{(A)}(r_a, r_b)$ vanish.

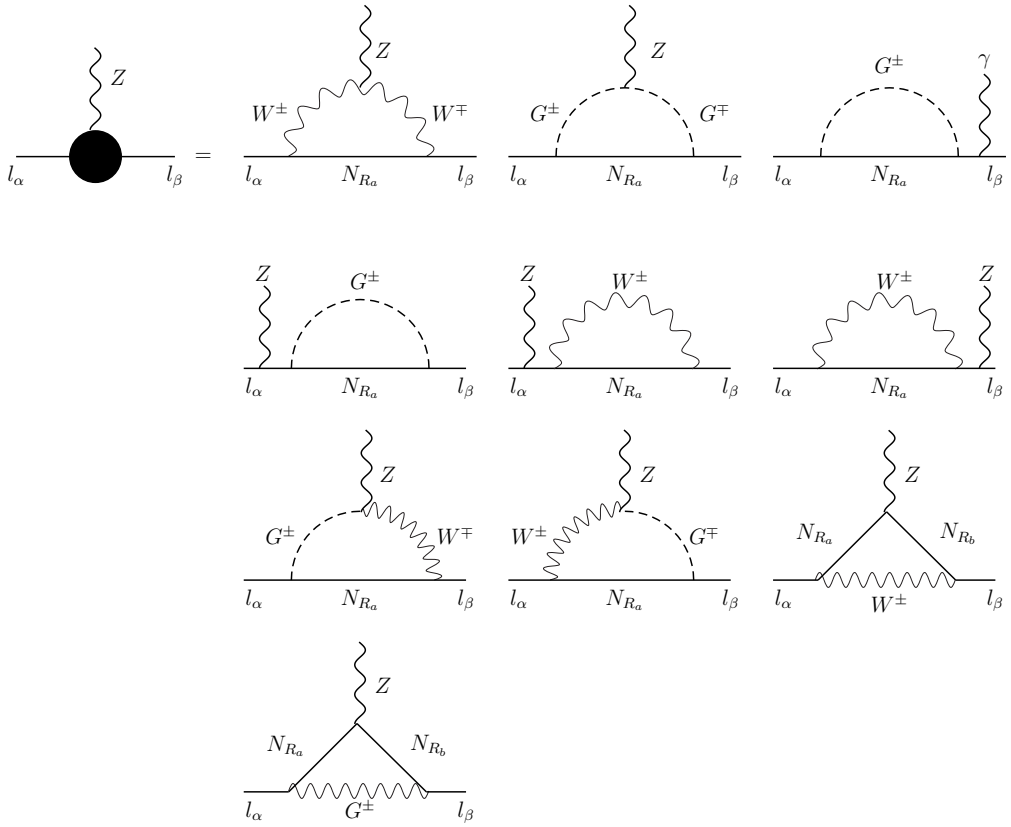

Figure D.2: *Z penguin Feynman diagrams contributing to $l_\alpha \to l_\beta l_\beta l_\beta$ processes, once fermion external lines are attached to the Z boson line (see Figure D.3).*

The box diagram contributions can be split in three parts as follows

$$F_{\text{Box}}^{l_\alpha 3 l_\beta} = \sum_{A=1,2,3} F_{\text{Box}}^{l_\alpha 3 l_\beta (A)} , \tag{D.16}$$

The first part reads

$$F_{\text{Box}}^{l_\alpha 3 l_\beta (1)} = \frac{2}{g^2} \left[\boldsymbol{\lambda} \cdot \hat{\boldsymbol{F}}^{\mathbf{(1)}}_{\mathbf{Box}} \cdot \boldsymbol{\lambda}^\dagger \right]_{ij} , \tag{D.17}$$

$$F_{\text{Box}}^{(1)}(r_a) = -\frac{2 r_a}{(1-r_a)^2} \left(1 - r_a + r_a \log r_a\right) . \tag{D.18}$$

The second is given by

$$F_{\text{Box}}^{l_\alpha 3 l_\beta (2)}(\beta) = \frac{4}{g^4} \left[\boldsymbol{\lambda} \cdot \left(\tilde{\boldsymbol{F}}^{\mathbf{(2)}}_{\mathbf{Box}}(\beta) + \tilde{\boldsymbol{F}}^{\mathbf{(3)}}_{\mathbf{Box}}(\beta) \right) \cdot \boldsymbol{\lambda}^\dagger \right]_{\alpha\beta} , \tag{D.19}$$

$$\tilde{F}_{\text{Box}}^{(A)}(r_a, r_b)(\beta) = \lambda^*_{\beta a} \, F_{\text{Box}}^{(A)}(r_a, r_b) \, \lambda_{jb} \quad \text{with} \quad A = 2, 3, \tag{D.20}$$

$$\begin{aligned} F_{\text{Box}}^{(2)}(r_a, r_b) = \frac{r_a r_b}{4(r_a - r_b)} \Bigg[& \frac{1 - 4 r_a (2 - r_b)}{(1-r_a)^2} \log r_a - \frac{1 - 4 r_b (2 - r_a)}{(1-r_b)^2} \log r_b \\ & - \frac{r_a - r_b}{(1-r_a)(1-r_b)} (7 - 4 r_a r_b) \Bigg] , \end{aligned} \tag{D.21}$$

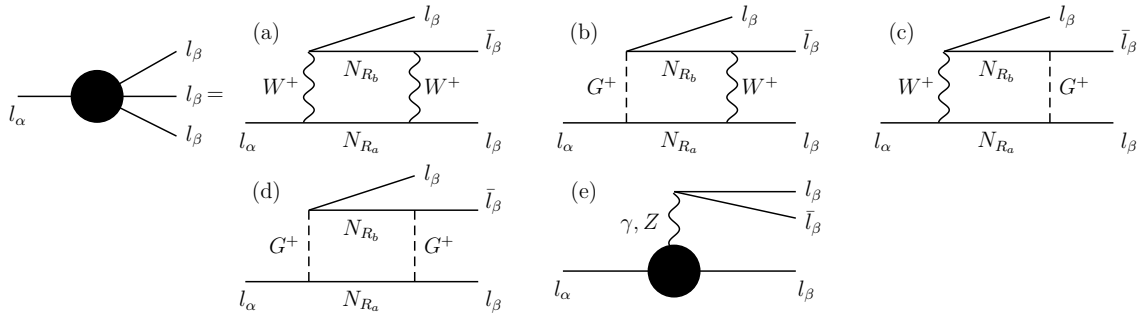

Figure D.3: *Box ((a)-(d)) and γ and Z penguins ((e)) Feynman diagrams contributing to $l_\alpha \to l_\beta l_\beta l_\beta$ processes in the type-I seesaw model.*

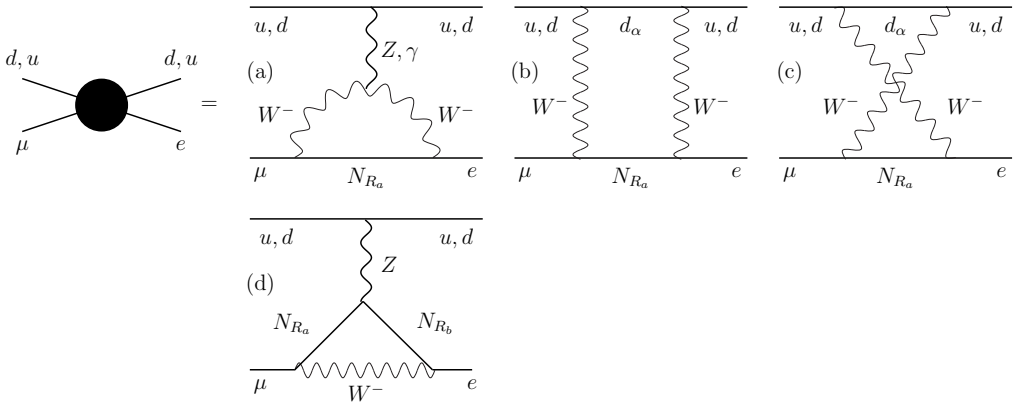

Figure D.4: *Box and Z and γ penguins Feynman diagrams contributing to μ to e conversion in the type-I seesaw model.*

$$F^{(3)}_{\text{Box}}(r_a, r_b) = 2 r_a r_b \left[\frac{r_b}{(1-r_b)^2}(1 - r_b + \log r_b) + \frac{1}{(1-r_a)^2}(1 - r_a + r_a \log r_a) \right], \tag{D.22}$$

where in $\tilde{F}^{(A)}_{\text{Box}}(r_a, r_b)(\beta)$ no summation over the indices a, b is performed. Finally, the third term in (D.16) can be written as

$$F^{l_\alpha 3 l_\beta (3)}_{\text{Box}}(\beta) = \frac{4}{g^4} \left[\boldsymbol{\lambda} \cdot \tilde{\boldsymbol{G}}_{\mathbf{Box}}(\beta) \cdot \boldsymbol{\lambda}^\dagger \right]_{\alpha\beta} \tag{D.23}$$

$$\tilde{G}_{\text{Box}}(r_a, r_b)(\beta) = \lambda_{\beta a}\, G_{\text{Box}}(r_a, r_b)\, \lambda^*_{\beta b}, \tag{D.24}$$

$$\begin{aligned} G_{\text{Box}}(r_a, r_b) = -\frac{\sqrt{r_a r_b}}{r_a - r_b} \Bigg[& \frac{r_a\,[1 - 2r_b(1 - 2r_a)]}{(1-r_a)^2} \log r_a - \frac{r_b\,[1 - 2r_a(1 - 2r_b)]}{(1-r_b)^2} \log r_b \\ & + \frac{(r_a - r_b)}{(1-r_a)(1-r_b)}(1 + 2 r_a r_b) \Bigg], \end{aligned} \tag{D.25}$$

where, again, in $\tilde{G}^{(A)}_{\text{Box}}(r_a, r_b)(\beta)$ no summation over the indices a and b is performed.

For completeness the Feynman diagrams for $\mu - e$ conversion in nuclei are shown as well. The process proceeds also via Z and γ penguins and box diagrams as displayed in Figure D.4.

LIST OF FIGURES

1.1 Feynman diagrams for H production. 10
1.2 Decay branching ratios for the SM Higgs as a function of its mass. 11
1.3 The signal strength for the individual channel and their combination at ATLAS and at CMS. 12
1.4 The orbit space of 2HDM, lying along or within the Minkowski future light-cone as required by $r^\mu r_\mu > 0$. 19
1.5 The orbit space of 3HDM defined by two forward cones as determined by the $SU(3)$ $\bar{3} \otimes 3$ decomposition. 24

3.1 Two-dimensional illustration of the geometric minimization method. 39
3.2 The orbit space of the toy model projected on the (x, z)-plane. 41
3.3 Various possible directions of steepest descent and the corresponding minima. 42
3.4 Sketch of the orbit space Γ of the S_4-symmetric 3HDM in the (x, y, z)-space and the neutral orbit space in the (x, y)-plain. 43
3.5 Sketch of the neutral orbit space in the tetrahedral 3HDM viewed from two angles. 46

4.1 Spectrum of solar neutrinos arising from the pp chain as predicted by the standard solar model. 57
4.2 Super-Kamiokande results. 59
4.3 KamLAND results. 60
4.4 Global 3ν oscillation analysis including all available neutrino oscillation data. 62
4.5 Dimension five effective operator (Weinberg operator) responsible for Majorana neutrino masses. 65
4.6 Four-loop order realization of the Weinberg operator from which is has been argued the phenomenologically inconsistency of those realizations. . . 66
4.7 Tree level realizations of the Weinberg operator which define the type-I, type-II and type-III seesaw models. 67
4.8 Feynman diagrams accounting for the Zee model and the radiative seesaw. 67
4.9 Some examples of two-loop topologies associated with two-loop realizations of the Weinberg operator. 68

4.10 Feynman diagram accounting for light neutrino masses in the Cheng-Li-Babu-Zee model. 69

5.1 Decay branching ratio BR($\mu \to e\gamma$) normalized to $|\boldsymbol{\lambda_1}|^4$ as a function of the RH neutrino mass and the corresponding bounds on $|\boldsymbol{\lambda_1}|$. 82
5.2 Decay branching ratio BR($\mu^- \to e^- e^+ e^-$) normalized to $|\boldsymbol{\lambda_1}|^4$ as a function of RH neutrino mass and the corresponding bounds on $|\boldsymbol{\lambda_1}|$. 84
5.3 Branching ratio BR($\mu^- \mathrm{Au}^{197}_{79} \to e^- \mathrm{Au}^{197}_{79}$) normalized to $|\boldsymbol{\lambda_1}|^4$ as a function of the RH neutrino mass and the corresponding bounds on $|\boldsymbol{\lambda_1}|$. 85
5.4 Washout factors for muon and electron lepton flavors and $|Y_{\Delta_B}|$ as a function of the RH neutrino mass. 87

D.1 Feynman diagrams contributing to $l_\alpha \to l_\beta \gamma$, and, with external fermion legs attached to the γ line, to $l_\alpha \to l_\beta l_\beta l_\beta$ processes in the type-I seesaw model. 108
D.2 Z penguin Feynman diagrams contributing to $l_\alpha \to l_\beta l_\beta l_\beta$ processes, once fermion external lines are attached to the Z boson line. 109
D.3 Box and Z and γ penguins Feynman diagrams contributing to $l_\alpha \to l_\beta l_\beta l_\beta$ processes in the type-I seesaw model. 110
D.4 Box and Z and γ penguins Feynman diagrams contributing to $\mu - e$ conversion in nuclei in the type-I seesaw model. 110

LIST OF TABLES

4.1 Neutrino oscillation parameters summary. 61
4.2 Present experimental upper bounds on lepton-flavor-violating processes for pure leptonic decays. 64

5.1 Numerical factors for Ti and Au entering in the $\mu - e$ conversion rate. . . . 84

BIBLIOGRAPHY

[1] P. W. Higgs, *Broken Symmetries and the Masses of Gauge Bosons*, *Phys.Rev.Lett.* **13** (1964) 508–509.

[2] P. W. Higgs, *Spontaneous Symmetry Breakdown without Massless Bosons*, *Phys.Rev.* **145** (1966) 1156–1163.

[3] F. Englert and R. Brout, *Broken symmetry and the mass of gauge vector mesons*, *Phys. Rev. Lett.* **13** (Aug, 1964) 321–323.

[4] P. W. Higgs, *Broken symmetries, massless particles and gauge fields*, *Phys.Lett.* **12** (1964) 132–133.

[5] **ATLAS Collaboration** Collaboration, G. Aad *et. al.*, *Observation of a new particle in the search for the Standard Model Higgs boson with the ATLAS detector at the LHC*, *Phys.Lett.* **B716** (2012) 1–29 [1207.7214].

[6] **CMS Collaboration** Collaboration, S. Chatrchyan *et. al.*, *Observation of a new boson at a mass of 125 GeV with the CMS experiment at the LHC*, *Phys.Lett.* **B716** (2012) 30–61 [1207.7235].

[7] http://cerncourier.com/cws/article/cern/5403.

[8] **ATLAS Collaboration** Collaboration, *Observation of an excess of events in the search for the Standard Model Higgs boson in the gamma-gamma channel with the ATLAS detector*, .

[9] G. Branco, P. Ferreira, L. Lavoura, M. Rebelo, M. Sher *et. al.*, *Theory and phenomenology of two-Higgs-doublet models*, *Phys.Rept.* **516** (2012) 1–102 [1106.0034].

[10] G. C. Branco, L. Lavoura and J. P. Silva, *CP Violation*, *Int.Ser.Monogr.Phys.* **103** (1999) 1–536.

[11] P. Minkowski, $\mu \to e\gamma$ *at a rate of one out of 1-billion muon decays?*, *Phys.Lett.* **B67** (1977) 421.

[12] T. Yanagida, *Horizontal symmetry and masses of neutrinos*, *Conf.Proc.* **C7902131** (1979) 95–99.

[13] R. N. Mohapatra and G. Senjanovic, *Neutrino Mass and Spontaneous Parity Violation*, *Phys.Rev.Lett.* **44** (1980) 912.

[14] J. Schechter and J. Valle, *Neutrino Masses in $SU(2) \otimes U(1)$ Theories*, *Phys.Rev.* **D22** (1980) 2227.

[15] J. Schechter and J. Valle, *Neutrino Decay and Spontaneous Violation of Lepton Number*, *Phys.Rev.* **D25** (1982) 774.

[16] A. Degee and I. Ivanov, *Higgs masses of the general 2HDM in the Minkowski-space formalism*, *Phys.Rev.* **D81** (2010) 015012 [0910.4492].

[17] A. Degee, I. Ivanov and V. Keus, *Geometric minimization of highly symmetric potentials*, *JHEP* **1302** (2013) 125 [1211.4989].

[18] D. Aristizabal Sierra, A. Degee and J. Kamenik, *Minimal Lepton Flavor Violating Realizations of Minimal Seesaw Models*, *JHEP* **1207** (2012) 135 [1205.5547].

[19] J. F. Gunion, H. E. Haber, G. L. Kane and S. Dawson, *The Higgs Hunter's guide*, *Front.Phys.* **80** (2000) 1–448.

[20] A. Djouadi, *The Anatomy of electro-weak symmetry breaking. I: The Higgs boson in the standard model*, *Phys.Rept.* **457** (2008) 1–216 [hep-ph/0503172].

[21] A. Djouadi, *The Anatomy of electro-weak symmetry breaking. II. The Higgs bosons in the minimal supersymmetric model*, *Phys.Rept.* **459** (2008) 1–241 [hep-ph/0503173].

[22] C. Giunti and C. W. Kim, *Fundamentals of Neutrino Physics and Astrophysics*, .

[23] R. Mohapatra and P. Pal, *Massive neutrinos in physics and astrophysics. Second edition*, *World Sci.Lect.Notes Phys.* **60** (1998) 1–397.

[24] E. K. Akhmedov, *Neutrino physics*, hep-ph/0001264.

[25] S. Davidson, E. Nardi and Y. Nir, *Leptogenesis*, *Phys.Rept.* **466** (2008) 105–177 [0802.2962].

[26] C. S. Fong, E. Nardi and A. Riotto, *Leptogenesis in the Universe*, *Adv.High Energy Phys.* **2012** (2012) 158303 [1301.3062].

[27] T. Hambye, *Leptogenesis: beyond the minimal type I seesaw scenario*, *New J.Phys.* **14** (2012) 125014 [1212.2888].

[28] E. Fermi, *An attempt of a theory of beta radiation. 1.*, *Z.Phys.* **88** (1934) 161–177.

[29] S. Weinberg, *A Model of Leptons*, *Phys.Rev.Lett.* **19** (1967) 1264–1266.

[30] A. Salam, *Weak and Electromagnetic Interactions*, *Conf.Proc.* **C680519** (1968) 367–377.

[31] S. Glashow and S. Weinberg, *Breaking chiral symmetry*, *Phys.Rev.Lett.* **20** (1968) 224–227.

[32] **LEP Working Group for Higgs boson searches, ALEPH Collaboration, DELPHI Collaboration, L3 Collaboration, OPAL Collaboration** Collaboration, R. Barate *et. al.*, *Search for the standard model Higgs boson at LEP*, *Phys.Lett.* **B565** (2003) 61–75 [hep-ex/0306033].

[33] **CDF Collaboration, D0 Collaboration** Collaboration, T. T. Group, *Combined CDF and D0 Upper Limits on Standard Model Higgs-Boson Production with 2.1 - 5.4 fb^{-1} of Data*, 0911.3930.

[34] **LHC Higgs Cross Section Working Group** Collaboration, S. Dittmaier *et. al.*, *Handbook of LHC Higgs Cross Sections: 1. Inclusive Observables*, 1101.0593.

[35] M. E. Peskin, *Comparison of LHC and ILC Capabilities for Higgs Boson Coupling Measurements*, 1207.2516.

[36] H. E. Haber and G. L. Kane, *The Search for Supersymmetry: Probing Physics Beyond the Standard Model*, *Phys.Rept.* **117** (1985) 75–263.

[37] H. P. Nilles, *Supersymmetry, Supergravity and Particle Physics*, *Phys.Rept.* **110** (1984) 1–162.

[38] R. Contino, *The Higgs as a Composite Nambu-Goldstone Boson*, 1005.4269.

[39] **Particle Data Group** Collaboration, J. Beringer *et. al.*, *Review of Particle Physics (RPP)*, *Phys.Rev.* **D86** (2012) 010001.

[40] S. Dittmaier, C. Mariotti, G. Passarino, R. Tanaka *et. al.*, *Handbook of LHC Higgs Cross Sections: 2. Differential Distributions*, 1201.3084.

[41] A. Blondel and F. Zimmermann, *A High Luminosity e^+e^- Collider in the LHC tunnel to study the Higgs Boson*, 1112.2518.

[42] M. Koratzinos, A. Blondel, R. Aleksan, O. Brunner, A. Butterworth *et. al.*, *TLEP: A High-Performance Circular e^+e^- Collider to Study the Higgs Boson*, 1305.6498.

[43] B. W. Lee, C. Quigg and H. B. Thacker, *Weak interactions at very high energies: The role of the higgs-boson mass*, *Phys. Rev. D* **16** (Sep, 1977) 1519–1531.

[44] J. M. Cornwall, D. N. Levin and G. Tiktopoulos, *Uniqueness of spontaneously broken gauge theories.*, *Phys. Rev. Lett.* **31** (Aug, 1973) 572–572.

[45] http://lepewwg.web.cern.ch/LEPEWWG/plots/winter2012.

[46] **ALEPH Collaboration, DELPHI Collaboration, L3 Collaboration, OPAL Collaboration, The LEP working group for Higgs boson searches** Collaboration, G. Abbiendi *et. al.*, *Search for Charged Higgs bosons: Combined Results Using LEP Data*, *Eur.Phys.J.C* (2013) [1301.6065].

[47] **CDF Collaboration and D0 Collaboration** Collaboration, T. Aaltonen *et. al.*, *Combination of tevatron searches for the standard model higgs boson in the W^+W^- decay mode*, *Phys. Rev. Lett.* **104** (Feb, 2010) 061802.

[48] **The LHC Higgs Cross Section Working Group** Collaboration, S. Heinemeyer *et. al.*, *Handbook of LHC Higgs Cross Sections: 3. Higgs Properties*, 1307.1347.

[49] *Combined coupling measurements of the higgs-like boson with the atlas detector using up to 25 fb^{-1} of proton-proton collision data*, Tech. Rep. ATLAS-CONF-2013-034, CERN, Geneva, Mar, 2013.

[50] *Combination of standard model higgs boson searches and measurements of the properties of the new boson with a mass near 125 gev*, Tech. Rep. CMS-PAS-HIG-13-005, CERN, Geneva, 2013.

[51] E. Witten, *Short Distance Analysis of Weak Interactions*, *Nucl.Phys.* **B122** (1977) 109.

[52] T. Schwetz, M. Tortola and J. Valle, *Where we are on θ_{13}: addendum to 'Global neutrino data and recent reactor fluxes: status of three-flavour oscillation parameters'*, *New J.Phys.* **13** (2011) 109401 [1108.1376].

[53] A. Sakharov, *Violation of CP Invariance, c Asymmetry, and Baryon Asymmetry of the Universe*, *Pisma Zh.Eksp.Teor.Fiz.* **5** (1967) 32–35.

[54] **WMAP Collaboration** Collaboration, G. Hinshaw *et. al.*, *Nine-Year Wilkinson Microwave Anisotropy Probe (WMAP) Observations: Cosmological Parameter Results*, 1212.5226.

[55] J. F. Gunion, *Extended Higgs sectors*, hep-ph/0212150.

[56] P. Langacker, *Grand Unified Theories and Proton Decay*, *Phys.Rept.* **72** (1981) 185.

[57] G. Lazarides, Q. Shafi and C. Wetterich, *Proton Lifetime and Fermion Masses in an SO(10) Model*, *Nucl.Phys.* **B181** (1981) 287.

[58] R. N. Mohapatra and G. Senjanovic, *Neutrino Masses and Mixings in Gauge Models with Spontaneous Parity Violation*, *Phys.Rev.* **D23** (1981) 165.

[59] C. Wetterich, *Neutrino Masses and the Scale of B-L Violation*, *Nucl.Phys.* **B187** (1981) 343.

[60] A. Zee, *A Theory of Lepton Number Violation, Neutrino Majorana Mass, and Oscillation*, *Phys.Lett.* **B93** (1980) 389.

[61] K. Babu, *Model of 'Calculable' Majorana Neutrino Masses*, *Phys.Lett.* **B203** (1988) 132.

[62] D. Ross and M. Veltman, *Neutral Currents in Neutrino Experiments*, *Nucl.Phys.* **B95** (1975) 135.

[63] S. Glashow, J. Iliopoulos and L. Maiani, *Weak Interactions with Lepton-Hadron Symmetry*, *Phys.Rev.* **D2** (1970) 1285–1292.

[64] I. F. Ginzburg and M. Krawczyk, *Symmetries of two Higgs doublet model and CP violation*, *Phys.Rev.* **D72** (2005) 115013 [hep-ph/0408011].

[65] I. Ginzburg and K. Kanishev, *Different vacua in 2HDM*, *Phys.Rev.* **D76** (2007) 095013 [0704.3664].

[66] G. Sartori and G. Valente, *Allowed and observable phases in two Higgs doublet standard models*, hep-ph/0304026.

[67] N. Deshpande and X.-G. He, *CP violation in a multi - Higgs doublet model*, *Pramana* **45** (1995) S73–S83 [hep-ph/9409234].

[68] R. Erdem, *Symmetries and observable parameters of multi - Higgs doublet models*, *Phys.Lett.* **B355** (1995) 222–228.

[69] P. Ferreira and J. P. Silva, *Discrete and continuous symmetries in multi-Higgs-doublet models*, *Phys.Rev.* **D78** (2008) 116007 [0809.2788].

[70] A. Barroso, P. Ferreira, R. Santos and J. P. Silva, *Stability of the normal vacuum in multi-Higgs-doublet models*, *Phys.Rev.* **D74** (2006) 085016 [hep-ph/0608282].

[71] I. P. Ivanov and V. Keus, *Frustrated symmetries in multi-Higgs-doublet models*, *Phys.Lett.* **B695** (2011) 459–462 [1007.5305].

[72] P. P. Giardino, K. Kannike, I. Masina, M. Raidal and A. Strumia, *The universal Higgs fit*, 1303.3570.

[73] **CMS Collaboration** Collaboration, S. Chatrchyan *et. al.*, *Study of the Mass and Spin-Parity of the Higgs Boson Candidate Via Its Decays to Z Boson Pairs*, *Phys.Rev.Lett.* **110** (2013) 081803 [1212.6639].

[74] T. Cheng and M. Sher, *Mass Matrix Ansatz and Flavor Nonconservation in Models with Multiple Higgs Doublets*, *Phys.Rev.* **D35** (1987) 3484.

[75] H. Haber, G. L. Kane and T. Sterling, *The Fermion Mass Scale and Possible Effects of Higgs Bosons on Experimental Observables*, *Nucl.Phys.* **B161** (1979) 493.

[76] L. J. Hall and M. B. Wise, *Flavor changing Higgs - boson couplings*, *Nucl.Phys.* **B187** (1981) 397.

[77] J. F. Donoghue and L. F. Li, *Properties of Charged Higgs Bosons*, *Phys.Rev.* **D19** (1979) 945.

[78] V. D. Barger, J. Hewett and R. Phillips, *Nex constraints on the charged Higgs sector in two-Higgs-doublet models*, *Phys.Rev.* **D41** (1990) 3421–3441.

[79] Y. Grossman, *Phenomenology of models with more than two Higgs doublets*, *Nucl.Phys.* **B426** (1994) 355–384 [hep-ph/9401311].

[80] A. Akeroyd, *Nonminimal neutral Higgs bosons at LEP-2*, *Phys.Lett.* **B377** (1996) 95–101 [hep-ph/9603445].

[81] A. Akeroyd and W. J. Stirling, *Light charged Higgs scalars at high-energy e+ e- colliders*, *Nucl.Phys.* **B447** (1995) 3–17.

[82] M. Aoki, S. Kanemura, K. Tsumura and K. Yagyu, *Models of Yukawa interaction in the two Higgs doublet model, and their collider phenomenology*, *Phys.Rev.* **D80** (2009) 015017 [0902.4665].

[83] R. Barbieri, L. J. Hall, Y. Nomura and V. S. Rychkov, *Supersymmetry without a Light Higgs Boson*, *Phys.Rev.* **D75** (2007) 035007 [hep-ph/0607332].

[84] P. Ferreira, R. Santos, M. Sher and J. P. Silva, *Implications of the LHC two-photon signal for two-Higgs-doublet models*, *Phys.Rev.* **D85** (2012) 077703 [1112.3277].

[85] P. Ferreira, R. Santos, M. Sher and J. P. Silva, *Could the LHC two-photon signal correspond to the heavier scalar in two-Higgs-doublet models?*, *Phys.Rev.* **D85** (2012) 035020 [1201.0019].

[86] P. Ferreira, R. Santos, H. E. Haber and J. P. Silva, *Mass-degenerate Higgs bosons at 125 GeV in the Two-Higgs-Doublet Model*, *Phys.Rev.* **D87** (2013) 055009 [1211.3131].

[87] P. Ferreira, R. Santos, M. Sher and J. P. Silva, *2HDM confronting LHC data*, 1305.4587.

[88] M. Trodden, *Electroweak baryogenesis*, *Rev.Mod.Phys.* **71** (1999) 1463–1500 [hep-ph/9803479].

[89] D. E. Morrissey and M. J. Ramsey-Musolf, *Electroweak baryogenesis*, *New J.Phys.* **14** (2012) 125003 [1206.2942].

[90] E. Ma, *Verifiable radiative seesaw mechanism of neutrino mass and dark matter*, *Phys.Rev.* **D73** (2006) 077301 [hep-ph/0601225].

[91] S. Davidson and H. E. Haber, *Basis-independent methods for the two-Higgs-doublet model*, *Phys.Rev.* **D72** (2005) 035004 [hep-ph/0504050].

[92] H. E. Haber and D. O'Neil, *Basis-independent methods for the two-Higgs-doublet model. II. The Significance of tan beta*, *Phys.Rev.* **D74** (2006) 015018 [hep-ph/0602242].

[93] D. O'Neil, *Phenomenology of the Basis-Independent CP-Violating Two-Higgs Doublet Model [Dissertation]*, 0908.1363.

[94] I. Ivanov, *Minkowski space structure of the Higgs potential in 2HDM*, *Phys.Rev.* **D75** (2007) 035001 [hep-ph/0609018].

[95] I. P. Ivanov, *Minkowski space structure of the Higgs potential in 2HDM. II. Minima, symmetries, and topology*, *Phys.Rev.* **D77** (2008) 015017 [0710.3490].

[96] C. Nishi, *Physical parameters and basis transformations in the Two-Higgs-Doublet model*, *Phys.Rev.* **D77** (2008) 055009 [0712.4260].

[97] I. Ivanov, *Thermal evolution of the ground state of the most general 2HDM*, *Acta Phys.Polon.* **B40** (2009) 2789–2807 [0812.4984].

[98] A. Barroso, P. Ferreira and R. Santos, *Neutral minima in two-Higgs doublet models*, *Phys.Lett.* **B652** (2007) 181–193 [hep-ph/0702098].

[99] P. Ferreira and D. Jones, *Bounds on scalar masses in two Higgs doublet models*, *JHEP* **0908** (2009) 069 [0903.2856].

[100] S. Davidson and H. E. Haber, *Erratum: Basis-independent methods for the two-higgs-doublet model [phys. rev. d 72, 035004 (2005)]*, *Phys. Rev. D* **72** (Nov, 2005) 099902.

[101] H. E. Haber and D. O'Neil, *Erratum: Basis-independent methods for the two-higgs-doublet model. ii. the significance of tan beta [phys. rev. d 74, 015018 (2006)]*, *Phys. Rev. D* **74** (Sep, 2006) 059905.

[102] J. F. Gunion and H. E. Haber, *Conditions for CP-violation in the general two-Higgs-doublet model*, *Phys.Rev.* **D72** (2005) 095002 [hep-ph/0506227].

[103] I. P. Ivanov, *General two-order-parameter ginzburg-landau model with quadratic and quartic interactions*, *Phys. Rev. E* **79** (Feb, 2009) 021116.

[104] F. Nagel, *New aspects of gauge-boson couplings and the Higgs sector*, hep-ph/0304026.

[105] I. Ivanov and C. Nishi, *Properties of the general NHDM. I. The Orbit space*, *Phys.Rev.* **D82** (2010) 015014 [1004.1799].

[106] I. Ivanov, *Properties of the general NHDM. II. Higgs potential and its symmetries*, *JHEP* **1007** (2010) 020 [1004.1802].

[107] C. Nishi, *CP violation conditions in N-Higgs-doublet potentials*, *Phys.Rev.* **D74** (2006) 036003 [hep-ph/0605153].

[108] J. Velhinho, R. Santos and A. Barroso, *Tree level vacuum stability in two Higgs doublet models*, *Phys.Lett.* **B322** (1994) 213–218.

[109] M. Maniatis, A. von Manteuffel, O. Nachtmann and F. Nagel, *Stability and symmetry breaking in the general two-Higgs-doublet model*, *Eur.Phys.J.* **C48** (2006) 805–823 [hep-ph/0605184].

[110] M. Maniatis, A. von Manteuffel and O. Nachtmann, *CP violation in the general two-Higgs-doublet model: A Geometric view*, *Eur.Phys.J.* **C57** (2008) 719–738 [0707.3344].

[111] E. Accomando, A. Akeroyd, E. Akhmetzyanova, J. Albert, A. Alves *et. al.*, *Workshop on CP Studies and Non-Standard Higgs Physics*, hep-ph/0608079.

[112] L. Lavoura and H. Kuhbock, *A(4) model for the quark mass matrices*, *Eur.Phys.J.* **C55** (2008) 303–308 [0711.0670].

[113] S. Morisi and E. Peinado, *An A(4) model for lepton masses and mixings*, *Phys.Rev.* **D80** (2009) 113011 [0910.4389].

[114] R. de Adelhart Toorop, F. Bazzocchi, L. Merlo and A. Paris, *Constraining Flavour Symmetries At The EW Scale I: The A4 Higgs Potential*, *JHEP* **1103** (2011) 035 [1012.1791].

[115] I. Ivanov and E. Vdovin, *Discrete symmetries in the three-Higgs-doublet model*, *Phys.Rev.* **D86** (2012) 095030 [1206.7108].

[116] E. Ma and G. Rajasekaran, *Softly broken A(4) symmetry for nearly degenerate neutrino masses*, *Phys.Rev.* **D64** (2001) 113012 [hep-ph/0106291].

[117] G. Branco, J. Gerard and W. Grimus, *Geometrical T-violation*, *Phys.Lett.* **B136** (1984) 383.

[118] I. de Medeiros Varzielas and D. Emmanuel-Costa, *Geometrical CP Violation*, *Phys.Rev.* **D84** (2011) 117901 [1106.5477].

[119] W. Pauli, *Dear radioactive ladies and gentlemen*, *Phys.Today* **31N9** (1978) 27.

[120] F. Reines and C. L. Cowan, *The neutrino*, *Nature* **178** (1956) 446–449.

[121] B. Pontecorvo, *Inverse beta processes and nonconservation of lepton charge*, *Sov.Phys.JETP* **7** (1958) 172–173.

[122] J. Davis, Raymond, D. S. Harmer and K. C. Hoffman, *Search for neutrinos from the sun*, *Phys.Rev.Lett.* **20** (1968) 1205–1209.

[123] **Super-Kamiokande Collaboration** Collaboration, Y. Fukuda *et. al.*, *Evidence for oscillation of atmospheric neutrinos*, *Phys.Rev.Lett.* **81** (1998) 1562–1567 [hep-ex/9807003].

[124] **SNO Collaboration** Collaboration, N. Tolich, *Final results from SNO*, *J.Phys.Conf.Ser.* **375** (2012) 042049.

[125] **KamLAND Collaboration** Collaboration, K. Eguchi *et. al.*, *First results from KamLAND: Evidence for reactor anti-neutrino disappearance*, *Phys.Rev.Lett.* **90** (2003) 021802 [hep-ex/0212021].

[126] **DOUBLE-CHOOZ Collaboration** Collaboration, Y. Abe *et. al.*, *Indication for the disappearance of reactor electron antineutrinos in the Double Chooz experiment*, *Phys.Rev.Lett.* **108** (2012) 131801 [1112.6353].

[127] **Collaboration Daya Bay** Collaboration, D. A. Dwyer, *The Improved Measurement of Electron-antineutrino Disappearance at Daya Bay*, *Nucl.Phys.Proc.Suppl.* **235-236** (2013) 30–32 [1303.3863].

[128] **RENO collaboration** Collaboration, J. Ahn *et. al.*, *Observation of Reactor Electron Antineutrino Disappearance in the RENO Experiment*, *Phys.Rev.Lett.* **108** (2012) 191802 [1204.0626].

[129] W. Rodejohann, *Neutrinoless double beta decay and neutrino physics*, *J.Phys.* **G39** (2012) 124008 [1206.2560].

[130] S. Weinberg, *Baryon and Lepton Nonconserving Processes*, *Phys.Rev.Lett.* **43** (1979) 1566–1570.

[131] M. Fukugita and T. Yanagida, *Baryogenesis Without Grand Unification*, *Phys.Lett.* **B174** (1986) 45.

[132] **WMAP Collaboration** Collaboration, G. Hinshaw *et. al.*, *Five-Year Wilkinson Microwave Anisotropy Probe (WMAP) Observations: Data Processing, Sky Maps, and Basic Results*, *Astrophys.J.Suppl.* **180** (2009) 225–245 [0803.0732].

[133] **Planck Collaboration** Collaboration, P. Ade *et. al.*, *Planck 2013 results. I. Overview of products and scientific results*, 1303.5062.

[134] **Planck Collaboration** Collaboration, P. Ade *et. al.*, *Planck 2013 results. XVI. Cosmological parameters*, 1303.5076.

[135] J. N. Bahcall, M. Pinsonneault and S. Basu, *Solar models: Current epoch and time dependences, neutrinos, and helioseismological properties*, *Astrophys.J.* **555** (2001) 990–1012 [astro-ph/0010346].

[136] J. Bahcall, *http://www.sns.ias.edu/ jnb/*, .

[137] J. N. Bahcall, *NEUTRINO ASTROPHYSICS*, .

[138] **Super-Kamiokande** Collaboration, Y. Ashie *et. al.*, *Evidence for an oscillatory signature in atmospheric neutrino oscillation*, *Phys. Rev. Lett.* **93** (2004) 101801 [hep-ex/0404034].

[139] R. Becker-Szendy *et. al.*, *A search for muon neutrino oscillations with the IMB detector*, *Phys. Rev. Lett.* **69** (1992) 1010–1013.

[140] W. W. M. Allison *et. al.*, *Measurement of the atmospheric neutrino flavour composition in Soudan-2*, *Phys. Lett.* **B391** (1997) 491–500 [hep-ex/9611007].

[141] V. D. Barger, J. G. Learned, S. Pakvasa and T. J. Weiler, *Neutrino decay as an explanation of atmospheric neutrino observations*, *Phys. Rev. Lett.* **82** (1999) 2640–2643 [astro-ph/9810121].

[142] Y. Grossman and M. P. Worah, *Atmospheric ν_μ deficit from decoherence*, hep-ph/9807511.

[143] **SNO** Collaboration, Q. R. Ahmad *et. al.*, *Direct evidence for neutrino flavor transformation from neutral-current interactions in the Sudbury Neutrino Observatory*, *Phys. Rev. Lett.* **89** (2002) 011301 [nucl-ex/0204008].

[144] **KamLAND** Collaboration, K. Eguchi *et. al.*, *First results from KamLAND: Evidence for reactor anti- neutrino disappearance*, *Phys. Rev. Lett.* **90** (2003) 021802 [hep-ex/0212021].

[145] **KamLAND** Collaboration, T. Araki *et. al.*, *Measurement of neutrino oscillation with KamLAND: Evidence of spectral distortion*, *Phys. Rev. Lett.* **94** (2005) 081801 [hep-ex/0406035].

[146] M. Gonzalez-Garcia, M. Maltoni, J. Salvado and T. Schwetz, *Global fit to three neutrino mixing: critical look at present precision*, *JHEP* **1212** (2012) 123 [1209.3023].

[147] Y. Itow., *Talk given at the XXV International Conference on Neutrino Physics*, (Kyoto, Japan), June 3-9, 2012.

[148] **K2K Collaboration** Collaboration, M. Ahn *et. al.*, *Measurement of Neutrino Oscillation by the K2K Experiment*, *Phys.Rev.* **D74** (2006) 072003 [hep-ex/0606032].

[149] **MINOS Collaboration** Collaboration, P. Adamson *et. al.*, *Improved search for muon-neutrino to electron-neutrino oscillations in MINOS*, *Phys.Rev.Lett.* **107** (2011) 181802 [1108.0015].

[150] **T2K Collaboration** Collaboration, K. Abe *et. al.*, *Indication of Electron Neutrino Appearance from an Accelerator-produced Off-axis Muon Neutrino Beam*, *Phys.Rev.Lett.* **107** (2011) 041801 [1106.2822].

[151] **CHOOZ Collaboration** Collaboration, M. Apollonio *et. al.*, *Limits on neutrino oscillations from the CHOOZ experiment*, *Phys.Lett.* **B466** (1999) 415–430 [hep-ex/9907037].

[152] F. Boehm, J. Busenitz, B. Cook, G. Gratta, H. Henrikson *et. al.*, *Final results from the Palo Verde neutrino oscillation experiment*, *Phys.Rev.* **D64** (2001) 112001 [hep-ex/0107009].

[153] **DAYA-BAY Collaboration** Collaboration, F. An *et. al.*, *Observation of electron-antineutrino disappearance at Daya Bay*, *Phys.Rev.Lett.* **108** (2012) 171803 [1203.1669].

[154] **KamLAND Collaboration** Collaboration, A. Gando *et. al.*, *Constraints on θ_{13} from A Three-Flavor Oscillation Analysis of Reactor Antineutrinos at KamLAND*, *Phys.Rev.* **D83** (2011) 052002 [1009.4771].

[155] G. Bellini, J. Benziger, D. Bick, S. Bonetti, G. Bonfini *et. al.*, *Precision measurement of the 7Be solar neutrino interaction rate in Borexino*, *Phys.Rev.Lett.* **107** (2011) 141302 [1104.1816].

[156] **Borexino Collaboration** Collaboration, G. Bellini *et. al.*, *Measurement of the solar 8B neutrino rate with a liquid scintillator target and 3 MeV energy threshold in the Borexino detector*, *Phys.Rev.* **D82** (2010) 033006 [0808.2868].

[157] F. Kaether, W. Hampel, G. Heusser, J. Kiko and T. Kirsten, *Reanalysis of the GALLEX solar neutrino flux and source experiments*, *Phys.Lett.* **B685** (2010) 47–54 [1001.2731].

[158] **SAGE Collaboration** Collaboration, J. Abdurashitov *et. al.*, *Measurement of the solar neutrino capture rate with gallium metal. III: Results for the 2002–2007 data-taking period*, *Phys.Rev.* **C80** (2009) 015807 [0901.2200].

[159] **Super-Kamiokande Collaboration** Collaboration, J. Hosaka *et. al.*, *Solar neutrino measurements in super-Kamiokande-I*, *Phys.Rev.* **D73** (2006) 112001 [hep-ex/0508053].

[160] **SNO Collaboration** Collaboration, B. Aharmim *et. al.*, *Combined Analysis of all Three Phases of Solar Neutrino Data from the Sudbury Neutrino Observatory*, *Phys.Rev.* **C88** (2013) 025501 [1109.0763].

[161] **KATRIN Collaboration** Collaboration, A. Osipowicz *et. al.*, *KATRIN: A Next generation tritium beta decay experiment with sub-eV sensitivity for the electron neutrino mass. Letter of intent*, hep-ex/0109033.

[162] E. Otten and C. Weinheimer, *Neutrino mass limit from tritium beta decay*, *Rept.Prog.Phys.* **71** (2008) 086201 [0909.2104].

[163] E. Andreotti, C. Arnaboldi, P. De Bernardis, J. Beyer, C. Brofferio *et. al.*, *MARE, Microcalorimeter Arrays for a Rhenium Experiment: A detector overview*, *Nucl.Instrum.Meth.* **A572** (2007) 208–210.

[164] P. Bhupal Dev, S. Goswami, M. Mitra and W. Rodejohann, *Constraining Neutrino Mass from Neutrinoless Double Beta Decay*, 1305.0056.

[165] **EXO Collaboration** Collaboration, M. Auger *et. al.*, *Search for Neutrinoless Double-Beta Decay in ^{136}Xe with EXO-200*, *Phys.Rev.Lett.* **109** (2012) 032505 [1205.5608].

[166] H. Klapdor-Kleingrothaus, A. Dietz and I. Krivosheina, *Neutrinoless double beta decay: Status of evidence*, *Found.Phys.* **32** (2002) 1181–1223 [hep-ph/0302248].

[167] K. Abazajian, E. Calabrese, A. Cooray, F. De Bernardis, S. Dodelson *et. al.*, *Cosmological and Astrophysical Neutrino Mass Measurements*, *Astropart.Phys.* **35** (2011) 177–184 [1103.5083].

[168] A. Melchiorri, F. De Bernardis and E. Menegoni, *New limits on the neutrino mass from cosmology*, *Int.J.Mod.Phys.Conf.Ser.* **12** (2012) 368–379.

[169] G. Drexlin, V. Hannen, S. Mertens and C. Weinheimer, *Current direct neutrino mass experiments*, *Adv.High Energy Phys.* **2013** (2013) 293986.

[170] V. Aseev, A. Belesev, A. Berlev, E. Geraskin, A. Golubev *et. al.*, *Measurement of the electron antineutrino mass in tritium beta decay in the Troitsk nu-mass experiment*, *Phys.Atom.Nucl.* **75** (2012) 464–478.

[171] C. Kraus, B. Bornschein, L. Bornschein, J. Bonn, B. Flatt *et. al.*, *Final results from phase II of the Mainz neutrino mass search in tritium beta decay*, *Eur.Phys.J.* **C40** (2005) 447–468 [hep-ex/0412056].

[172] M. Sturm, *Status of the KATRIN experiment with special emphasis on source-related issues*, 1111.4773.

[173] **WMAP Collaboration** Collaboration, D. Spergel *et. al.*, *Wilkinson Microwave Anisotropy Probe (WMAP) three year results: implications for cosmology*, *Astrophys.J.Suppl.* **170** (2007) 377 [astro-ph/0603449].

[174] S. Riemer-Srensen, D. Parkinson and T. M. Davis, *Combining Planck with Large Scale Structure gives strong neutrino mass constraint*, 1306.4153.

[175] **Planck Collaboration** Collaboration, P. Ade *et. al.*, *Planck 2013 results. XVII. Gravitational lensing by large-scale structure*, 1303.5077.

[176] **CMBPol Study Team** Collaboration, D. Baumann *et. al.*, *CMBPol Mission Concept Study: A Mission to Map our Origins*, *AIP Conf.Proc.* **1141** (2009) 3–9 [0811.3911].

[177] A. de Gouvea and P. Vogel, *Lepton Flavor and Number Conservation, and Physics Beyond the Standard Model*, *Prog.Part.Nucl.Phys.* **71** (2013) 75–92 [1303.4097].

[178] W. J. Marciano, T. Mori and J. M. Roney, *Charged Lepton Flavor Violation Experiments*, *Ann.Rev.Nucl.Part.Sci.* **58** (2008) 315–341.

[179] **MEG collaboration** Collaboration, J. Adam *et. al.*, *New limit on the lepton-flavour violating decay $\mu^+ \to e^+\gamma$* , *Phys.Rev.Lett.* **107** (2011) 171801 [1107.5547].

[180] **SINDRUM Collaboration** Collaboration, U. Bellgardt *et. al.*, *Search for the Decay $\mu^+ \to e^+e^+e^-$*, *Nucl.Phys.* **B299** (1988) 1.

[181] **BABAR Collaboration** Collaboration, B. Aubert *et. al.*, *Searches for Lepton Flavor Violation in the Decays $\tau^\pm \to e^\pm\gamma$ and $\tau^\pm \to \mu^\pm\gamma$*, *Phys.Rev.Lett.* **104** (2010) 021802 [0908.2381].

[182] K. Hayasaka, K. Inami, Y. Miyazaki, K. Arinstein, V. Aulchenko *et. al.*, *Search for Lepton Flavor Violating Tau Decays into Three Leptons with 719 Million Produced Tau+Tau- Pairs*, *Phys.Lett.* **B687** (2010) 139–143 [1001.3221].

[183] **SINDRUM II Collaboration** Collaboration, W. H. Bertl *et. al.*, *A Search for muon to electron conversion in muonic gold*, *Eur.Phys.J.* **C47** (2006) 337–346.

[184] R. H. Bernstein and P. S. Cooper, *Charged Lepton Flavor Violation: An Experimenter's Guide*, *Phys.Rept.* (2013) [1307.5787].

[185] R. Sawada, *talk at Neutrino 2012*, .

[186] **MEG Collaboration** Collaboration, J. Adam *et. al.*, *New constraint on the existence of the $\mu \to e\gamma$ decay*, 1303.0754.

[187] A. B. et al. http://www.physi.uni-heidelberg.de/Forschung/he/mu3e/documents/LOI_Mu3e_PSI.pdf.

[188] C. Ankenbrandt, D. Bogert, F. DeJongh, S. Geer, D. McGinnis *et. al.*, *Using the Fermilab proton source for a muon to electron conversion experiment*, physics/0611124.

[189] http://j-parc.jp/researcher/Hadron/en/pac_0701/pdf/P21-LOI.pdf.

[190] http://j-parc.jp/researcher/Hadron/en/pac_0606/pdf/p20-Kuno.pdf.

[191] D. Aristizabal, A. Degee and M. Hirsch, *General classification of 2-loop neutrino mass models*, . To be published.

[192] E. Ma, *Pathways to naturally small neutrino masses*, *Phys.Rev.Lett.* **81** (1998) 1171–1174 [hep-ph/9805219].

[193] R. Foot, H. Lew, X. He and G. C. Joshi, *Seesaw neutrinos masses induced by a triplet of leptons*, *Z.Phys.* **C44** (1989) 441.

[194] F. Bonnet, M. Hirsch, T. Ota and W. Winter, *Systematic study of the d=5 Weinberg operator at one-loop order*, *JHEP* **1207** (2012) 153 [1204.5862].

[195] T. Hahn, *Generating Feynman diagrams and amplitudes with FeynArts 3*, *Comput.Phys.Commun.* **140** (2001) 418–431 [hep-ph/0012260].

[196] F. Bonnet, M. Hirsch, T. Ota and W. Winter, *Systematic study of the d=5 Weinberg operator at one-loop order*, *JHEP* **1207** (2012) 153 [1204.5862].

[197] T. Cheng and L.-F. Li, *Neutrino Masses, Mixings and Oscillations in SU(2) x U(1) Models of Electroweak Interactions*, *Phys.Rev.* **D22** (1980) 2860.

[198] A. Zee, *Quantum Numbers of Majorana Neutrino Masses*, *Nucl.Phys.* **B264** (1986) 99.

[199] **BESS Collaboration** Collaboration, S. Orito *et. al.*, *Precision measurement of cosmic ray anti-proton spectrum*, *Phys.Rev.Lett.* **84** (2000) 1078–1081 [astro-ph/9906426].

[200] A. Buffington and S. Schindler, *Recent cosmic ray anti-proton measurements and astrophysical implications*, *Astrophys.J.* **247** (1981) L105–L109.

[201] A. G. Cohen, A. De Rujula and S. Glashow, *A Matter - antimatter universe?*, *Astrophys.J.* **495** (1998) 539–549 [astro-ph/9707087].

[202] A. Pilaftsis, *Advances in Leptogenesis*, *J.Phys.Conf.Ser.* **447** (2013) 012007.

[203] W. Buchmuller, P. Di Bari and M. Plumacher, *Leptogenesis for pedestrians*, *Annals Phys.* **315** (2005) 305–351 [hep-ph/0401240].

[204] V. Cirigliano, B. Grinstein, G. Isidori and M. B. Wise, *Minimal flavor violation in the lepton sector*, *Nucl.Phys.* **B728** (2005) 121–134 [hep-ph/0507001].

[205] S. Davidson and F. Palorini, *Various definitions of minimal flavour violation for leptons*, *Phys.Lett.* **B642** (2006) 72–80 [hep-ph/0607329].

[206] M. Gavela, T. Hambye, D. Hernandez and P. Hernandez, *Minimal Flavour Seesaw Models*, *JHEP* **0909** (2009) 038 [0906.1461].

[207] R. Alonso, G. Isidori, L. Merlo, L. A. Munoz and E. Nardi, *Minimal flavour violation extensions of the seesaw*, *JHEP* **1106** (2011) 037 [1103.5461].

[208] G. D'Ambrosio, G. Giudice, G. Isidori and A. Strumia, *Minimal flavor violation: An Effective field theory approach*, *Nucl.Phys.* **B645** (2002) 155–187 [hep-ph/0207036].

[209] A. Ibarra, E. Molinaro and S. Petcov, *TeV Scale See-Saw Mechanisms of Neutrino Mass Generation, the Majorana Nature of the Heavy Singlet Neutrinos and $(\beta\beta)_{0\nu}$-Decay*, *JHEP* **1009** (2010) 108 [1007.2378].

[210] D. Aristizabal Sierra and C. E. Yaguna, *On the importance of the 1-loop finite corrections to seesaw neutrino masses*, *JHEP* **1108** (2011) 013 [1106.3587].

[211] R. Mohapatra and J. Valle, *Neutrino Mass and Baryon Number Nonconservation in Superstring Models*, *Phys.Rev.* **D34** (1986) 1642 [0707.4058].

[212] A. Ilakovac and A. Pilaftsis, *Flavor violating charged lepton decays in seesaw-type models*, *Nucl.Phys.* **B437** (1995) 491 [hep-ph/9403398].

[213] http://meg.icepp.s.u-tokyo.ac.jp/docs/prop_psi/proposal.pdf.

[214] A. Blondel, A. Bravar, M. Pohl and others., *Research Proposal for an Experiment to Search for the Decay $\mu \to e\gamma$*, *ArXiv e-prints* (Jan., 2013) [1301.6113].

[215] **SINDRUM II Collaboration.** Collaboration, C. Dohmen *et. al.*, *Test of lepton flavor conservation in $\mu - e$ conversion on titanium*, *Phys.Lett.* **B317** (1993) 631–636.

[216] R. Kitano, M. Koike and Y. Okada, *Detailed calculation of lepton flavor violating muon electron conversion rate for various nuclei*, *Phys.Rev.* **D66** (2002) 096002 [hep-ph/0203110].

[217] S. Blanchet, T. Hambye and F.-X. Josse-Michaux, *Reconciling leptogenesis with observable $\mu \to e\gamma$ rates*, *JHEP* **1004** (2010) 023 [0912.3153].

[218] T. Asaka and S. Blanchet, *Leptogenesis with an almost conserved lepton number*, *Phys.Rev.* **D78** (2008) 123527 [0810.3015].

[219] D. Aristizabal Sierra, F. Bazzocchi, I. de Medeiros Varzielas, L. Merlo and S. Morisi, *Tri-Bimaximal Lepton Mixing and Leptogenesis*, *Nucl.Phys.* **B827** (2010) 34–58 [0908.0907].

[220] E. Nardi, Y. Nir, E. Roulet and J. Racker, *The Importance of flavor in leptogenesis*, *JHEP* **0601** (2006) 164 [hep-ph/0601084].

[221] M. Gonzalez-Garcia, M. Maltoni and J. Salvado, *Updated global fit to three neutrino mixing: status of the hints of $\theta_{13} > t0$*, *JHEP* **1004** (2010) 056 [1001.4524].

[222] B. Gorczyca and M. Krawczyk, *Tree-Level Unitarity Constraints for the SM-like 2HDM*, 1112.5086.

[223] E. W. Kolb and M. S. Turner, *The Early Universe*, *Front.Phys.* **69** (1990) 1–547.